High Temperature QCD Calculations Using Gradient Flow On An Anisotropic Lattice

A DISSERTATION SUBMITTED TO THE DEPARTMENT
OF PHYSICS OF SWANSEA UNIVERSITY
IN PARTIAL FULFILLMENT OF THE REQUIREMENTS
FOR THE DEGREE OF DOCTOR IN PHILOSOPHY

Swansea University
Author: Alan-Francis Kirby
Supervisors: Professor Simon Hands and Professor Chris Allton
April 2022 (Corrections Jan 2023)

Abstract

Understanding the evolution of the universe from its earliest configuration to its present state requires an understanding of strongly coupled systems such as QCD. Many interesting components of QCD such as confinement and chiral-symmetry breaking can only be understood using first principles non-perturbative methods such as lattice field theory. The energy-momentum tensor is key within QCD thermodynamics, containing information on the equation of state and transport properties such as specific heat and viscosity. Defining the energy-momentum tensor on the lattice is challenging, however it has been made obtainable recently by using a tool known generally as gradient flow. This has been used in order to compute thermodynamic quantities on the lattice, however due to the isotropy of the involved lattices, obtaining fine temperature sampling can be difficult. This work implements the gradient flow method for obtaining thermodynamic quantities from the energy-momentum tensor, by using an anisotropic lattice, which as far as the author is aware is the first example of such, and thus provides the novelty of this work. Another application is to compute the topological susceptibility, which is important for axion cosmology, and related to both the strong CP problem and dark matter, again for the first time using an anisotropic lattice for $N_f = 2 + 1$ QCD.

Contents

Title Page i
Abstract ii
Contents iii
List of Figures vi
List of Tables viii
Declaration ix
Acknowledgements 1

1 Motivation and Context **2**

2 Theoretical Prerequisites **5**
2.1 Continuum QCD 7
2.2 Lattice QCD 14
2.2.1 Lattice Gauge Theory 17
2.2.2 Lattice Fermions 21
2.2.3 FASTSUM Lattice Setup 27
2.2.4 Configuration Generation 40
2.3 High Temperature QCD 44
2.4 Gradient Flow 47

3 Validation of Anisotropic Flow and Numerical Stability Checks **52**

4 Energy-Momentum Tensor and Thermodynamics **71**
4.1 Equation of State 71
4.1.1 Derivative Method 71
4.1.2 Integral Method 72
4.1.3 Small Flow Time Expansion Method 73
4.2 Topological Susceptibility 92

5 Conclusions **102**

Appendices **105**
Appendix A 106
Appendix B 110

Bibliography **112**

List of Figures

2.1 Baryon octet for spin 1/2 particles. . . . 12
2.2 Baryon decuplet for spin 3/2 particles. . . . 12
2.3 Meson nonet for spin 0 particles. . . . 13
2.4 Meson nonet for spin 1 particles. . . . 13
2.5 Symmetric lattice field strength tensor $F_{\mu\nu}(x)$. Figure taken from [40]. . . . 29
2.6 Dimension-6 operators for $\mathcal{O}(a^2)$-improvement of the Wilson gauge action, taken from[44]. The figure labelled (0) is the basic plaquette operator for the unimproved Wilson gauge action, whilst (1), (2) and (3) are for $\mathcal{O}_1$, $\mathcal{O}_2$ and $\mathcal{O}_3$ respectively. . . . 37
2.7 Stages of the thermalisation process for the QGP [52]. The system reaches local thermal equilibrium, then the QGP exists up until the point where chemical and thermal freezout occur, whereby hadronisation then takes place. . . . 45
2.8 Phase diagram for QCD, showing the state of strongly interacting matter across a range of values for temperature T and baryon chemical potential $\mu \equiv \mu_B$. This image was taken from [53]. . . . 45
2.9 A generic field $O(x,\tau)$ for positive flow time $\tau > 0$ depends on the value of the original unflowed field variable $O(x,0)$ within some local region of diameter $2\sqrt{8\tau}$. Figure taken from [55]. . . . 50

3.1 Figure taken from [68]. The derivative of the action density is shown against the flowtime for two levels of anisotropy, $\xi_w = \{2.8, 3.2\}$, where a difference of notation is noted by $\xi_w \equiv \gamma_w$. The spatial and temporal components switch order for the two anisotropy values, indicating that the renormalised gauge anisotropy lies between these values. Moreover the identification of $\gamma_w = \tilde{\gamma}_g$ is made for that value of γ_w where the spatial and temporal components are equal at $\hat{\tau} = \hat{\omega}_0^2$. . . . 56
3.2 Figure taken from [68]. The renormalised gauge anisotropy is determined using the Wilson flow, by determining the spatial $\hat{\omega}_0$ scale for various values of γ_w, and then determining the value of R_E at the point $\hat{\tau} = \hat{\omega}_0^2$. Within the lower panel the value of R_E/γ_w^2 is used on the vertical axis, such that condition eq. (3.14) is met at the unit value. The upper panel shows the interpolation of ω_0/a_s to the relevant point at $\gamma_w = \tilde{\gamma}_g$. . . . 57
3.3 $< \hat{E}_{st}(\hat{\tau}) >$ and $< \hat{E}_{ss}(\hat{\tau}) >$ vs $\hat{\tau}$ for various integrator step sizes ϵ (eps) for $\gamma_w = 1.00$. This data is for the N_t x $N_s^3 = 8$ x 32^3 ensemble. . . . 60
3.4 $< \hat{E}_{st}(\hat{\tau}) >$ and $< \hat{E}_{ss}(\hat{\tau}) >$ vs $\hat{\tau}$ for various integrator step sizes ϵ (eps) for $\gamma_w = 3.25$. This data is for the N_t x $N_s^3 = 8$ x 32^3 ensemble. . . . 60
3.5 $< \hat{E}_{st}(\hat{\tau}) >$ and $< \hat{E}_{ss}(\hat{\tau}) >$ vs $\hat{\tau}$ for various integrator step sizes ϵ (eps) for $\gamma_w = 3.35$. This data is for the N_t x $N_s^3 = 8$ x 32^3 ensemble. . . . 61
3.6 $< \hat{E}_{st}(\hat{\tau}) >$ and $< \hat{E}_{ss}(\hat{\tau}) >$ vs $\hat{\tau}$ for various integrator step sizes ϵ (eps) for $\gamma_w = 3.45$. This data is for the N_t x $N_s^3 = 8$ x 32^3 ensemble. . . . 61
3.7 $< \hat{E}_{st}(\hat{\tau}) >$ and $< \hat{E}_{ss}(\hat{\tau}) >$ vs $\hat{\tau}$ for various integrator step sizes ϵ (eps) for $\gamma_w = 3.55$. This data is for the N_t x $N_s^3 = 8$ x 32^3 ensemble. . . . 62
3.8 $< \hat{E}_{st}(\hat{\tau}) >$ and $< \hat{E}_{ss}(\hat{\tau}) >$ vs $\hat{\tau}$ for various integrator step sizes ϵ (eps) for $\gamma_w = 3.65$. This data is for the N_t x $N_s^3 = 8$ x 32^3 ensemble. . . . 62
3.9 $< \hat{E}_{st}(\hat{\tau}) >$ and $< \hat{E}_{ss}(\hat{\tau}) >$ vs $\hat{\tau}$ for various integrator step sizes ϵ (eps) for $\gamma_w = 1.00$. This data is for the N_t x $N_s^3 = 128$ x 32^3 ensemble. . . . 63
3.10 $< \hat{E}_{st}(\hat{\tau}) >$ and $< \hat{E}_{ss}(\hat{\tau}) >$ vs $\hat{\tau}$ for various integrator step sizes ϵ (eps) for $\gamma_w = 3.25$. This data is for the N_t x $N_s^3 = 128$ x 32^3 ensemble. . . . 63
3.11 $< \hat{E}_{st}(\hat{\tau}) >$ and $< \hat{E}_{ss}(\hat{\tau}) >$ vs $\hat{\tau}$ for various integrator step sizes ϵ (eps) for $\gamma_w = 3.35$. This data is for the N_t x $N_s^3 = 128$ x 32^3 ensemble. . . . 64

3.12 $< \hat{E}_{st}(\hat{\tau}) >$ and $< \hat{E}_{ss}(\hat{\tau}) >$ vs $\hat{\tau}$ for various integrator step sizes ϵ (eps) for $\gamma_w = 3.45$. This data is for the N_t x $N_s^3 = 128$ x 32^3 ensemble. 64
3.13 $< \hat{E}_{st}(\hat{\tau}) >$ and $< \hat{E}_{ss}(\hat{\tau}) >$ vs $\hat{\tau}$ for various integrator step sizes ϵ (eps) for $\gamma_w = 3.55$. This data is for the N_t x $N_s^3 = 128$ x 32^3 ensemble. 65
3.14 $< \hat{E}_{st}(\hat{\tau}) >$ and $< \hat{E}_{ss}(\hat{\tau}) >$ vs $\hat{\tau}$ for various integrator step sizes ϵ (eps) for $\gamma_w = 3.65$. This data is for the N_t x $N_s^3 = 128$ x 32^3 ensemble. 65
3.15 $< \hat{E}_{st}(\hat{\tau}) >$ and $< \hat{E}_{ss}(\hat{\tau}) >$ vs $\hat{\tau}$ for integrator step size $\epsilon = 0.015$ and $\gamma_w = 1.00$, at multiple temperatures. 66
3.16 $< \hat{E}_{st}(\hat{\tau}) >$ and $< \hat{E}_{ss}(\hat{\tau}) >$ vs $\hat{\tau}$ for integrator step size $\epsilon = 0.015$ and $\gamma_w = 3.65$, at multiple temperatures. 66
3.17 $< \hat{E}_{st}(\hat{\tau}) >$ and $< \hat{E}_{ss}(\hat{\tau}) >$ vs $\hat{\tau}$ for integrator step size $\epsilon = 0.015$ and $N_t = 8$, at multiple values of flow anisotropy γ_w. 67
3.18 $< \hat{E}_{st}(\hat{\tau}) >$ and $< \hat{E}_{ss}(\hat{\tau}) >$ vs $\hat{\tau}$ for integrator step size $\epsilon = 0.015$ and $N_t = 128$, at multiple values of flow anisotropy γ_w. 67
3.19 This data is for the N_t x $N_s^3 = 128$ x 32^3 ensemble, with an integrator step size of $\epsilon = 0.015$, using 990 configurations and with $\gamma_w = 3.65$. 69
3.20 This data is for the N_t x $N_s^3 = 128$ x 32^3 ensemble, with an integrator step size of $\epsilon = 0.015$, using 990 configurations. 69
3.21 Comparison of the output of the code, in this case the action density E_{ss} and E_{st} as a function of flow time $\hat{\tau}$, from Borsanyi et al, and the OpenQCD-FASTSUM code. This data is for the N_t x $N_s^3 = 128$ x 32^3 ensemble, with an integrator step size of $\epsilon = 0.015$. 70

4.1 The running gauge coupling as a function of flowtime for a lattice spacing of $a_s = 0.11208$ fm, computed using the approximate formula given in eq. (4.36). 84
4.2 Energy density vs flow time, computed using the gluonic contribution to the expectation value of the energy-momentum tensor. 84
4.3 Energy density vs flow time, computed using the gluonic contribution to the expectation value of the energy-momentum tensor. 85
4.4 Energy density vs flow time, computed using the gluonic contribution to the expectation value of the energy-momentum tensor. 85
4.5 Energy density vs flow time, computed using the gluonic contribution to the expectation value of the energy-momentum tensor. 86
4.6 Energy density vs flow time, computed using the gluonic contribution to the expectation value of the energy-momentum tensor. 86
4.7 Energy density vs flow time, computed using the gluonic contribution to the expectation value of the energy-momentum tensor. 87
4.8 Pressure vs flow time, computed using the gluonic contribution to the expectation value of the energy-momentum tensor. 87
4.9 Pressure vs flow time, computed using the gluonic contribution to the expectation value of the energy-momentum tensor. 88
4.10 Pressure vs flow time, computed using the gluonic contribution to the expectation value of the energy-momentum tensor. 88
4.11 Pressure vs flow time, computed using the gluonic contribution to the expectation value of the energy-momentum tensor. 89
4.12 Pressure vs flow time, computed using the gluonic contribution to the expectation value of the energy-momentum tensor. 89
4.13 Pressure vs flow time, computed using the gluonic contribution to the expectation value of the energy-momentum tensor. 90

4.14 Preliminary data for the energy density as a function of temperature. These values were extrapolated using eq. (4.20) with the coefficients set to $c_1 = c_2 = 1$. The errors within these plots are statistical only. 90
4.15 Preliminary data for the pressure as a function of temperature. These values were extrapolated using eq. (4.20) with the coefficients set to $c_1 = c_2 = 1$. The errors within these plots are statistical only. 91
4.16 This data is taken from the work of Suzuki et al [76]. The errors included within these plots are statistical only. 91
4.17 Topological susceptibility from the gauge definition $\chi^G_{top}(x,\tau)$, as a function of flow time τ/a_s^2. 96
4.18 Topological susceptibility from the gauge definition $\chi^G_{top}(x,\tau)$, as a function of flow time τ/a_s^2. 96
4.19 Topological susceptibility from the gauge definition $\chi^G_{top}(x,\tau)$, as a function of flow time τ/a_s^2. 97
4.20 Topological susceptibility from the gauge definition $\chi^G_{top}(x,\tau)$, as a function of flow time τ/a_s^2. 97
4.21 Topological susceptibility from the gauge definition $\chi^G_{top}(x,\tau)$, as a function of flow time τ/a_s^2. 98
4.22 Topological susceptibility from the gauge definition $\chi^G_{top}(x,\tau)$, as a function of flow time τ/a_s^2. 98
4.23 Topological susceptibility from the gauge definition $\chi^G_{top}(x,\tau)$, as a function of flow time τ/a_s^2. 99
4.24 Topological susceptibility vs temperature for the FASTSUM Gen2L ensembles and comparison against the work of Suzuki et al [93]. The work of Suzuki et al has a value $T_{pc} = 190$ MeV, with the FASTSUM Gen2L value being $T_{pc} = 162$ MeV. 99
4.25 Topological susceptibility vs temperature for the FASTSUM Gen2L ensembles and comparison against the work of Suzuki et al [93], including fits. 100
4.26 The figure is taken from fig.23 of [94], where the behaviour of χ^G_{top} vs T is understood in terms of the population of bonded and unbonded instantons. 100

List of Tables

2.1 Basic properties of the fundamental particles of the standard model of particle physics [24]. . . . 6
2.2 Spin 1/2 Baryons with quark content, electric charge and rest mass. . . . 13
2.3 Spin 3/2 Baryons with quark content, electric charge and rest mass. . . . 13
2.4 Spin 0 Mesons with quark content, electric charge and rest mass. . . . 14
2.5 Spin 1 Mesons with quark content, electric charge and rest mass. . . . 14
2.6 Parameters for the action used by the FASTSUM collaboration in order to generate (Gen2L) configurations with $N_f = 2 + 1$ flavours. The values for the bare anisotropy factors and the tadpole factors, and thus clover coefficients, were determined in [2], whilst the value for the strange quark mass was obtained in [46], and then the target renormalised anisotropy, pion mass, light quark masses and lattice spacings being determined in [47, 48]. Note that here $\tilde{\gamma}_f = a_s/a_t$ and represents the renormalised fermion anisotropy, whereas γ_g and γ_f represent the bare gauge and fermion anisotropy respectfully. . . . 40

3.1 Comparison of the known FASTSUM values and the values for this validation check of the anisotropic flow, for the spatial lattice spacing a_s and the renormalised anisotropy ($\tilde{\gamma}_g$ vs $\tilde{\gamma}_f$). This work was performed using the N_t x N_s^3 = 128 x 32^3 ensemble with 990 configurations. This is for the Gen2L data, the full parameter list for which can be found within table 2.6. The error on $\tilde{\gamma}_g$ for this work is statistical, with the first and second errors on a_s being statistical and systematic respectively. . . . 59
3.2 The data associated with fig. 3.19, which was computed for $\gamma_w = 3.65$. Note that the error for both a_s and $\tilde{\gamma}_g$ were computed via jackknife analysis on these final quantities, not at the level of the components of R_E or $\hat{E}(\hat{\tau})$, thus no error is quoted here for these intermediate quantities. . . . 68
3.3 The data associated with fig. 3.20. The determination of a_s involved determining the $\hat{w}_0$ value for each γ_w as shown in eq. (3.13) and presented here within this table. The $\hat{w}_0$ value for the renormalised gauge anisotropy where $\gamma_w = \tilde{\gamma}_g$ is then interpolated from this data. This is repeated for each jackknife re-sample and the final $\hat{w}_0$ with statistical error is thus determined, and used within the Δa_s computation shown in eq. (3.19). Thus at no point is there an error directly computed for the actual data points $\hat{w}_0$ given in this table, and hence they are quoted here without an associated error. Likewise the error on the final renormalised gauge anisotropy, $\Delta\tilde{\gamma}_g$, was determined by jackknife analysis, not the intermediate data presented within this table and thus no error is quoted here for R_E/γ_w^2. . . . 70

4.1 Temperature, maximum safe flow time $\tau_{1/2}$ and number of configurations for the FASTSUM Gen2L data, the parameters for which were specified within table 2.6. The temperatures are computed using $T = 1/(N_t a_t)$, where $a_t = 0.032459$ fm, and 1 fm $= 1/(197.3$ MeV). . . . 92
4.2 Energy density ϵ, and pressure p, as functions of temperature for the FASTSUM Gen2L data, the parameters for which were specified within table 2.6. The temperatures are computed using $T = 1/(N_t a_t)$, where $a_t = 0.032459$ fm, and 1 fm $= 1/(197.3$ MeV). The first error is statistical and the second is systematic. The goodness of fit parameters R^2 and χ^2_{dof} are included for both the energy density and pressure data. The data for $T = 47$ MeV has been omitted as it was used as the zero temperature data point in order to compute the vacuum expectation value required for eq. (4.20). . . . 93

4.3 Topological susceptibility using the gauge χ^G_{top} definition, for various temperatures using the FASTSUM Gen2L configurations. The first error on χ^G_{top} is statistical and the second is systematic. The plateau gradient is included to specify the flatness of the data within the plateau. The chi-squared per degree of freedom χ^2_{dof}, is included as the goodness of fit parameter. The plateau mean is the mean value within the fiducial window, and its systematic error was taken as the standard deviation of the values within the fiducial window. 95

Declaration

This work has not previously been accepted in substance for any degree and is not being concurrently submitted in candidature for any degree.

Signed [redacted]
Date 11/01/23

This thesis is the result of my own investigations, except where otherwise stated. Other sources are acknowledged by footnotes giving explicit references. A bibliography is appended.

Signed [redacted]
Date 11/01/23

I hereby give consent for my thesis, if accepted, to be available for photocopying and for inter-library loan, and for the title and summary to be made available to outside organisations.

Signed [redacted]
Date 11/01/23

The University's ethical procedures have been followed and, where appropriate, that ethical approval has been granted.

Signed [redacted]
Date 11/01/23

Date of Viva and Signatures of Examiners

Details of examiner 1 (external)

Signiture:
Date:

Details of examiner 2 (internal)

Signiture:
Date:

Details of viva chairperson

Signiture:
Date:

Results of viva - pass with major corrections on 08/07/2022.

Acknowledgements

I would like to thank my project supervisors Professor Simon Hands and Professor Chris Allton and also Gert Aarts for the opportunity to complete this PhD and for their guidance and time given throughout the project. I would also like to thank the department of physics at Swansea university for allowing me to complete my PhD degree with them. Furthermore I would like to thank the STFC for funding my PhD in its entirety. Finally I would like to thank my assessors for taking the time to evaluate my thesis and perform the viva examination.

Chapter 1

Motivation and Context

In the early universe, roughly $10^{-5}s$ after the big bang, space was filled with a deconfined state of matter composed of asymptotically free quarks and gluons, known as the Quark Gluon Plasma. As the universe expanded and thus cooled, a transition occurred into a confined state of hadronic matter. Understanding how this strongly interacting matter behaves under such conditions is important for explaining how the universe evolved into what is seen today, and is of interest to cosmology and astro-particle physics. Such conditions are probed experimentally at facilities such as the Relativistic Heavy Ion Collider which collides nuclei as heavy as gold, and the Large Hadron Collider which collides heavier nuclei such as lead. From the theoretical side of the coin, much of the work is done using hydrodynamics, which requires the input of thermodynamic quantities. These quantities require the use of non-perturbative first principles methods, with the predominant method being lattice field theory.

Initial attempts to compute thermodynamic quantities on the lattice involved using the known equations of statistical mechanics, and reformulating them in terms of actions rather than partition functions, the latter of which is not a-priori known on the lattice. These methods, such as the derivative method and the integral method, require many simulations in a large multi-dimensional parameter space, and are thus very computationally expensive. The ideal scenario would be to directly compute the energy-momentum tensor on the lattice, and thus have direct access by first principle calculations to thermodynamic quantities for high temperature QCD.

Alas, this is a significantly difficult task in itself, as whilst the lattice formulation of quantum field theory respects gauge invariance, it explicitly violates Lorentz invariance which is only regained when taking the naive continuum limit. The energy-momentum tensor is the conserved Nöether current of translational invariance, which is violated on the explicitly discrete lattice. Determining a correct definition of the energy-momentum tensor thus poses a significant challenge.

However a new tool has emerged in recent years, which has been used on the lattice to help with several problems, from scale setting, filtering ultraviolet fluctuations, and dealing with issues of renormalisation. This tool, known as Yang-Mills gradient flow has been used in order to define the energy-momentum tensor on the lattice, allowing for QCD to be more readily explored. In particular

an approach based on the small flow-time expansion has been used to great success.

Anisotropic lattices [1, 2], with different lattice spacings in the spatial and temporal directions are often employed in order to achieve fine sampling of the temporal direction whilst keeping the sampling in the spatial direction relatively coarse. This enables fine sampling of temperature, whilst avoiding the accumulation of small volume errors, and without incurring unacceptable computational expense. This is particularly important when studying temporal correlation functions which decay rapidly, as a sufficient temporal sampling can then be obtained without facing issues of small volume effects (rapid signal decay), permitting a more accurate determination of large masses [3].

One of the original motivating factors behind anisotropic lattices is that larger bare quark masses, m_q, result in uncontrolled systematic errors for $a > 1/m_q$ when using the naive action that one might use for the lighter quarks [4–6]. One common method to get around this is the lattice implementation of what is known as Non-Relativistic QCD (NRQCD) which is valid for $a > 1/m_q$. NRQCD describes a low energy effective field theory, with the action expanded in powers of lattice spacing a and powers of the heavy quark velocity v^2. One of the difficulties of NRQCD is that the very requirement that makes it interesting for heavy bare quark mass, $a > 1/m_q$, also makes a continuum extrapolation difficult.

Another common approach to this issue is the heavy-relativistic approach, also known as the Fermilab approach, which utilises interactions from both the low and high mass limits in such a way that large masses can be viewed in a non-relativistic manner, whereas the light masses result in the more familiar Wilson action. The down side is that the improvement coefficients for heavy quarks are now mass dependant.

The anisotropic lattice allows for the condition $a_t m_q < 1$ to be met whilst $a_s m_q \approx 1$, avoiding the need for either of these specialised approaches and side stepping the original issue that the isotropic lattice experienced. Anisotropic lattices are thus well placed for heavy quark studies [7, 8], as well as other topics such as the glueball spectrum [9, 10]. The down side is that there are now more parameters that require tuning.

The focus of the FASTSUM collaboration is to study the hadronic spectrum and transport properties of QCD at non-zero temperature. For this the group utilises an anisotropic lattice, although use of other methods such as NRQCD are employed also. A broad sample of the work from the FASTSUM collaboration can be found in the following references [11–18]. A long term major goal of the collaboration is to non-perturbatively compute the QCD viscosity with a good sampling over temperature. One of the possible approaches to this is to compute the correlation function of the energy-momentum tensor on the lattice [19–22], which can be obtained via the gradient flow method. It is hoped that due to the anisotropic lattice, the viscosity should be better sampled across temperature than for the isotropic lattice computations performed by other groups. The motivation for the work presented within this thesis is to serve as an initial feasibility study by looking at various thermodynamic properties computed using gradient flow on the FASTSUM anisotropic lattice setup. The focus will be on the expectation value of the energy-momentum tensor, providing information on

the energy and pressure as functions of temperature. The topological susceptibility is also of interest in cosmology [23], and will be used as a second test of the gradient flow on the anisotropic lattice. The key objectives of this work are to try the new technology of the gradient flow on the FASTSUM configurations so as to determine their suitability for thermodynamic studies, and to perform the first thermodynamic computations in full $N_f = 2 + 1$ QCD on the anisotropic lattice.

This thesis is organised as follows: In chapter 2 the prerequisite content for studying QCD on the lattice is covered, as well as the specific details for the lattice setup of the FASTSUM collaboration, and the initial introduction to the gradient flow. Then chapter 3 covers the validation test for the anisotropic gradient flow within the OpenQCD-FASTSUM code base, using the Gen2L configuration data, and provides the results for tests of numerical stability for the parameters of interest. In chapter 4 the background content for the lattice determination of the energy-momentum tensor is covered along with the topological susceptibility, and the main results for this thesis are provided. Finally chapter 5 will provide a brief summary of the results and consequences of the work presented within this thesis, and will discuss the next steps in this line of work.

Chapter 2

Theoretical Prerequisites

The Standard Model of particle physics is currently the best description for the fundamental interactions within the universe, and is described at high enough energies by the gauge group $SU(3)_C \times SU(2)_L \times U(1)_Y$. In the early moments of the universe, as the energy density decreased due to expansion, approximately 10^{-12} s after the big bang the Higgs potential was spontaneously broken and the Higgs field developed a non-zero vacuum expectation value (VEV). Consequently the electroweak symmetry $SU(2)_L \times U(1)_Y$ was spontaneously broken, resulting in the mixing of the coupling constants and the resultant weak gauge bosons being massive. This spontaneous symmetry breaking is also responsible for the leptons acquiring their mass, as in the earliest moments of the universe they were massless. The current state of the universe is thus such that the fundamental interactions are described by the exact gauge symmetry $SU(3)_C \times U(1)_{EM}$, and the broken gauge symmetry $SU(2)_L$.

Every particle within the standard model must transform under some representation of each of the above subgroups, even if only trivially. The fundamental matter components are the 12 spin 1/2 Fermions, composed of 6 leptons and 6 quarks, both of which are split into 3 generations;

$$\begin{pmatrix} \nu_e \\ e \end{pmatrix}_L \begin{pmatrix} \nu_\mu \\ \mu \end{pmatrix}_L \begin{pmatrix} \nu_\tau \\ \tau \end{pmatrix}_L \begin{pmatrix} u \\ d \end{pmatrix}_L \begin{pmatrix} c \\ s \end{pmatrix}_L \begin{pmatrix} t \\ b \end{pmatrix}_L , \tag{2.1}$$

with the first three doublets being the three generations of leptons, followed by the three generations of quarks. All of the doublets are left handed due to the $SU(2)_L$ weak interactions only acting on left handed matter[1]. The leptons carry weak charge, with the electron, muon and tau also carrying electric charge. The quarks carry weak, electric and strong charges. There is one type of electric charge, two types of weak charge and three types of strong charge.

The forces are mediated by the gauge bosons, with the photon mediating $U(1)_{EM}$ interactions, the $W^\pm$ and Z^0 bosons mediating the $SU(2)_L$ interactions and the 8 gluons mediating the $SU(3)_C$ interactions. For every particle within the standard model their exists a corresponding charge conjugated

[1] Strictly speaking the right handed matter transforms trivially under $SU(2)_L$ and is thus in a singlet state. Similarly, the weak interactions only act non-trivially on right handed anti-matter, with the left handed anti-matter transforming trivially as a singlet.

antiparticle which is identical except for opposite quantum numbers, with some particles acting as their own antiparticle. The properties of these fundamental particles are presented in table 2.1.

Particle	Spin	Electric Charge	Mass Gev/c^2
$W^{\pm}$	1	±1	80.379(12)
Z^0	1	0	91.1876(21)
Photon (γ)	1	0	0
Gluon (g)	1	0	0
Higgs boson (H)	0	0	125.10(14)
Electron (e)	1/2	-1	$0.5109989461(31)\cdot10^{-3}$
Muon (μ)	1/2	-1	$105.6583745(24)\cdot10^{-3}$
Tau (τ)	1/2	1	1.77686(12)
Electron neutrino (ν_e)	1/2	0	-
Muon neutrino (ν_μ)	1/2	0	-
Tau neutrino (ν_τ)	1/2	0	-
Up (u)	1/2	2/3	$2.16(+49)(-26)\cdot10^{-3}$
Down (d)	1/2	$-1/3$	$4.67(+48)(-17)\cdot10^{-3}$
Strange (s)	1/2	$-1/3$	$93(+11)(-5)\cdot10^{-3}$
Charm (c)	1/2	2/3	1.27(2)
Bottom (b)	1/2	$-1/3$	4.18(+3)(-2)
Top (t)	1/2	2/3	172.9(4)

Table. 2.1: Basic properties of the fundamental particles of the standard model of particle physics [24].

The term model suggests that there are external inputs that cannot be determined by the underlying mechanics framework. There are in-fact 25 input parameters, corresponding to; the mass of the 6 leptons, the mass of the 6 quarks, the Higgs mass, the electric, strong and weak couplings constants (g_e, g_s, θ_w), the 4 CKM matrix mixing angles, the 3 neutrino mixing angles, one phase and the Higgs field amplitude[2]. The framework underpinning the Standard Model is Quantum Field Theory (QFT), which is the combination of relativistic and quantum mechanical frameworks, specifically utilising a field theoretic description.

The Standard Model predictions have been vindicated by many experiments, from the prediction and discovery of the Higgs boson to that of the anomalous magnetic dipole moment of the electron. However, despite tremendous success to date, it is clear that the Standard Model in its present formulation can not be the final description of nature on the most fundamental level. In its present incarnation the Standard Model fails to explain the matter-antimatter asymmetry, the nature of dark matter and dark energy, the equal magnitude for the charge of the proton and electron and then there is the issue of the large disparity in coupling for the three forces at low energy. Perhaps the largest issue is that there is no mention of one of the fundamental forces, with the gravitational force absent due to the complexities of a quantum formulation.

[2]The Higgs field is actually a doublet with components ϕ_1 and ϕ_2, which are rotated under weak interactions. The Higgs field amplitude is $v = 246$ GeV, and is the vacuum expectation value of the non-zero component after spontaneous symmetry breaking, with $\phi_1 = v$ and $\phi_2 = 0$. The field amplitude can be expressed in terms of the couplings of the Higgs Lagrangian density $-\mu^2(\phi_1^2 + \phi_2^2)/2 + \lambda^2(\phi_1^2 + \phi_2^2)^2/4$, with $v = \mu/\lambda$ [25].

Furthermore the Standard Model is believed to be an effective theory describing the degrees of freedom that are relevant on the length and energy scales that we currently have experimental access to. It is believed that the electroweak sector $SU(2)_L \times U(1)_Y$ is valid only up to some cutoff energy scale. This is similar to non-relativistic QFT which is utilised within condensed matter physics acting as an effective theory to standard (relativistic) QFT, where the theory correctly describes the degrees of freedom which are relevant to physics at the energy and length scales of condensed matter systems. The standard model effective theory is expected to be replaced at energies on the Plank scale with a theory that involves some formulation of gravity with quantum mechanics, with two of the main present candidates being string theory and loop quantum gravity. However $SU(3)_C$ which is the gauge group of Quantum Chromodynamics (QCD) is in principle valid up to arbitrary energy scales and is in fact a very well tested theory.

2.1 Continuum QCD

The fundamental constituents of QCD are the gluon fields A^a_μ and the quark fields $\psi^{i\alpha}_f$.The gluon fields sit in the adjoint representation of $SU(3)_C$, and as such the colour index takes the values $a = 1, ..., N_c^2 - 1$, whereas the quark fields sit in the fundamental representation and thus $i = 1, ..., N_c$. Moreover the quark fields are endowed with a flavour index $f = 1, ..., N_f$ and also a spinor index $\alpha = 1, 2, 3, 4$, whilst the gluon gauge fields possess a Lorentz index $\mu = 0, 1, 2, 3$. Physical QCD contains three colour charges called red, green and blue, for reasons that will be explained shortly, and thus $N_c = 3$. Furthermore there are six quark flavours; up, down, strange, charm, bottom and top, and hence $N_f = 6$.

In the 1950's the strong nuclear force had become a hot bed of frustration for physicists with a large number of new particles being discovered, with a clear need for some form of classification. The particles were initially classified based on their isospin, and subsequently by the eight fold way of Gell-Mann [26], who would later suggest that these particles were made up of more fundamental matter which he named quarks. As is turned out, the groundwork had already began in 1954 for the modern description of the strong force, that being Yang-Mills (YM) theory which describes the gauge degrees of freedom for QCD. However it wasn't immediately clear that YM theory was applicable to the strong interactions, with one of the first key steps in this story being the work of 't Hooft and Veltman in 1972 showing that YM theory was renormalisable and could thus give meaningful predictions to compare against experiment [27]. Furthermore in 1973 it was independently shown by Wilczek and Gross [28], and also by Politzer [29], that the running of the coupling constant with energy scale is in fact a feature of QFT. In the context of the strong interactions this results in asymptotic freedom whereby the quarks interact so weakly at large enough energy scales so as to be essentially quasi-free particles with negligible strong interacts. Consequently an asymptotically free QFT could describe the strong interactions at sufficiently high energy, whence YM theory became a candidate as it meets the requirement of being asymptotically free. The deep inelastic scattering experiments of the 1960's had convinced many that Gell-Mann's quarks may be real. However the

observed production rates in electron anti-electron collisions of hadrons versus muon anti-muon pairs was three times larger than anticipated, suggesting that there were three times as many quarks than previously believed. This triplicate of quarks were identical in all ways, including electric charge and mass, except for some new feature that distinguished them from one another. It was later realised that quarks only exist in certain combinations of this distinguishing feature, and thus this characteristic would be named colour charge[3]. It is this symmetry of the three types of quarks that would reveal the required exact gauge symmetry which YM theory required in order to describe the strong interactions, and would thus reveal the gauge group of QCD to be $SU(3)_C$, where the subscript makes explicit the symmetry being with respect to the colour charge rather than quark flavour.

Further evidence for the existence of colour charge came from the discovery of the ground state Δ^-, Δ^{++} and Ω^- spin 3/2 Baryons, which have three down, up, and strange quarks respectively. The Pauli exclusion principle prohibits multiple Fermions from existing in the same state, and thus indicates that there must exist some additional characteristic with at least three possible values which permits these Fermions to exist in different states. The aforementioned production rates showed three types of quarks, implying that there are in fact precisely three colour charges and that quarks must each carry a single colour, otherwise in each case there would be more than three types of quark. It is clear from the fact that this colour charge doesn't appear in most experiments that all observed bound states must be colour singlets, which are invariant under $SU(3)_C$ transformations. This is known as colour confinement whereby no individual long lived colour charged particle may exist in nature. The reason for the gauge group not being $U(3)$ is that this would require the existence of a long range gluon, which would in turn endow the strong nuclear interaction with a long range component which is not observed in experiment. This is another expression of colour confinement as the gluons are themselves carriers of colour charge and thus can't exist as free particles. Furthermore, given that there are three colour charges, the observation of Mesons which are two-quark bound states suggests that in order for these bound states to be colour singlets, they must contain one colour and a corresponding anti-colour. Subsequently, the gluons must then be bi-colour and must themselves carry one unit of colour and one of anti-colour in order to mediate the interactions within the Meson.

The YM Lagrangian density for QCD[4] is shown here with the Minkowski metric;

$$\mathcal{L}_{gluon} = -\frac{1}{4}\sum_{a=1}^{N_c^2-1} F_a^{\mu\nu}(x)F^a_{\mu\nu}(x), \tag{2.2}$$

[3]The term colour charge is inspired by the observation that all observable particles which are charged under $SU(3)_C$ exist in bound states which possess zero net colour charge. The name is in analogy to sunlight, which contains all wavelengths of light and yet appears to be colourless overall.

[4]For the sake of clarity it should also be stated that the gauge field A_μ for QCD ($N_c = 3$) is thus a 4 component Lorentz vector, with each of those components themselves being an 8 component colour vector. Likewise, the quark field (dropping the flavour index f for a moment) $\psi^{i\alpha}$ is a 3 component colour vector, with each of those components themselves being a 4 component spinor. The inclusion of the free flavour index f further highlights that the expression holds true for each of the 6 quark flavours, all of which contribute to the Lagrangian density.

with the field strength tensor components[5] $F^a_{\mu\nu}(x)$ given by;

$$F^a_{\mu\nu}(x) = \partial_\mu A^a_\nu(x) - \partial_\nu A^a_\mu(x) + g f^{abc} A^b_\mu(x) A^c_\nu(x), \tag{2.3}$$

where f^{abc} are the structure constants for $\mathfrak{SU}(3)$. The QCD Lagrangian density is then given by;

$$\mathcal{L}_{QCD} = \mathcal{L}_{gluon} + \mathcal{L}_{quark}, \tag{2.4}$$

where the fermion matter is described by;

$$\mathcal{L}_{quark} = \sum_{f=1}^{N_f} \sum_{i,j=1}^{N_c} \sum_{\alpha,\beta=1}^{4} \bar{\psi}^{i\alpha}_f(x)(i\not{D}^{ij}_{\alpha\beta} - m_f \delta_{ij}\delta_{\alpha\beta})\psi^{j\beta}_f(x), \tag{2.5}$$

with bare mass m_f. The gauge covariant derivative[6] is given by;

$$\not{D}_{ij,\alpha\beta} = \gamma^\mu_{\alpha\beta}(\partial_\mu \delta_{ij} + i g T^a_{ij} A^a_\mu(x)) : T^a_{ij} = \frac{\lambda^a_{ij}}{2}, \tag{2.6}$$

with g being the bare coupling constant for the strong force, $A^a_\mu(x) \in \mathbb{R}$ and T^a_{ij} being the $\mathfrak{SU}(3)$ Lie algebra generators which include the Gell-Mann matrices[7] λ^a_{ij}. The structure constants also relate to the generators T^a via the Lie algebra where from this point on the spinor, flavour and colour indices will be omitted for simplicity whenever there exists no ambiguity;

$$[T^a, T^b] = i f^{abc} T^c : \mathrm{Tr}(T^a T^b) = \frac{1}{2}\delta^{ab}, \tag{2.7}$$

with the latter being a normalisation convention. The hermitian and traceless Lie algebra generators are related to the Lie group elements Ω[8] through the exponential map, specified here for $SU(3)_C$;

$$\Omega \equiv \Omega_\mu = e^{iT^a A^a_\mu} \in SU(3)_C, \tag{2.8}$$

where the group elements are unitary 3x3 matrices with unit determinant;

$$\Omega^\dagger \Omega = \Omega \Omega^\dagger = 1; \ \mathrm{det}\Omega = 1. \tag{2.9}$$

[5]The field strength is related to its components via $F_{\mu\nu ij}(x) \equiv F_{\mu\nu}(x) = F^a_{\mu\nu}(x) T^a_{ij}$, where the fundamental representation colour indices i, j are typically omitted for the field strength tensor $F_{\mu\nu}$. The field strength tensor can be thought of as a 4x4 matrix in spacetime (hence Lorentz indices $\mu\nu$), with each component being a 3x3 matrix in the fundamental representation of colour space.

[6]As with the fields, the indexing $\not{D}^{ij}_{\alpha\beta}$ should be understood as a 3x3 colour matrix, whose components are themselves 4x4 spinor matrices. The terms colour matrix and spinor matrix refer to the space in which the matrices act non-trivially, with a trivial effect to objects or indices belonging to any another space.

[7]It should be noted that the gauge field $A_\mu(x)$, which is a Lorentz vector, is related to the Gell-Mann matrices via $A_\mu(x) = A^a_\mu(x) T^a_{ij}$, and that each element of the Lorentz vector is thus a 3x3 traceless hermitian matrix in colour space.

[8]Note that eq. (2.8) is actually four equations in one, with one equation for each of the Lorentz vector indices. From this point on the Lorentz index μ will be dropped with the tacit understanding that one arbitrary value of the Lorentz index is being discussed at a time.

The Dirac matrices γ^μ in eq. (2.6) are defined through an anti-commutator relation via the Clifford algebra;

$$\{\gamma^\mu, \gamma^\nu\} = -2\eta^{\mu\nu}\mathcal{I}_4 : \gamma_\mu = \eta_{\mu\nu}\gamma^\nu, \tag{2.10}$$

where $\mathcal{I}_4$ is the 4x4 identity matrix, $\eta^{\mu\nu}$ is the Minkowski metric with signature $(-+++)$ and the exact form of the matrices γ^μ depends on the choice of basis.

The statement that QCD is described by the $SU(3)_C$ gauge symmetry is precisely the requirement that the Lagrangian density $\mathcal{L}_{QCD}$ be invariant under the simultaneous local transformations for the quark and gluon fields;

$$\psi(x) \to \psi^{'}(x) = \Omega(x)\psi(x), \tag{2.11}$$

$$\bar{\psi}(x) \to \bar{\psi}^{'}(x) = \bar{\psi}(x)\Omega^\dagger(x), \tag{2.12}$$

$$A_\mu(x) \to \Omega(x)A_\mu(x)\Omega^\dagger(x) - i\Omega(x)\partial_\mu\Omega^\dagger(x), \tag{2.13}$$

where eq. (2.12) is the transformation rule for the anti-quark field, which is given by $\bar{\psi} \equiv \psi^\dagger\gamma^0$. The quark field is expressed as a colour triplet of quarks which are equal in all but their colour charge;

$$\psi = \begin{pmatrix} \psi_r \\ \psi_b \\ \psi_g \end{pmatrix}, \tag{2.14}$$

where the subscripts represent the colour charge that the given quark possesses , which again are referred to as red, blue and green. The global $SU(3)_C$ gauge symmetry results via Nöether's theorem, in 8 independently conserved quantities (the gauge field components A^a_μ), one for each of the Lie algebra generators T^a. However only two of these T^a are Cartan generators, that is, those generators which are diagonal. Moreover it is only for diagonal generators that all three components of the quark colour triplet ψ can have have a definite value assigned, as the components ψ_r,ψ_b and ψ_g aren't eigenstates of the other generators. In one particular choice of basis for the $SU(3)$ matrices, the Cartan generators are given by[9];

$$T_3 \equiv \frac{\lambda_3}{2} = \frac{1}{2}\begin{pmatrix} 1 & 0 & 0 \\ 0 & -1 & 0 \\ 0 & 0 & 0 \end{pmatrix}, T_8 \equiv \frac{\lambda_8}{2} = \frac{1}{2\sqrt{3}}\begin{pmatrix} 1 & 0 & 0 \\ 0 & 1 & 0 \\ 0 & 0 & -2 \end{pmatrix}, \tag{2.15}$$

with the corresponding eigenvalue equations;

$$(T_3, T_8)\begin{pmatrix} 1 \\ 0 \\ 0 \end{pmatrix} = \left(\frac{1}{2}, \frac{1}{2\sqrt{3}}\right)\begin{pmatrix} 1 \\ 0 \\ 0 \end{pmatrix}, \tag{2.16}$$

[9]The placement of the colour indices as being upper or lower is arbitrary and means the same thing in each instance, unlike with the Lorentz indices where the placement is significant. This could be phrased as the metric on the colour space being the identity.

$$(T_3, T_8) \begin{pmatrix} 0 \\ 1 \\ 0 \end{pmatrix} = \left(\frac{-1}{2}, \frac{1}{2\sqrt{3}} \right) \begin{pmatrix} 0 \\ 1 \\ 0 \end{pmatrix}, \tag{2.17}$$

$$(T_3, T_8) \begin{pmatrix} 0 \\ 0 \\ 1 \end{pmatrix} = \left(0, \frac{-1}{\sqrt{3}} \right) \begin{pmatrix} 0 \\ 0 \\ 1 \end{pmatrix}. \tag{2.18}$$

The Cartan generators commute, and as such all three eigenvectors of the triplet are each simultaneous eigenstates of T_3 and T_8. Consequently these eigenvalue pairs, which are conserved quantities, are used to label particles. The eigenvalue pairs in eq. (2.16), eq. (2.17) and eq. (2.18) are precisely the labels that are used to specify red, blue and green colour charge. Due to the eigenvector basis being orthogonal the triplet can be either in a definite eigenstate of colour or a linear combination of all three colours. It is prudent to note that these values do not constitute three values of the same colour charge, but rather three distinct types of charge. Furthermore, all colour charge neutral particles are assigned colour singlet states, which transform trivially under $SU(3)_C$.

The gluons transform under the adjoint representation of $SU(3)_C$, and are composed of a linear combination of the bi-colour octet states;

$$\begin{aligned} |1\rangle &= \frac{1}{\sqrt{2}}(r\bar{b} + b\bar{r}), & |2\rangle &= \frac{-i}{\sqrt{2}}(r\bar{b} - b\bar{r}), \\ |3\rangle &= \frac{1}{\sqrt{2}}(r\bar{r} - b\bar{b}), & |4\rangle &= \frac{1}{\sqrt{2}}(r\bar{g} + g\bar{r}), \\ |5\rangle &= \frac{i}{\sqrt{2}}(r\bar{g} - g\bar{r}), & |6\rangle &= \frac{1}{\sqrt{2}}(b\bar{g} + g\bar{b}), \\ |7\rangle &= \frac{-i}{\sqrt{2}}(b\bar{g} - g\bar{b}), & |8\rangle &= \frac{1}{\sqrt{6}}(r\bar{r} + b\bar{b} - 2g\bar{g}), \end{aligned} \tag{2.19}$$

where each basis vector transforms non-trivially under $SU(3)_C$, irrespective of the overall colour. Colour confinement requires the quarks and gluons to exist in bound states, which come in quark anti-quark pairs called Mesons or triplets of quarks or anti-quarks called Baryons. In each instance the bound state must be in an overall colour singlet state, which for integer spin Mesons is given by the symmetric colour combination;

$$|\text{singlet}\rangle = \frac{1}{\sqrt{3}}(r\bar{r} + b\bar{b} + g\bar{g}), \tag{2.20}$$

and for half-integer spin Baryons it is given by the anti-symmetric combination;

$$|\text{singlet}\rangle = \frac{1}{\sqrt{6}}(rgb - rbg + gbr - grb + brg - bgr). \tag{2.21}$$

Furthermore Gell-Mann showed that the spin 1/2 Baryons can be organised into an octet based on

a separate $SU(3)$ vector flavour symmetry, fig. 2.1, and the spin 3/2 Baryons can be organised into a decuplet, fig. 2.2.

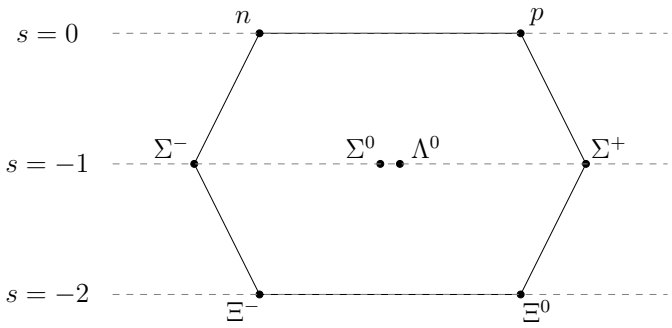

Fig. 2.1: Baryon octet for spin 1/2 particles.

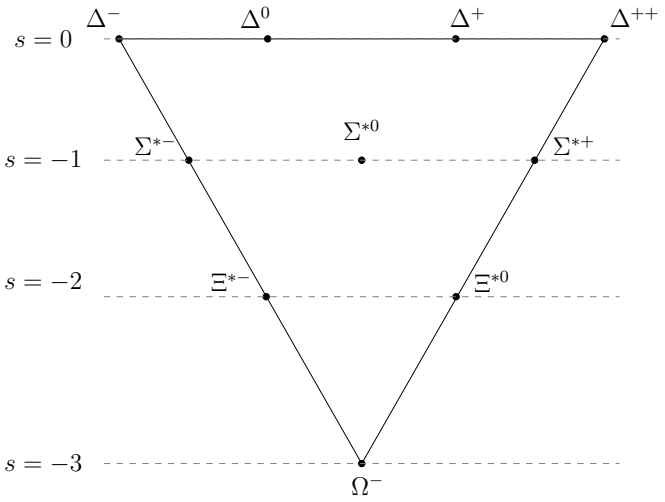

Fig. 2.2: Baryon decuplet for spin 3/2 particles.

The octet contains three rows, where the inhabitants of a given row contain a given number of strange quarks[10] and have a very similar mass. This is made explicit by the corresponding data within table 2.2 and table 2.3. Similarly there is a diagonal (\) pattern to the electric charge. Baryons are three body systems and as such they contain two angular momenta. The aforementioned particles are in the ground state where the angular momenta $l = l' = 0$. The difference between the Σ^0 and Λ^0 lies in the details of the wave function and results in Σ^0 having isospin of 1 whereas Λ^0 has isospin 0.

The seven Baryons within fig. 2.2 which are not located at the corners of the dectet can be thought of as excitations of those within fig. 2.1. The masses of the Baryons are considerably heavier than the masses of the constituent quarks[11] due to the non-abelian nature of the theory, whereby due to the nonzero structure constants in eq. (2.7), the gluons self-interact and create a dynamically generated mass. Consequently if the Higgs field were to lose its non-zero VEV and result in massless quarks, the Baryons and indeed all nuclei would still be massive, and moreover the reduction in mass would be almost negligible. The underlying chiral symmetry breaking is explained within chapter 5.

The ground state Mesons can also be characterised by a similar nonet pattern with spin 0 particles in fig. 2.3, and spin 1 particles in fig. 2.4, and the corresponding data presented in table 2.4 and table 2.5 respectively.

Similar to the case of the Baryons, the spin 1 Mesons can be thought of as excitations of the spin 0 Mesons, with the exception of η and η' having distinct quark content from ϕ and ω. However the masses for each row of particles are not as consistent as with the Baryons, with the pions being

[10]Strangeness, i.e. the number of strange quarks minus anti-strange quarks, is conserved by the strong and electromagnetic interactions but not by the weak interactions. In this sense strangeness is a conserved quantity within the context of QCD. It should also be noted that particles with different quark content thus experience different lifetimes, with strong interactions occurring on a timescale of $10^{-22} - 10^{-24}$ s, electromagnetic interactions $10^{-16} - 10^{-21}$ s and for weak interactions $10^{-7} - 10^{-13}$ s.

[11]The masses of the three lighter quarks are approximately; $m_u \approx 2$ MeV/c^2, $m_d \approx 5$ MeV/c^2 and $m_s \approx 95$ MeV/c^2.

Particle : Quarks	Electric Charge	Mass Mev/c^2
$n : udd$	0	939.5654133(58)
$p : uud$	1	938.2720813(58)
$\Sigma^- : dds$	-1	1197.449(30)
$\Sigma^0 : dus$	0	1192.642(24)
$\Lambda^0 : dus$	0	1115.683(6)
$\Sigma^+ : uus$	1	1189.37(7)
$\Xi^- : dss$	-1	1321.71(7)
$\Xi^0 : uss$	0	1314.86(20)

Table. 2.2: Spin 1/2 Baryons with quark content, electric charge and rest mass.

Particle : Quarks	Electric Charge	Mass Mev/c^2
$\Delta^- : ddd$	-1	1232(2)
$\Delta^0 : udd$	0	1232(2)
$\Delta^+ : uud$	1	1232(2)
$\Delta^{++} : uuu$	2	1232(2)
$\Sigma^{*-} : dds$	-1	1387.2(5)
$\Sigma^{*0} : dus$	0	1383.7(10)
$\Sigma^{*+} : uus$	1	1382.80(35)
$\Xi^{*-} : dss$	-1	1535.0(6)
$\Xi^{*0} : uss$	0	1531.80(32)
$\Omega^- : sss$	-1	1672.45(29)

Table. 2.3: Spin 3/2 Baryons with quark content, electric charge and rest mass.

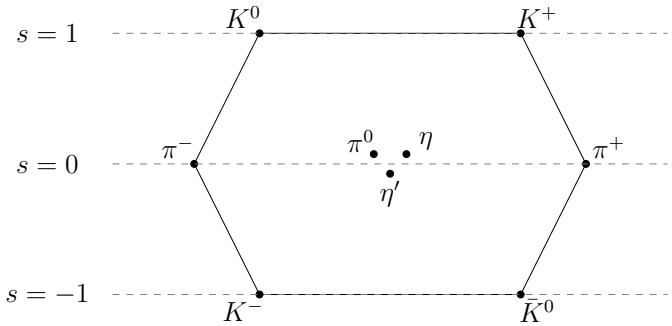

Fig. 2.3: Meson nonet for spin 0 particles.

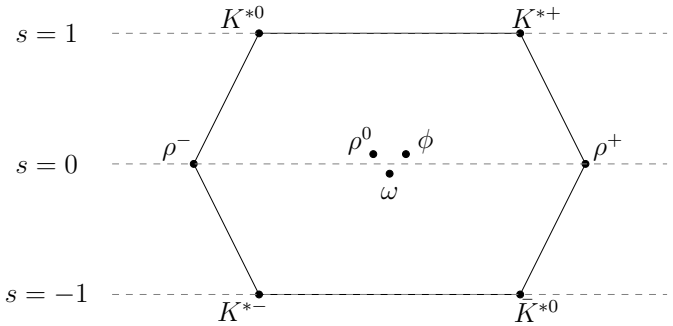

Fig. 2.4: Meson nonet for spin 1 particles.

rather lighter due to the lack of any strange quark. The η' is substantially heavier than all other spin 0 Mesons due to a subtlety of QFT called the axial-anomaly. Another stark contrast between the Baryons and the Mesons is that the Baryons are all of a definite quark composition, whereas some of the Mesons are formed of a linear combination of constituent quarks. Furthermore, unlike for the case of Baryons, if the masses of the quarks were zero then the mass of all Mesons would also vanish, with the pions, kaons and eta being Nambu-Goldstone bosons, which is related to chiral symmetry breaking[12].

The Mesons and Baryons presented above are by no means an exhaustive list, with many excitations possible and along with heavier particles that contain charm and bottom quarks. However the work presented within this thesis does not pertain to QCD spectroscopy and thus such details are beyond the scope of this prerequisites section. On a similar note it should be briefly mentioned that the residual strong interaction which binds nucleons together within the nucleus, is in fact a complicated manifestation of the strong interaction whereby spin 0 Mesons are exchanged between the nuclei, and was predicted by Yukawa in 1935.

The running coupling for QCD varies with energy in such a way so as to create quasi-free gluons and quarks at small distance scales, or equivalently high energy. This characteristic is known as

[12]See chapter 5 for a summary of chiral symmetry.

Particle : Quarks	Electric Charge	Mass Mev/c^2
$K^0 : d\bar{s}$	0	497.614(24)
$K^+ : u\bar{s}$	1	93.677(16)
$\pi^- : d\bar{u}$	-1	139.57018(35)
$\pi^0 : (u\bar{u} - d\bar{d})/\sqrt{2}$	0	134.9766(6)
$\eta : (u\bar{u} + d\bar{d} - 2s\bar{s})/\sqrt{6}$	0	547.853(24)
$\eta' : (u\bar{u} + d\bar{d} + s\bar{s})/\sqrt{3}$	0	957.66(24)
$\pi^+ : u\bar{d}$	1	139.57018(35)
$K^- : s\bar{u}$	-1	493.677(16)
$\bar{K}^0 : s\bar{d}$	0	497.614(24)

Table. 2.4: Spin 0 Mesons with quark content, electric charge and rest mass.

Particle : Quarks	Electric Charge	Mass Mev/c^2
$K^{*0} : d\bar{s}$	0	896.000(25)
$K^{*+} : u\bar{s}$	1	891.660(26)
$\rho^- : d\bar{u}$	-1	775.4(4)
$\rho^0 : (u\bar{u} - d\bar{d})/\sqrt{2}$	0	775.49(34)
$\phi : s\bar{s}$	0	1019.445(20)
$\omega : (u\bar{u} + d\bar{d})/\sqrt{2}$	0	782.65(12)
$\rho^+ : u\bar{d}$	1	775.4(4)
$K^{*-} : s\bar{u}$	-1	891.660(26)
$\bar{K}^{*0} : s\bar{d}$	0	896.000(25)

Table. 2.5: Spin 1 Mesons with quark content, electric charge and rest mass.

asymptotic freedom, and is responsible for the successful application of perturbation theory at high energies. However perturbation theory fails once the coupling becomes sufficiently large, which occurs when considering interactions on a distance scale of $10^{-14} - 10^{-15}$ m, or equivalently at energy scales around $\Lambda_{QCD} \approx 200$ MeV, which is known as the characteristic scale of the strong interactions. Around this scale and beyond it is necessary to use non-perturbative methods, such as the well established approach of lattice field theory which will be the topic of the next section.

2.2 Lattice QCD

The lattice formulation of quantum field theory contains three key pieces, the first of which is the use of the functional integral quantisation method, which essentially replaces the operators of the canonical quantisation method with functionals, which can be formally manipulated with known functional integral methods. The second step is to then perform a Wick rotation whereby the temporal component of spacetime is analytically rotated into imaginary time and thus resulting in a functional integral with an explicitly real phase, resulting in a clear physical interpretation and the applicability of numerical methods thanks to the formal analogy between Euclidean functional integrals and statistical mechanics systems[13]. The final piece is the use of a 4-dimensional lattice as a regulator, which is defined without the use of and is thus applicable beyond the scope of perturbation theory, allowing for the investigation of non-perturbative physics. The formal introduction of these pieces is rather involved and thus here the key results will simply be stated, which are taken from the first chapter of both [30, 31], each of which go into extensive detail.

[13]The resultant Euclidean symmetry further simplifies the formal manipulations for scalar field theory, as the fields, which are the fundamental degrees of freedom within the functional integral, now behave as classical fields in that they commute with one another. For QCD the situation is more complex and must respect the correct fermion statistics, as will be discussed shortly.

The lattice, Λ, is taken for the sake of simplicity to be a 4D hyper-cube;

$$\Lambda = \{n = (n_0, n_1, n_2, n_3) | n_0 = 0, 1, \ldots, N_T - 1; n_1, n_2, n_3 = 0, 1, \ldots, N - 1\}, \tag{2.22}$$

whereby the lattice sites are separated by the lattice spacing a. The fermionic degrees of freedom, $\psi(x)$ and $\bar{\psi}(x)$, live on the lattice sites, where the spacetime coordinate is related to the lattice via $x = an$, where $n \in \Lambda$. The gauge degrees of freedom, U, live on the links that connect the lattice spacing's on a nearest neighbour basis. The discretisation onto a lattice replaces the infinite dimensional functional integral with a very high-dimensional ordinary integral.

The continuation into imaginary time involves replacing the typical Minkowski time coordinate t_M with its Euclidean counterpart t_E, which are related via;

$$t_M = -it_E : t_E > 0, \tag{2.23}$$

with the consequence that the appropriate spacetime metric is that of Euclidean spacetime, which happens to be the Kronecker delta $\delta_{\mu\nu}$. Moreover the covariant and contravariant four-vectors are equivalent, $x^E_\mu = x^{E\mu}$. Henceforth four-vectors are to be explicitly understood as Euclidean unless stated otherwise, and thus the subscript will be dropped, $t_E \equiv t$.

The Euclidean correlation function must however still be related to a well defined Hilbert space and thus to the Hamiltonian formalism. Moreover it is crucial that the lattice discretisation of the system is such that the Euclidean correlators $\langle O_2(t)O_1(0)\rangle$ satisfy the expression, given here for the simple case of a scalar field theory[14];

$$\begin{aligned} \lim_{T\to\infty}\left(\left\langle O_2(t)O_1(0)\right\rangle\right) &= \lim_{T\to\infty}\left(\frac{1}{Z_T}\,\mathrm{tr}\left\{e^{-(T-t)\hat{H}}\hat{O}_2 e^{-t\hat{H}}\hat{O}_1\right\}\right) \\ &= \sum_n \langle 0|\hat{O}_2|n\rangle\langle n|\hat{O}_1|0\rangle e^{-tE_n}, \end{aligned} \tag{2.24}$$

which ensures that physical matrix elements and energy levels can be extracted. Additionally, in order that the above expression is satisfied and that a quantum mechanical Hilbert space exists, the Euclidean correlators computed with the functional integral must satisfy the Osterwalder-Schrader reconstruction. This is beyond the scope of this thesis and the interested reader is directed to the aforementioned references, however the point is that the lattice formulation must ultimately connect with the physical quantum mechanical Hilbert space and thus produce physical results.

The Euclidean correlation function, or Euclidean correlator, is expressed in terms of a functional integral via;

$$\left\langle O_2(t)O_1(0)\right\rangle_T = \frac{1}{Z_T}\int \mathcal{D}[\phi]e^{-S_E[\phi]}O_2[\phi(x_2,t)]O_1[\phi(x_1,0)], \tag{2.25}$$

which is an integral over all field configurations and can be numerically evaluated, the details of which will be explored in section 2.2.4. The normalisation factor, which will later be identified as

[14] See pg.1 of [30]. Note that $n = 0$ is included in the sum for those states that have vacuum quantum numbers.

the partition function, can also be expressed as a functional integral;

$$Z_T = \mathrm{tr}\Big\{e^{-T\hat{H}}\Big\} = \int \mathcal{D}[\phi] e^{-S_E[\phi]} : \mathcal{D}[\phi] = \prod_{x\in\Lambda} d\phi(x), \tag{2.26}$$

with the Boltzmann weight, $e^{-S_E[\phi]}$, depending on the Euclidean action functional $S_E[\phi]$. The equivalent expression for QCD is given by;

$$\Big\langle O_2(t)O_1(0)\Big\rangle_T = \frac{1}{Z_T}\int \mathcal{D}[\psi,\bar{\psi}]\mathcal{D}[U] e^{-S_F[\psi,\bar{\psi},U]-S_G[U]} O_2[\psi,\bar{\psi},U]O_1[\psi,\bar{\psi},U], \tag{2.27}$$

where the partition function is given by;

$$Z_T = \int \mathcal{D}[\psi,\bar{\psi}]\mathcal{D}[U] e^{-S_F[\psi,\bar{\psi},U]-S_G[U]}. \tag{2.28}$$

The functional integral measure for the fermion fields is given by a finite product of measures;

$$\mathcal{D}[\psi,\bar{\psi}] = \prod_{x\in\Lambda}\prod_{f,\alpha,i} d\psi^f_{\alpha,i}(x) d\bar{\psi}^f_{\alpha,i}(x), \tag{2.29}$$

with f being the flavour index, α the spinor index and i is the fundamental representation colour index. In order for the fermions to obey the required Fermi statistics, they are implemented in practice as anti-commuting numbers called Grassmann numbers. A discussion of the specific details of the properties of Grassmann numbers is not necessary for the present work, and the full details can be found in chapter 5 of [30], however there are a few key points worth mentioning. The fermionic degrees of freedom can be integrated out such that the remaining gauge part of the functional integral takes the form;

$$< . >_G = \frac{1}{Z}\int \mathcal{D}[U] e^{-S_G[U]} Z_F[U] O[U], \tag{2.30}$$

where the $O[U]$ term includes the fermionic part of the functional integral $< O >_F$, along with purely gluonic observables, and the whole functional integral may be expressed as $<< O >_F >_G$. The partition function $Z_F[U]$ is called the fermion determinant, which is the determinant of the Dirac operator, and the inverse of the Dirac operator is called the propagator. The key point is that the fermionic degrees of freedom can be integrated out and thus all relevant information can be expressed in terms of gauge fields and the Dirac operator, which can be shown via Wicks theorem. These details are not pertinent for the current work and it should simply be understood that henceforth the only key details will be the gauge fields U, the fermion action $S_F[\psi,\bar{\psi},U]$, the gauge action $S_G[U]$, and the measure over gauge fields $\mathcal{D}[U]$.

The functional integral measure for the gauge field is given by;

$$\mathcal{D}[U] = \prod_{x\in\Lambda}\prod_{\mu=0}^{3} dU_\mu(x), \tag{2.31}$$

which along with the lattice version of the fermion action $S_F[\psi, \bar{\psi}, U]$ and the gauge action $S_G[U]$ will be discussed in the following sections.

The analogy to statistical mechanics can be seen by noticing that the form of the expectation value in a statistical mechanics system is determined by the sum of possible values, weighted by the probability of finding the system in the associated configuration. Moreover, for a spin system where the degrees of freedom are the spin variables s, which is in a heat bath of temperature T and where the system is closed, i.e. in the canonical ensemble, the expectation value of some observable O is given by;

$$< O >= \frac{1}{Z} \sum_s e^{-\beta H[s]} O[s], \tag{2.32}$$

where the probability of finding the system in a given configuration is;

$$P[s] = \frac{1}{Z} e^{-\beta H[s]} : Z = \sum_s e^{-\beta H[s]}. \tag{2.33}$$

Here the term $\beta = 1/k_B T$ is the inverse temperature, where the Boltzmann constant is often set to one, $k_B = 1$. The Boltzmann factor $e^{-\beta H[s]}$ plays the role of a weight factor, much as the factor $e^{-S_E[\phi]}$ does within the Euclidean path integral eq. (2.25). As such, the identification of the normalisation factor within the functional integral, Z, as a partition function becomes justified. Further details of finite temperature field theory and QCD will be discussed in a later section, once the groundwork of defining the lattice actions and some other subtleties have been laid out.

The sum total of the above is that the continuous Minkowski spacetime is substituted with a discrete Euclidean lattice, with classical field variables taking the role of the fundamental degrees of freedom. The Euclidean action for the fermionic and gauge degrees of freedom are discretised onto the lattice in such a manner as to regain their continuum Euclidean counterparts in the naive continuum limit $a \to 0$. The Euclidean correlator is composed of functionals and can thus be evaluated by integrating over all lattice configurations, with each being weighted by an appropriate Boltzmann factor.

In the next section the details of the gauge fields U, the gauge action $S_G[U]$, and the integration measure $\mathcal{D}[U]$ will be discussed. Subsequently the details of the fermion action $S_F[\psi, \bar{\psi}, U]$ will be discussed, followed by the specific details of the FASTSUM lattice setup and the numerical methods for determining the functional integrals.

2.2.1 Lattice Gauge Theory

In order to understand gauge theory on the lattice it is instructive to first consider continuum gauge theory from a geometrical perspective. Generally speaking, the product of two spaces can be thought of in terms of taking some base space, and at each point within this base space, embedding an independent copy of the second space, which is referred to as the fibre space [32]. Each embedded copy of the fibre space is called a fibre and collectively the fibres are known as a fibre bundle, which in the case of having a Lie group as the fibre space is given the name principal fibre bundle. In

the case of QCD, the base space is spacetime itself, whereas the fibre space is the fundamental representation[15] of $SU(3)$.

The key point is that the matter field $\psi(x)$ has a value at each point in spacetime, and thus it has a value within each fibre, which happens to be vector-valued. However when taking the derivative, the value of the field is necessarily compared at different points in spacetime, i.e. on different fibres. Local gauge invariance permits the arbitrary assignment of the coordinates within each fibre, and thus there must exist some means by which to translate the coordinates of the field at some point, $\psi(x+\delta x)$, to the coordinates at some other point $\psi(x)$, so that the values of the field at different points can be meaningfully compared. The general name for the object of interest is the gauge connection, and this role is performed by the Lie algebra valued gauge field $A_\mu(x)$ once a set of coordinates has been specified for each fibre. In order to parallel transport the field $\psi(x+\delta x)$ to the infinitesimally close point x, it must be multiplied by $(1+iA^a_\mu(x)\delta x^\mu T^a)$. This is then compounded in order to perform parallel transport over larger distances, where the total transport operator for taking a field from x_0 to x_n via infinitesimal steps is denoted as $U(x_0,x_n)$ and defined by;

$$U(x_0,x_n)\psi(x_n) = (1+iA^a_\mu(x_0)(x_1-x_0)^\mu T^a)\dots(1+iA^a_\mu(x_{n-1})(x_n-x_{n-1})^\mu T^a)\psi(x_n). \tag{2.34}$$

The result depends on the path taken, C, and once specified the product is known as the Wilson line which can be written as a path ordered exponential;

$$U(x_0,x_n,C) = Pe^{(\int_C iA^a_\mu(x)dx^\mu T^a)}. \tag{2.35}$$

The path may be taken to form some closed loop, and when this Wilson loop exhibits the characteristic that;

$$U(x_0,x_n,C) \neq 1, \tag{2.36}$$

then the gauge connection possesses curvature, which is a fancy way to say that the field strength tensor is non-zero. The reason why all of this is important is that it provides insight as to how a gauge theory on the lattice ought to be constructed. The gauge connection is the general term for that object which connects the fibres together into a fibre bundle and in doing so allows the field to be parallel transported so that derivatives, and in general all interesting operators, can be meaningfully computed. The coordinates within each fibre can be independently set, and once this is done the role of the connection is performed by the gauge field $A_\mu \in \mathfrak{SU}(3)$. The coordinates for the fibres can be changed by a local gauge transformation $\Lambda(x)$, which will then also result in a change to the gauge field A_μ such that it still connects the fibres together in the appropriate manner. And therein lies the essence of the gauge field, it is that object which connects the fibres together into the fibre bundle and keeps track of any coordinate transformations through local gauge transformations.

[15]Strictly speaking it could be any representation of $SU(3)$, however these details are not crucial here and thus liberties shall be taken for the sake of simplicity.

The question now is how to replicate this utility on the lattice. Moreover the discretisation replaces the derivative, which involves the gauge field A_μ, with a finite difference, which is not necessarily gauge invariant. Furthermore the theory ought to have exact gauge invariance, otherwise non-gauge invariant operators will contribute to observables, which are remarkably difficult to deal with and should be avoided at all costs. However, noting the above consideration of continuum gauge theory, it is clear that whatever the solution is, it must involve some prescription for taking the field ψ and parallel transporting it in some manner which respects gauge invariance. The solution turns out to be that it is in-fact the Lie group elements $U_\mu(x) \in SU(3)$, which perform the role of the gauge connection. The Lie group elements thus take on the role of the lattice gauge field (which from here on in will simply be called the gauge field), and can be related to the familiar path ordered exponential via;

$$U_\mu^{ij}(x) = Pe^{\int_x^{x+a\hat{\mu}} A_\mu^a(x+l)T_{ij}^a dl} \simeq e^{iaT_{ij}^a A_\mu^a(x)}, \tag{2.37}$$

where the second equality highlights the relation of the Lie algebra and Lie group elements through the exponential map. The gauge field lives on the link between nearest neighbouring lattice points, and more specifically it lives at the midpoint $x + a\hat{\mu}/2$. Strictly speaking the gauge field contains a colour index i which is associated with the fundamental representation at site x, and a colour index j which is associated with the anti-fundamental representation at site $x + a\hat{\mu}$. The lattice gauge field is thus often referred to as the gauge link. Any gauge invariant operator will have no free colour indices and must thus be formed by either a Wilson loop or a Wilson line capped at each end by the appropriate fermion fields. The colour indices will be dropped from here on in unless explicitly required.

The prescription for transporting the field $\psi(x + a\hat{\mu})$ to the point x is given as;

$$U(x, x + a\hat{\mu})\psi(x + a\hat{\mu}) = U_\mu(x)\psi(x + a\hat{\mu}), \tag{2.38}$$

whereas to take the field $\psi(x)$ to the site $x + a\hat{\mu}$, the expression is;

$$U(x + a\hat{\mu}, x)\psi(x) = U_\mu^\dagger(x)\psi(x). \tag{2.39}$$

Moreover the formation of a Wilson line is still path dependent, where in order to transport the field $\psi(x + 2a\hat{\mu} + a\hat{\nu})$ to point x through path C, via sites $x + a\hat{\mu} + a\hat{\nu}$ and $x + a\hat{\mu}$, the expression is given by;

$$U_C\psi(x + 2a\hat{\mu} + a\hat{\nu}) = U_\mu(x)U_\nu(x + a\hat{\mu})U_\mu(x + a\hat{\mu} + a\hat{\nu})\psi(x + 2a\hat{\mu} + a\hat{\nu}). \tag{2.40}$$

In order to respect local gauge invariance the gauge field must itself transform according to;

$$U_\mu(x) \to \Lambda(x)U_\mu(x)\Lambda^{-1}(x + a\hat{\mu}). \tag{2.41}$$

In order to compute the correlation functions of interest, the gauge group measure must be defined.

It is already clear that the measure from the continuum must be replaced by the finite product of lattice gauge link measures;

$$DA_\mu \to \prod_{x\mu} dU_\mu(x), \tag{2.42}$$

but the question remains as to what $dU_\mu(x)$ itself actually means, albeit it is clear that it must be gauge invariant. There are certain requirements for the integration measure over the group manifold G, including left and right invariance;

$$\int dU f(U) = \int dU f(U\Lambda) = \int dU f(\Lambda U) \forall f(U) : U, \Lambda \in G, \tag{2.43}$$

linearity;

$$\int dU(\alpha f(U) + \beta g(U)) = \alpha \int dU f(U) + \beta \int dU g(U), \tag{2.44}$$

and the normalisation condition;

$$\int dU 1 = 1. \tag{2.45}$$

The unique measure that satisfies these requirements is called the Haar measure, which encompasses an area of the group manifold which is not changed in its magnitude by gauge transformations. It should be noted that the normalisation condition is specific to the lattice, as the dynamical degrees of freedom are the Lie group elements rather than the Lie algebra elements, and thus exist on a compact space. Moreover the approach to gauge fixing on the lattice is rather humorously to simply not do it at all, instead opting to integrate over all gauge field configurations, which is itself only possible due to working with the compact space of the Lie group.

The requirement of left and right invariance guarantees the required gauge invariance eq. (2.41). However this requires that;

$$\int dUU = \int dU\Lambda_1 U \Lambda_2^{-1} : \forall \Lambda_1, \Lambda_2 \in G, \tag{2.46}$$

where the only solution is then;

$$\int dUU = 0, \tag{2.47}$$

with the only non-vanishing result occurring when integrating over gauge invariant objects. Consequently the expectation value of any non-gauge invariant observable will vanish, $< \mathcal{O} >= 0$, which is known as Elitzur's theorem [34].

The only remaining task, given the aforementioned definitions of the gauge field and the gauge measure, is to specify the lattice discretisation of the gauge action. The gauge action can be built from the simplest gauge invariant Wilson loops, i.e. plaquettes, which are constructed from the gauge link such that;

$$U_{\mu\nu}(x) = U_\mu(x)U_\nu(x + a\hat{\mu})U^\dagger_\mu(x + a\hat{\nu})U^\dagger_\nu(x). \tag{2.48}$$

The Wilson gauge action is then given by;

$$S^W = \frac{\beta}{N_c}\sum_x\sum_{\mu<\nu}\mathrm{Re}(\mathrm{tr}\{1 - U_{\mu\nu}(x)\}) = \frac{\beta}{2N_c}\sum_x\sum_{\mu,\nu=0}^{3}\mathrm{Re}(\mathrm{tr}\{1 - U_{\mu\nu}(x)\}), \tag{2.49}$$

which can be related to the continuum gauge action, and will be discussed in further explicit detail in section 2.2.3. In this context and from now on, unless stated otherwise, β is the inverse (bare) gauge coupling $\beta = 2N_c/g^2$.

The naive continuum limit involves ensuring that the lattice action is equal to the continuum action in the limit $a \to 0$. This is a useful tool in the construction of lattice field theory, however the true continuum limit also involves evaluating the path integral, and thus within numerical computations the couplings are driven to their critical values, where the statistical mechanics equivalent of the lattice theory undergoes a second order phase transition. In pure gauge theory the lattice spacing decreases with the coupling g and also with increasing β. Thus the true continuum limit where $a \to 0$ is obtained when $\beta \to \infty$.

However as the lattice spacing is driven to zero, so too is the physical volume encapsulated within the lattice, resulting in finite volume effects. This is avoided by increasing the number of lattice spacings, and ideally taking the thermodynamic limit, $N_S \to \infty$ and $N_T \to \infty$, before taking the continuum limit. This is clearly not numerically possible and thus instead the observables in question must be computed at several values of β, with an extrapolation to $a \to 0$ then being carefully performed. This is done in such a way where the physical volume of the lattice, $L = aN_S$ and $T = aN_T$ are fixed for varying lattice spacings.

2.2.2 Lattice Fermions

Naive Fermions

Given the form of the quark Lagrangian density for the continuum, eq. (2.5), the task of discretising the fermion action involves writing a lattice version of $\bar{\psi}(x)\gamma^\mu D_\mu\psi(x)$. An initial guess may take the form;

$$\bar{\psi}(x)\gamma^\mu D_\mu\psi(x) \to a^4\sum_\mu \bar{\psi}(x)\gamma^\mu\left(\frac{U_\mu(x)\psi(x + a\hat{\mu}) - \psi(x)}{a}\right), \tag{2.50}$$

where γ^μ are the euclidean gamma matrices, however this does not respect reflection-positivity, and thus does not correspond to a unitary Minkowski theory which in turn means that the observables

are not real [33]. The derivative must take a symmetric form such as;

$$\bar{\psi}(x)\gamma^{\mu}D_{\mu}\psi(x) \rightarrow a^{4}\sum_{\mu}\bar{\psi}(x)\gamma^{\mu}\left(\frac{U_{\mu}(x)\psi(x+a\hat{\mu})-U_{\mu}^{\dagger}(x-a\hat{\mu})\psi(x-a\hat{\mu})}{2a}\right), \tag{2.51}$$

which is referred to as the naive lattice fermion action. However there exists a fundamental issue with this action, in that it necessarily describes 16 fermions. Moreover it is not possible within the computation to distinguish and then isolate the actual physical fermion seen in the continuum theory, from those fermions which are the 15 uninvited doublers. Mathematically the physical fermion corresponds to a pole in momentum space at;

$$p = (0, 0, 0, 0), \tag{2.52}$$

whereas the 15 unwanted doublers relate to poles where at least one of the coordinates is at π/a;

$$p = (\pi/a, 0, 0, 0), (0, \pi/a, 0, 0), \ldots, (\pi/a, \pi/a, \pi/a, \pi/a). \tag{2.53}$$

The derivation of these results is not relevant for this overview, however the details can be found in section 5.2 of [30]. The natural question is whether a suitable alternative expression can be written down which does not contain these doublers, thus allowing for the lattice to compute physical quantities. The Nielsen-Ninomiya No-Go theorem states that it is not possible for a lattice fermion action to simultaneously respect the following four properties [35];

1. Locality,
2. Translational invariance,
3. No fermion doublers,
4. Respects chiral symmetry.

Hence, in order to remove the fermion doublers and maintain a real action it is required to sacrifice either locality, translational invariance or chiral symmetry.

Wilson Fermions

The present work utilises the approach put forward by Kenneth Wilson, who proposed to include an additional term which explicitly violates chiral symmetry, and removes the 15 doublers. This is known as the Wilson term[16] and is expressed as;

$$-a^{4}\sum_{x,\mu}\frac{1}{2a}\bar{\psi}(x)\left(U_{\mu}(x)\psi(x+a\hat{\mu})+U_{\mu}^{\dagger}(x-a\hat{\mu})\psi(x-a\hat{\mu})-2\psi(x)\right), \tag{2.54}$$

[16]The Wilson term is the discretisation of $-(a/2)\partial_{\mu}\partial_{\mu}$ [30].

which is often written in the literature in the form;

$$-a^4\sum_{x,\mu}\frac{1}{2a}\bar{\psi}(x)\Big(U_\mu(x)\psi(x+a\hat{\mu})+U_\mu^\dagger(x-a\hat{\mu})\psi(x-a\hat{\mu})\Big)+a^4\sum_x\bar{\psi}(x)\frac{4}{a}\psi(x). \tag{2.55}$$

The two expressions can be seen to be equal noting that within eq. (2.54) the $\psi(x)$ factors contain no explicit μ index, and thus accounting for the coefficients there are four such contributions in total.

The further inclusion of a mass term would take the form;

$$a^4\sum_x\bar{\psi}(x)m_0\psi(x), \tag{2.56}$$

where it should be noted that this term originated not from QCD but rather from the electroweak sector [36].

Moreover the inclusion of a generic boundary term takes the form ;

$$a^4\sum_x\bar{\psi}(x)D^B\psi(x), \tag{2.57}$$

where the Dirac operator for the boundary term is given by;

$$D^B\psi(x)=\Big((c_F-1)\delta_{x_0,1}+(c_F^{'}-1)\delta_{x_0,T-1}\Big)\psi(x). \tag{2.58}$$

Within this work periodic boundary conditions[17] are used, such that $c_F=c_F^{'}=1$, resulting in the boundary term vanishing and the lattice essentially having no boundaries.

The massive Wilson fermion action is then taken as the sum of the naive discretisation, the Wilson term and the mass term, and is given by;

$$\begin{aligned}S^W=&a^4\sum_{x,\mu}\frac{1}{2a}\bar{\psi}(x)\Big((\gamma_\mu-1)U_\mu(x)\psi(x+a\hat{\mu})-(\gamma_\mu+1)U_\mu^\dagger(x-a\hat{\mu})\psi(x-a\hat{\mu})+2\psi(x)\Big)\\&+a^4\sum_x\bar{\psi}(x)m_0\psi(x),\end{aligned} \tag{2.59}$$

[17] The fermion fields $\bar{\psi}(x)$ and $\psi(x)$ are periodic in the spatial directions and anti-periodic in the temporal direction. For a lattice defined in the range $0\leq x_\mu\leq N_{\mu-1}$, the spatial boundary terms are thus;

$$\psi(x)\mid_{x_j=N_j}=e^{i\theta_j}\psi(x)\mid_{x_j=0}\ :\ j=1,2,3,$$

where θ_j are real angles. The temporal boundary conditions are given by;

$$\psi(x)\mid_{x_0=N_0}=-\psi(x)\mid_{x_0=0}.$$

which can then be re-written in terms of the massless Wilson-Dirac operator $\hat{D}^W_\mu$;

$$S^W = a^4 \sum_{x,\mu} \frac{1}{a} \bar{\psi}(x) \hat{D}^W_\mu \psi(x) + a^4 \sum_x \bar{\psi}(x) m_0 \psi(x), \tag{2.60}$$

where the massless Wilson-Dirac operator is given by;

$$\hat{D}^W_\mu \psi(x) = \frac{1}{2}\Big((\gamma_\mu - 1) U_\mu(x) \psi(x + a\hat{\mu}) - (\gamma_\mu + 1) U^\dagger_\mu(x - a\hat{\mu}) \psi(x - a\hat{\mu}) + 2\psi(x) \Big). \tag{2.61}$$

The form of the action given in eq. (2.60) is such that the fermion fields are expressed as dimensionful quantities, whereas the Wilson-Dirac operator is given as a dimensionless quantity, specified by the notational convention that it is given a hat. All quantities which possess some dimension and are thus not simply pure numbers, can be expressed as a dimensionless number multiplied by some explicit dimension such as $\psi(x) = \hat{\psi}(x) a^{-3/2}$. Within the above action, the factor of a^{-1} was a consequence of the finite difference, which came about due to the lattice version of the covariant derivative acting on the field $\psi(x)$. The action is itself a pure number and thus both terms on the right hand side of eq. (2.60) must also be overall dimensionless. Dimensional analysis shows that the factor of a^{-1} is from the units of the Wilson-Dirac operator, hence why $\hat{D}^W_\mu$ has been denoted as its dimensionless form. In order for a quantity to be expressed in physical units, it must absorb its dimension, leaving no explicit trace of the units within the expressions where it appears. It is in this dimensionful form that many expressions are given within the literature, and thus it is prudent to restate the above in explicitly dimensionful form[18].

The massive Wilson fermion action is then written in purely dimensionful terms as;

$$S^W = a^4 \sum_{x,\mu} \bar{\psi}(x) D^W_\mu \psi(x) + a^4 \sum_x \bar{\psi}(x) m_0 \psi(x), \tag{2.62}$$

where the massless Wilson-Dirac operator is given in dimensionful terms, D^W_μ by;

$$D^W_\mu \psi(x) = \frac{1}{2a}\Big((\gamma_\mu - 1) U_\mu(x) \psi(x + a\hat{\mu}) - (\gamma_\mu + 1) U^\dagger_\mu(x - a\hat{\mu}) \psi(x - a\hat{\mu}) + 2\psi(x) \Big). \tag{2.63}$$

There are several points regarding Wilson fermions which should be mentioned at this point. The manner by which the Wilson term eliminates the fermion doublers is by giving the doublers a mass of the order of the cut-off, whilst the physical fermion which survives after taking the continuum limit remains massless[19]. It should be noted that the physical fermion remaining massless is to be taken solely in the context of QCD, where no explicit mass term of the form $\bar{\psi}(x) m \psi(x)$ is permitted due to the resultant lack of invariance under $SU(2)_L$ transformations. Moreover such a forbidden mass term containing only spin-1/2 fields must necessarily mix left and right handed components

[18] The dimensionality of the action will be explained in detail within section 2.2.3 when discussing the form of the action which is used within the present work.

[19] Further details can be found in [35], which highlights the subtlety that the Wilson term acts like a momentum-dependant mass term.

in order to respect Lorentz invariance, whereas only left handed fields transform non-trivially under $SU(2)_L$. The mass term within the above expressions which entered into the discussion in eq. (2.56), is of a different nature and has its origin within the electroweak sector and the Higgs mechanism. A discussion of this is presented within section 7.5 of [36]. The key point is that this mass term secretly contains a spin-0 doublet, and cannot be obtained from considerations of QCD. Moreover the above statements regarding the doublers obtaining a mass and the physical fermion remaining massless, have nothing whatsoever to do with the mass term, eq. (2.56), and should be thought of as being entirely separate.

The violation of chiral symmetry by the Wilson term introduces unwanted contributions in correlation functions, which enter at the level of dimension-5 operators [37]. This must then be corrected for by adding a suitable counter-term, which will be discussed in detail within section 2.2.3. Chiral symmetry is ultimately regained in the continuum limit by using correlation lengths and tuning to obtain the correct mass, which must be done for each individual lattice spacing used within the extrapolation. One such example would be tuning the ratio of the masses for the pion and rho particles M_π/M_ρ [33]. Furthermore when using Wilson fermions there are occasionally configurations that are generated which possess a negative determinant. This can, depending on the lattice spacing, increase the numerical expense of performing simulations with Wilson fermions when the mass is small.

A review of alternative approaches to that of Wilson fermions is beyond the scope of the present work. However it is worth noting that there do exist other approaches to that of Wilson fermions for navigating past the No-Go theorem, such as that of Kogut and Susskind, called staggered fermions[20]. The idea behind staggered fermions is to start from the naive fermion action, eq. (2.51), and realise that it can be broken into 4 blocks. These 4 components are distributed in some manner over a 2^4 block of the lattice. The result is a theory with 4 Dirac fermions, which contains an exact $U(1) \times U(1)$ chiral symmetry[21]. Thus there still remain doublers, however now there are only 4 fermions, and some level of chiral symmetry is preserved. However the resultant 4 fermions are coupled to one another and it is not obvious whether the approach is mathematically sound [33], and as such staggered fermions are an interesting and active area of research. Furthermore it is possible to remove the doublers completely without using Wilson fermions, however such approaches are often not favourable, such as with SLAC fermions, where chiral symmetry is maintained but at the expense of locality [37].

Chiral Symmetry on the Lattice

Wilson fermions are perfectly fine for doing studies of QCD, however they are inappropriate for the standard model as a whole, as they explicitly break the chiral symmetry which is required for the electroweak interactions. Furthermore the requirement for tuning of mass ratios in order to obtain the correct continuum limit is often criticised as an unnatural fine tuning [35].

[20] An overview is given in chapter 10 of [30].
[21] A review of chiral symmetry is given in Appendix A.

Whilst a full summary of chiral fermions on the lattice is far beyond the scope of this work, for the sake of completeness it is worth making several points. Recapitulating, the lattice discretisation of the covariant derivative is given by eq. (2.51), which was necessarily symmetric in order for the resultant observables to be real. This naive fermion term creates fermion doublers, with no way to discern the physical fermion from the nonphysical doublers, and thus real physics cannot be studied[22]. The No-Go theorem states that in order to remove these obstructive doublers, it is necessary to sacrifice either the locality, translational invariance or the chiral symmetry. Sacrificing locality within QCD is considered to be implausible, due to the complexities of working with non-local QFT. Translational invariance must be maintained in order to correctly regain full Lorentz symmetry in the continuum limit. Thus the only viable option would seemingly be to do violence to chiral symmetry. In order to navigate the above inconveniences it is necessary to do something more radical.

Building on the previous work of Callan and Harvey, David Kaplan has shown that massless four-dimensional lattice fermions are obtained without fine-tuning, by being localised on a domain wall embedded within a five-dimensional space-time [37, 38]. Moreover fermions of opposite handedness can be localised on opposite walls within this fifth dimension, often called the domain wall and anti-wall. If the separation between this wall and anti-wall, L, is sufficiently large, then the left and right handed components of the Dirac fermion cannot mix. Chiral symmetry breaking terms are suppressed by $e^{-L/a}$, and thus a Wilson term in the five-dimensional lattice theory removes the doublers without breaking the chiral symmetry. These domain wall fermions thus possess a chiral symmetry, which is approximate for a finite separation L, and becomes exact in the infinite wall-anti-wall separation limit, $L \to \infty$.

A similar method was developed by Narayanan and Neuberger, whereby an infinite number of quark flavours are permitted, resulting in what are known as overlap fermion . This is intimately related to domain wall fermions, in that the infinite flavour space forms a fifth-dimension, and the overlap fermions possess an exact chiral symmetry. Domain wall fermions and overlap fermions are equivalent in the limit of wall-anti-wall separation, $L \to \infty$.

In both of the above instances, the approach to seemingly bypassing the No-Go theorem involved invoking the use of a higher dimension. However it must be stressed that both the domain wall fermions and overlap fermions do in fact obey the No-Go theorem, but with one crucial caveat. The requirement that chiral symmetry be respected on the lattice can be expressed as;

$$\{\gamma^5, D(k)\} = 0, \tag{2.64}$$

where here $D(k)$ is the Dirac operator after being Fourier transformed into momentum space. Ginsparg and Wilson showed that a general requirement for a lattice action to possess good chiral properties is ;

$$\{\gamma^5, D(k)\} = aD\gamma^5 D. \tag{2.65}$$

When the Ginsparg-Wilson relation was first written down, it did not appear to be possible to

[22]The case of staggered fermions was an exception with only 4 fermions of the original 16 surviving.

explicitly construct lattice actions that satisfy it. Noting once more however that the domain wall fermions and overlap fermions are equivalent for infinite wall-anti-wall separation, it has been shown by Neuberger that overlap fermions satisfy the Ginsparg-Wilson relation exactly. Thus the manner by which both domain wall fermions and overlap fermions appear to navigate past the No-Go theorem, is by satisfying an alternate form of chiral symmetry, eq. (2.65), which is equal to the expected definition, eq. (2.64), in the naive continuum limit $a \to 0$.

This alternate form of chiral symmetry is such that the extent to which a fermion is rotated depends on its momentum, and thus the symmetry does not act on all of the lattice points in the same way. Hence, whilst the No-Go theorem is still being obeyed, a concession on the form of chiral symmetry which is being respected, has allowed for a description of lattice fermions with all of the desired properties. This is still an area of active research, and these methods are often passed over in favour of Wilson fermions when studying QCD, simply due to the increased numerical expense associated with both domain wall and overlap fermions.

Finally, it is worth briefly mentioning that Hasenfratz and Niedermayer have investigated lattice actions which are completely free of cut-off effects, called perfect actions, the matter content of which is often referred to as perfect fermions . This approach uses non-perturbative renormalisation group blocking transformations on the lattice, whereby the fixed points of these transformations correspond to the perfect action. This is often criticised however as potentially being another form of unnatural fine-tuning.

2.2.3 FASTSUM Lattice Setup

In non-zero temperature studies it is advantageous to have a fine resolution within the temporal direction in order that the temperature can be adjusted in small steps. Unfortunately in the case of the isotropic lattice, this small lattice spacing a would require many lattice points in order to contain a sufficient volume so as to prevent erroneous small volume effects, which then results in a very large computational demand. In order to keep the computational requirement within realistic limits whilst achieving the desired resolution in temperature, the size of the lattice spacing in the spatial direction a_s and that in the temporal direction a_t are given different values. The ratio of the spatial to temporal lattice spacing's a_s/a_t is known as the lattice anisotropy. Due to renormalisation the bare value of the anisotropy which enters into the action is different than that which the particle content of the theory experiences. Moreover the gauge particles and fermionic matter experience different levels of renormalisation such that they must be individually tuned so that the bare gauge anisotropy γ_g and the bare fermion anisotropy γ_f both get renormalised to their intended values. The renormalised gauge anisotropy $\tilde{\gamma}_g$ and the renormalised fermion anisotropy $\tilde{\gamma}_f$ must be tuned to be equal to one another, such that the gauge and fermion sectors ultimately experience the same level of anisotropy. Once this tuning has been complete, which is closely related to the subject of chapter 3, there is thus only one renormalised anisotropy $\tilde{\gamma}_g = \tilde{\gamma}_f = \xi = a_s/a_t$, where here a_s and a_t take the values that are actually seen by the fields. However, when examining the manner in

which the anisotropy is applied to the lattice action it will be useful to keep explicit the factors of anisotropy for the gauge and fermion sectors, even when the renormalised value is being referenced.

As was discussed earlier at the end of section 2.2.1, when taking the continuum limit it is not feasible to first take the thermodynamic limit, and thus there remain explicit factors of a within the action and within the computed observables which must themselves be extrapolated to their continuum value at $a \to 0$. The computational requirement for performing this extrapolation precisely, depends on the degree to which the factors of a appear within the action and the operators. In order to reduce this computational expense and hasten the approach to the continuum limit, much effort is taken to perform so called improvement, whereby the leading order terms in a are cancelled by the inclusion of additional well chosen counter-terms.

There exist many approaches to performing improvement, several of which are reviewed to varying degrees within [39], whereby it is outlined that perturbative improvement, which is used within this work, consists of three steps. The first step is tree-level (classical) improvement whereby unwanted terms which contribute at the classical level are cancelled. The second step is tadpole improvement whereby those unwanted contributions which result from tadpole diagrams are cancelled out by the re-weighting of the gauge links. The third step is radiative corrections, which are not used within the present work and will thus not be discussed further. Any one of these steps can be independently applied, with the degree to which each step is significant being dependent on the details of the theory. These steps will be further elucidated below for both the gauge and fermion actions, starting with the familiar form of these actions which were presented in earlier sections.

The anisotropic version of eq. (2.62) from section 2.2.2 is given by;

$$S^W = a_s^3 a_t \sum_x \left(\bar{\psi}(x)\nu_t D_0^W \psi(x) + \sum_{i=1}^{3} \bar{\psi}(x)\nu_s D_i^W \psi(x) \right) + a_s^3 a_t \sum_x \bar{\psi}(x) m_0 \psi(x), \tag{2.66}$$

where the components of the massless Wilson-Dirac operator are given by;

$$D_0^W \psi(x) = \frac{1}{2a_t} \Big((\gamma_0 - 1) U_0(x) \psi(x + a\hat{0}) - (\gamma_0 + 1) U_0^\dagger(x - a\hat{0}) \psi(x - a\hat{0}) + 2\psi(x) \Big), \tag{2.67}$$

$$D_i^W \psi(x) = \frac{1}{2a_s} \Big((\gamma_i - 1) U_i(x) \psi(x + a\hat{i}) - (\gamma_i + 1) U_i^\dagger(x - a\hat{i}) \psi(x - a\hat{i}) + 2\psi(x) \Big). \tag{2.68}$$

The ν_t and ν_s factors are the bare velocity of light of the quarks in the temporal and spatial direction, and must be tuned such that special relativity is respected on the lattice, whence $\tilde{\gamma}_g = \tilde{\gamma}_f$ [6]. Either one of these factors is redundant, the choice of which results in either ν_t-tuning whereby $\nu_s = 1$ and ν_t is tuned, or ν_s-tuning where $\nu_t = 1$ and ν_s is tuned [4]. This work uses ν_s-tuning and thus $\nu_t = 1$ henceforth, where the tuning is performed using the parameterisation $\nu_s = \gamma_g/\gamma_f$ [2].

The tree-level $\mathcal{O}(a)$-improvement is determined in chapter 9 of [30], which results in the addition of an extra term to eq. (2.66), of the form;

$$+ C^{SW} a^5 \sum_x \sum_{\mu<\nu} \bar{\psi}(x) \frac{1}{2} \sigma_{\mu\nu} F_{\mu\nu}(x) \psi(x) \; : \; F_{\mu\nu}(x) = \frac{-i}{8a^2}(Q_{\mu\nu}(x) - Q_{\nu\mu}(x)) \; ; \; \sigma_{\mu\nu} = \frac{1}{2i}[\gamma_\mu, \gamma_\nu], \quad (2.69)$$

$$\begin{aligned} Q_{\mu\nu}(x) =& U_\mu(x) U_\nu(x + a\hat{\mu}) U_\mu^\dagger(x + a\hat{\nu}) U_\nu^\dagger(x) \\ &+ U_\nu(x) U_\mu^\dagger(x - a\hat{\mu} + a\hat{\nu}) U_\nu^\dagger(x - a\hat{\mu}) U_\mu(x - a\hat{\mu}) \\ &+ U_\mu^\dagger(x - a\hat{\mu}) U_\nu^\dagger(x - a\hat{\mu} - a\hat{\nu}) U_\mu(x - a\hat{\mu} - a\hat{\nu}) U_\nu(x - a\hat{\nu}) \\ &+ U_\nu^\dagger(x - a\hat{\nu}) U_\mu(x - a\hat{\nu}) U_\nu(x + a\hat{\mu} - a\hat{\nu}) U_\mu^\dagger(x), \end{aligned} \quad (2.70)$$

where the symmetric field strength tensor[23] is shown in fig. 2.5. In this work an alternate expression is used, which in anisotropic form is given by;

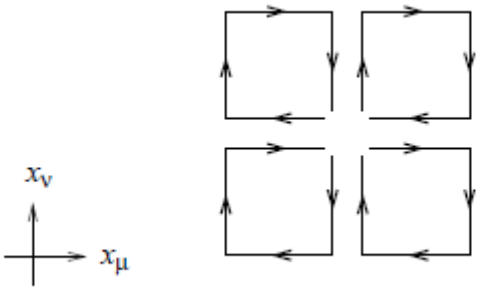

Fig. 2.5: Symmetric lattice field strength tensor $F_{\mu\nu}(x)$. Figure taken from [40].

$$\frac{+i a_s^4 a_t}{4} \sum_x \bar{\psi}(x) \left(2C_t^{SW} \sum_{i=1}^{3} \sigma_{0i} F_{0i}(x) + C_s^{SW} \sum_{i,j=1}^{3} \sigma_{ij} F_{ij}(x) \right) \psi(x), \quad (2.71)$$

where the various terms are explained below[24] and where the field strength tensor and Dirac-sigma matrices are given by;

$$F_{\mu\nu}(x) = \frac{1}{8a^2}(Q_{\mu\nu}(x) - Q_{\nu\mu}(x)) \; ; \; \sigma_{\mu\nu} = \frac{i}{2}[\gamma_\mu, \gamma_\nu]. \quad (2.72)$$

There are several differences between the two expressions although they are ultimately equivalent. The first of which is that the range of summation has been rewritten from $\mu < \nu$ to $\mu, \nu = 1 \rightarrow 3$, resulting in a relative double counting of each contribution[25] such that an additional factor of $1/2$ is required to cancel the extra terms, which is written out front for later comparison with the literature. The expression for the temporal sum is such that $\sigma_{i0} F_{i0}$ is never counted and thus the additional $1/2$ is not required, and is thus cancelled by the factor of 2. Moreover the two expressions contain

[23] This may be written more generally using U^{-1} rather than $U^\dagger$ in order to additionally be valid for non-unitary matrices. Here the notation from [30] with the hermitian conjugate will be used, for the sake of consistency.

[24] Note that the form given within eq. (2.69) is shown in order to provide the reader with a derivation from the literature, whereas the equivalent form stated subsequently is used within the literature relevant for this work and will not be derived separately.

[25] Note that $\sigma_{\mu\nu} F_{\mu\nu} = \sigma_{\nu\mu} F_{\nu\mu}$ due to symmetry.

different factors of i, however they are both overall explicitly real and contain a net negative sign.

The next step is to incorporate the corrections for the tadpole diagrams, which take the form of re-weighting the gauge links such that;

$$U_0(x) \to \frac{U_0(x)}{u_t},\ U_i(x) \to \frac{U_i(x)}{u_s} \tag{2.73}$$

where the tadpole factors are distinct for spatial and temporal gauge links, and only one of these needs to be independently determined, the choice of which is arbitrary. It is worth noting that the factors are the same for all spatial links and separately for all temporal links, and that any expressions containing n gauge links will thus contain n tadpole factors, distributed between spatial and temporal factors appropriately. In this work the temporal tadpole factor is held fixed and the spatial factor is determined such that;

$$u_t = 1,\ u_s = \left\langle \frac{1}{3}\mathrm{Re}(\mathrm{tr}\{U_{ss'}\}) \right\rangle^{\frac{1}{4}}, \tag{2.74}$$

where $U_{ss'}$ is the spatial platquette. The clover coefficients C^{SW} within eq. (2.71) have been estimated in [4], and at tree-level are given by;

$$C_t^{SW} = \frac{1}{2}\left(\nu_s + \frac{1}{\xi}\right)\ ;\ C_s^{SW} = \nu_s\ :\ \nu_s = \frac{\gamma_g}{\gamma_f}, \tag{2.75}$$

whereas the expressions for tree-level plus tadpole improvement are given by;

$$C_t^{SW} = \frac{1}{2}\left(\nu_s + \frac{1}{\xi}\right)\frac{1}{\tilde{u}_t\tilde{u}_s^2}\ ;\ C_s^{SW} = \frac{\nu_s}{\tilde{u}_s^3}\ :\ \nu_s = \frac{\gamma_g}{\gamma_f}, \tag{2.76}$$

where the renormalised anisotropy has been written in its tuned form ξ, as it's origin being from the bare gauge or the bare fermion anisotropy doesn't factor into the subtleties of any of the following expressions[26]. The notational convention $\tilde{u}$ is used to specify that the gauge links in question have first been adjusted using stout smearing[27], which has been shown to reduce the scaling effects and hence computational expense when taking the continuum limit [2]. The details of how this smearing of the gauge links is performed is beyond the scope of this work, but can be found within[28] [41].

The final $\mathcal{O}(a)$-improved fermion action S^F is then given as;

$$S^F = a_s^3 a_t \sum_x \bar{\psi}(x) D^F \psi(x), \tag{2.77}$$

[26] In practice the renormalised anisotropy for the gauge and fermion sectors should be equivalent, and thus the bare anisotropies will be tuned such that they both provide the same target renormalised anisotropy, which is denoted as ξ.

[27] Note that whilst stout smearing is only being applied in the spatial directions, this same notation will be applied to the temporal tadpole factors for notational consistency within the fermion action, as $\tilde{u}_t = 1$ anyway.

[28] It should however be noted that a smearing coefficient of $\rho = 0.14$ was chosen, with $n_\rho = 2$ smearing steps, as per [2].

with the Dirac operator including the mass term and appropriate tadpole factors now being given by;

$$\begin{aligned} D^F\psi(x) = &\Bigg[m_0\psi(x) + \frac{1}{\tilde{u}_t}D_0^W\psi(x) + \frac{\nu_s}{\tilde{u}_s}\sum_{i=1}^{3}D_i^W\psi(x) \\ &+\frac{ia_s}{4}\left(\frac{2C_t^{SW}}{\tilde{u}_t}\sum_{i=1}^{3}\sigma_{0i}F_{0i}(x) + \frac{C_s^{SW}}{\tilde{u}_s}\sum_{i,j=1}^{3}\sigma_{ij}F_{ij}(x)\right)\psi(x)\Bigg]. \end{aligned} \tag{2.78}$$

It should be noted that looking at eq. (2.67) and eq. (2.68), which are often referred to as hopping terms, the single gauge link results in a single tadpole factor[29]. Moreover due to the definition of the tree-level tadpole clover coefficients, eq. (2.76), the clover term requires a single explicit tadpole factor in both the spatial and temporal components, given that four such factors are required overall due to the four gauge links within each term of the field strength tensor.

The above formulation of the Dirac operator D^F can now be stated in dimensionless terms using the substitutions [4];

$$\begin{aligned} \psi &= \hat{\psi}a_s^{-3/2}, \\ m_0 &= \hat{m}_0 a_t^{-1}, \\ F_{\mu\nu}(x) &= \hat{F}_{\mu\nu}(x)a_{n1}^{-1}a_{n2}^{-1}, \\ D_\mu^W &= \hat{D}_\mu^W a_{n1}^{-1}, \end{aligned} \tag{2.79}$$

where the lattice spacing direction is determined by;

$$n_i = \begin{cases} t \text{ iff } i = 1 \text{ and } \mu = 0\ , \\ t \text{ iff } i = 2 \text{ and } \nu = 0\ , \\ s \text{ otherwise.} \end{cases} \tag{2.80}$$

Each term within the action S^F of eq. (2.77), can be expressed in terms of dimensionless quantities, from which the explicit factors of fermion anisotropy are made apparent. The mass term is the most straight forward and is given by;

$$\begin{aligned} a_s^3a_t\sum_x\bar{\psi}(x)m_0\psi(x) =& a_s^3a_t\sum_x\hat{\bar{\psi}}(x)a_s^{-3/2}\hat{m}_0a_t^{-1}\hat{\psi}(x)a_s^{-3/2} \\ =& \sum_x\hat{\bar{\psi}}(x)\hat{m}_0\hat{\psi}(x), \end{aligned} \tag{2.81}$$

where a complete cancellation of lattice spacing occurs and no anisotropy factors are present. The temporal hopping term is similarly straight forward with a substitution from eq. (2.79) yielding;

[29] In order to understand why the $2\psi(x)$ terms within D_0^W and D_i^W are also being acted on by the tadpole factors despite not containing a factor from a gauge link, it must be remembered from eq. (2.54) that the lone factors of $\psi(x)$ originate from the Wilson fermion term, and re-scaling of one of its terms must be applied in kind to the other terms. The application of the temporal or spatial tadpole factor to this term is then simply determined so as to be consistent with the component of the Dirac operator in question.

$$\begin{aligned}\frac{a_s^3 a_t}{\tilde{u}_t}\sum_x \bar{\psi}(x) D_0^W \psi(x) =& \frac{a_s^3 a_t}{\tilde{u}_t}\sum_x \hat{\bar{\psi}}(x) a_s^{-3/2} \hat{D}_0^W a_t^{-1} \hat{\psi}(x) a_s^{-3/2} \\ =& \frac{1}{\tilde{u}_t}\sum_x \hat{\bar{\psi}}(x) \hat{D}_0^W \hat{\psi}(x),\end{aligned} \tag{2.82}$$

where the tadpole factor $\tilde{u}_t$ is kept explicit for generality. The spatial hopping term offers the first interesting observation, and is given explicitly by;

$$\begin{aligned}\frac{\nu_s a_s^3 a_t}{\tilde{u}_s}\sum_x \bar{\psi}(x)\sum_{i=1}^3 D_i^W \psi(x) =& \frac{\nu_s a_s^3 a_t}{\tilde{u}_s}\sum_x \hat{\bar{\psi}}(x) a_s^{-3/2}\sum_{i=1}^3 \hat{D}_i^W a_s^{-1}\hat{\psi}(x) a_s^{-3/2} \\ =& \frac{\nu_s a_t}{\tilde{u}_s a_s}\sum_x \hat{\bar{\psi}}(x)\sum_{i=1}^3 \hat{D}_i^W \hat{\psi}(x) \\ =& \frac{\nu_s}{\tilde{u}_s \tilde{\gamma}_g}\sum_x \hat{\bar{\psi}}(x)\sum_{i=1}^3 \hat{D}_i^W \hat{\psi}(x) \\ =& \frac{\nu_s}{\tilde{u}_t \gamma_g}\sum_x \hat{\bar{\psi}}(x)\sum_{i=1}^3 \hat{D}_i^W \hat{\psi}(x) \\ =& \frac{1}{\tilde{u}_t \gamma_f}\sum_x \hat{\bar{\psi}}(x)\sum_{i=1}^3 \hat{D}_i^W \hat{\psi}(x),\end{aligned} \tag{2.83}$$

where the first two equalities simply show the substitution and the resultant factors of lattice spacing. The third equality then uses the formal definition $\gamma_g = a_s/a_t$, however with an additional complication whereby the renormalised gauge anisotropy $\tilde{\gamma}_g$ is chosen in place of its bare counterpart γ_g, with the justification that they are approximately equal at tree-level [6]. The motivation for this seemingly odd choice lies within the fourth equality, whereby the so called tadpole improvement hypothesis [4] is used, resulting in the substitution $\tilde{\gamma}_g = \tilde{u}_t \gamma_g / \tilde{u}_s$. This fourth equality thus changes the tadpole factors which are present within the term. The final equality then uses the parameterisation which was alluded to previously, whereby $\nu_s = \gamma_g/\gamma_f$, which is how the factor of bare fermion anisotropy γ_f appears within this part of the fermion action. It is worth noting that the above three terms constitute the original unimproved anisotropic Wilson fermion action, but now written in dimensionless form whence the anisotropy is made explicit. Furthermore, in the event that tadpole improvement is not implemented, the tadpole factors would not be present (i.e. $\tilde{u} \to 1$ in the above), the tadpole improvement hypothesis would not be used and thus the fourth equality would not be present, and the initial factor of anisotropy within the third equality would have been explicitly γ_g.

The temporal clover term is relatively straight forward and is given in dimensionless form by;

$$\begin{aligned}\frac{i a_s^4 a_t}{2\tilde{u}_t}\sum_x \bar{\psi}(x) C_t^{SW}\sum_{i=1}^3 \sigma_{0i} F_{0i}(x)\psi(x) =& \frac{i a_s^4 a_t}{2\tilde{u}_t}\sum_x \hat{\bar{\psi}}(x) a_s^{-3/2} C_t^{SW}\sum_{i=1}^3 \sigma_{0i}\hat{F}_{0i}(x) a_t^{-1} a_s^{-1}\hat{\psi}(x) a_s^{-3/2} \\ =& \frac{i}{2\tilde{u}_t}\sum_x \hat{\bar{\psi}}(x) C_t^{SW}\sum_{i=1}^3 \sigma_{0i}\hat{F}_{0i}(x)\hat{\psi}(x),\end{aligned} \tag{2.84}$$

where it is useful to reiterate that the coefficient is given here as $1/2$ rather than $1/4$ as the first index has been explicitly set to the temporal direction, $\mu = 0$, and thus no double counting is occurring within this term. The spatial clover term is more involved and is given as;

$$\begin{aligned}
\frac{ia_s^4 a_t}{4\tilde{u}_s}\sum_x \bar{\psi}(x) C_s^{SW} \sum_{i,j=1}^{3} \sigma_{ij} F_{ij}(x)\psi(x) =& \frac{ia_s^4 a_t}{4\tilde{u}_s}\sum_x \hat{\bar{\psi}}(x) a_s^{-3/2} C_s^{SW} \sum_{i,j=1}^{3} \sigma_{ij}\hat{F}_{ij}(x) a_s^{-2}\hat{\psi}(x) a_s^{-3/2} \\
=& \frac{ia_t}{4\tilde{u}_s a_s}\sum_x \hat{\bar{\psi}}(x) C_s^{SW} \sum_{i,j=1}^{3} \sigma_{ij}\hat{F}_{ij}(x)\hat{\psi}(x) \\
=& \frac{i}{4\tilde{u}_s\tilde{\gamma}_g}\sum_x \hat{\bar{\psi}}(x) C_s^{SW} \sum_{i,j=1}^{3} \sigma_{ij}\hat{F}_{ij}(x)\hat{\psi}(x) \\
=& \frac{i}{4\tilde{u}_t\gamma_g}\sum_x \hat{\bar{\psi}}(x) C_s^{SW} \sum_{i,j=1}^{3} \sigma_{ij}\hat{F}_{ij}(x)\hat{\psi}(x) \\
=& \frac{i\nu_s}{4\tilde{u}_t\tilde{u}_s^3\gamma_g}\sum_x \hat{\bar{\psi}}(x) \sum_{i,j=1}^{3} \sigma_{ij}\hat{F}_{ij}(x)\hat{\psi}(x) \\
=& \frac{i}{4\tilde{u}_t\tilde{u}_s^3\gamma_f}\sum_x \hat{\bar{\psi}}(x) \sum_{i,j=1}^{3} \sigma_{ij}\hat{F}_{ij}(x)\hat{\psi}(x),
\end{aligned} \tag{2.85}$$

where once more the first two equalities simply show the substitution and resultant factors of lattice spacing. The third equality uses the formal definition $\gamma_g = a_s/a_t$, but again replacing the bare gauge anisotropy γ_g with its renormalised counterpart $\tilde{\gamma}_g$. The fourth equality uses the tadpole improvement hypothesis $\tilde{\gamma}_g = \tilde{u}_t\gamma_g/\tilde{u}_s$. The fifth equality writes the tree-level tadpole clover coefficient C_s^{SW} in explicit form, in order to present the factor of $\nu_s = \gamma_g/\gamma_f$, which is once more used to write the term explicitly in terms of the bare fermion anisotropy γ_f.

Thus the final $\mathcal{O}(a)$-improved fermion action which is used within this work can be expressed in explicitly dimensionless form, $\hat{S}^F$ as;

$$\hat{S}^F = \sum_x \hat{\bar{\psi}}(x)\hat{D}^F\hat{\psi}(x), \tag{2.86}$$

with the dimensionless fermion Dirac operator $\hat{D}^F$, including the mass term now being given by;

$$\begin{aligned}\hat{D}^F\hat{\psi}(x) =& \frac{1}{\tilde{u}_t}\Bigg[\tilde{u}_t\hat{m}_0\hat{\psi}(x) + \hat{D}_0^W\hat{\psi}(x) + \frac{1}{\gamma_f}\sum_{i=1}^{3}\hat{D}_i^W\hat{\psi}(x) \\ &+\frac{i}{4}\Bigg(2C_t^{SW}\sum_{i=1}^{3}\sigma_{0i}\hat{F}_{0i}(x) + \frac{C_s^{SW}}{\gamma_g}\sum_{i,j=1}^{3}\sigma_{ij}\hat{F}_{ij}(x)\Bigg)\hat{\psi}(x)\Bigg] \\ =& \frac{1}{\tilde{u}_t}\Bigg[\tilde{u}_t\hat{m}_0\hat{\psi}(x) + \hat{D}_0^W\hat{\psi}(x) + \frac{1}{\gamma_f}\sum_{i=1}^{3}\hat{D}_i^W\hat{\psi}(x) \\ &+\frac{i}{4}\Bigg(\frac{1}{2}\Bigg(\frac{\gamma_g}{\gamma_f}+\frac{1}{\xi}\Bigg)\frac{2}{\tilde{u}_t\tilde{u}_s^2}\sum_{i=1}^{3}\sigma_{0i}\hat{F}_{0i}(x) + \frac{1}{\tilde{u}_s^3\gamma_f}\sum_{i,j=1}^{3}\sigma_{ij}\hat{F}_{ij}(x)\Bigg)\hat{\psi}(x)\Bigg],\end{aligned} \tag{2.87}$$

where a common factor of $\tilde{u}_t^{-1}$ has been pulled out to the front, and the explicit tree-level tadpole clover coefficients have been used in the second equality.

Performing improvement and showing the explicit manner in which the anisotropy appears for the gauge action is somewhat harder than with the fermion action. The starting point is the gauge action from eq. (2.49) in section 2.2.1, which was;

$$\begin{aligned}S^W =& \frac{\beta}{N_c}\sum_x\sum_{\mu<\nu}\mathrm{Re}(\mathrm{tr}\{1-U_{\mu\nu}(x)\}) = \frac{\beta}{2N_c}\sum_x\sum_{\mu,\nu=0}^{3}\mathrm{Re}(\mathrm{tr}\{1-U_{\mu\nu}(x)\}) \\ =& \frac{\beta}{2N_c}\sum_x\sum_{\mu,\nu=0}^{3}P_{\mu\nu}(x) \;:\; P_{\mu\nu}(x) \equiv \mathrm{Re}(\mathrm{tr}\{1-U_{\mu\nu}(x)\}).\end{aligned} \tag{2.88}$$

It is useful to reiterate that the plaquette variable is given by;

$$U_{\mu\nu}(x) = U_\mu(x)U_\nu(x+a\hat{\mu})U_\mu^\dagger(x+a\hat{\nu})U_\nu^\dagger(x), \tag{2.89}$$

with the gauge links defined as;

$$U_\mu(x) = e^{iaA_\mu(x)}. \tag{2.90}$$

Using the Baker-Campbell-Hausdorff formula;

$$e^Ae^B = e^{A+B+\frac{1}{2}[A,B]+\ldots}, \tag{2.91}$$

and the Taylor expansion;

$$A_\nu(x+a\hat{\mu}) = A_\nu(x) + a\partial_\mu A_\nu(x) + \mathcal{O}(a^2), \tag{2.92}$$

the plaquette variable can then be expressed as[30];

[30] See page 39 of [30].

$$\begin{aligned} U_{\mu\nu}(x) =& e^{ia^2 F_{\mu\nu}(x)+\mathcal{O}(a^3)} \\ \approx& 1 + (ia^2 F_{\mu\nu}(x) + \mathcal{O}(a^3)) + \frac{1}{2!}(ia^2 F_{\mu\nu}(x) + \mathcal{O}(a^3))^2 + \dots \\ \approx& 1 + ia^2 F_{\mu\nu}(x) + f(a^3) - \frac{a^4}{2} F_{\mu\nu}(x) F^{\mu\nu}(x) + f(a^5) + \mathcal{O}(a^6) + \dots, \end{aligned} \tag{2.93}$$

where in the above expansion $f(a^n)$ contains all terms of order a^n, and $\mathcal{O}(a^m)$ contains all terms of order a^m and above.

Substituting the expansion from eq. (2.93) into eq. (2.88), the Wilson gauge action can be expressed as [30, 42];

$$\begin{aligned} S^W =& \frac{\beta}{2N_c} \sum_x \sum_{\mu,\nu=0}^{3} \mathrm{Re}\left(\mathrm{tr}\left\{ 1 - (1 + ia^2 F_{\mu\nu}(x) + f(a^3) - \frac{a^4}{2} F_{\mu\nu}(x) F^{\mu\nu}(x) + f(a^5) + \mathcal{O}(a^6)) \right\} \right) \\ =& \frac{a^4 \beta}{4N_c} \sum_x \sum_{\mu,\nu=0}^{3} \mathrm{tr}\big\{ F_{\mu\nu}(x) F^{\mu\nu}(x) + \mathcal{O}(a^2) \big\}, \end{aligned} \tag{2.94}$$

where the terms with odd powers of a all cancel in the same manner as the a^3 terms [42]. It is important at this point to note that there has been no loss of generality from eq. (2.88) to eq. (2.94), with the caveat that the latter is valid for small a, which is precisely the requirement to obtain real physics in the naive continuum limit $a \to 0$. The plaquette operator eq. (2.89) is what is explicitly computed on the lattice, and the expansion eq. (2.93) shows the contents of this operator. Every term which is present within the plaquette operator continues to be present within eq. (2.94), with the realisation that the a^4 term remains explicit[31], whilst the surviving higher order terms are contained within $\mathcal{O}(a^2)$, and all other terms ultimately cancelled within the total summation shown within eq. (2.88).

The next step is to split $F_{\mu\nu}$ into temporal and spatial components and to use eq. (2.79) in order to

[31] It should be noted that the factor of a^4 is identified with the integration measure from the continuum $\int dx^4$, and thus whilst the surviving leading order term is of dimension-4, it is formally considered to be of order a^0.

explicitly show the anisotropy factors;

$$\begin{aligned}
\hat{S}^W =& \frac{a^4\beta}{4N_c}\sum_x \sum_{\mu,\nu=0}^{3} \mathrm{tr}\Big\{\hat{F}_{\mu\nu}(x)\hat{F}^{\mu\nu}(x)a_{n_1}^{-2}a_{n_2}^{-2} + \mathcal{O}(a^2))\Big\} \\
=& \frac{a_s^3 a_t\beta}{4N_c}\sum_x \Bigg(\sum_{i,j=1}^{3} \mathrm{tr}\Big\{\hat{F}_{ij}(x)\hat{F}^{ij}(x)a_s^{-4} + \mathcal{O}(a^2))\Big\}\Bigg) \\
&+\Bigg(\sum_{i=1}^{3} \mathrm{tr}\Big\{\hat{F}_{i0}(x)\hat{F}^{i0}(x)a_s^{-2}a_t^{-2} + \mathcal{O}(a^2))\Big\}\Bigg) \\
=& \frac{\beta}{4N_c}\sum_x \Bigg(\sum_{i,j=1}^{3} \frac{a_t}{a_s}\,\mathrm{tr}\Big\{\hat{F}_{ij}(x)\hat{F}^{ij}(x)\Big\} + a_s^3 a_t\,\mathrm{tr}\big\{\mathcal{O}(a^2))\big\}\Bigg) \\
&+\Bigg(\sum_{i=1}^{3} \frac{a_s}{a_t}\,\mathrm{tr}\Big\{\hat{F}_{i0}(x)\hat{F}^{i0}(x)\Big\} + a_s^3 a_t\,\mathrm{tr}\big\{\mathcal{O}(a^2))\big\}\Bigg) \\
=& \frac{\beta}{4N_c}\sum_x \Bigg(\sum_{i,j=1}^{3} \frac{1}{\gamma_g}\,\mathrm{tr}\Big\{\hat{F}_{ij}(x)\hat{F}^{ij}(x)\Big\} + a_s^3 a_t\,\mathrm{tr}\big\{\mathcal{O}(a^2))\big\}\Bigg) \\
&+\Bigg(\sum_{i=1}^{3} \gamma_g\,\mathrm{tr}\Big\{\hat{F}_{i0}(x)\hat{F}^{i0}(x)\Big\} + a_s^3 a_t\,\mathrm{tr}\big\{\mathcal{O}(a^2))\big\}\Bigg).
\end{aligned} \tag{2.95}$$

Thus far there has still been no loss of generality, and it is possible to rewrite the above in the familiar form of eq. (2.88), now with the anisotropy made explicit;

$$\hat{S}^W = \frac{\beta}{2N_c}\sum_x \Bigg(\sum_{i,j=1}^{3} \frac{1}{\gamma_g}\hat{P}_{ij}(x)\Bigg) + \Bigg(\sum_{i=1}^{3} \gamma_g \hat{P}_{i0}(x)\Bigg), \tag{2.96}$$

where the distinction between eq. (2.96) and eq. (2.88) is that the anisotropy factors are made explicit due to the operators such as $F_{\mu\nu}$ being expressed in dimensionless form, and thus the $P_{\mu\nu}$ operators are themselves now expressed in dimensionless form, as indicated by the usual hat notation. It should be understood that the terms which previously cancelled have again been included within the $\hat{P}_{\mu\nu}$ operator, with the awareness that they will cancel anyway and thus it is perfectly sound to include the same anisotropy factor in front of them. The question now is whether this same placement of the anisotropy factors is strictly correct given that it is also being applied to the contributions that are of $\mathcal{O}(a^6)$, which will be dealt with below.

The Yang-Mills term with order a^4 is precisely the correct term to regain the continuum action in the naive continuum limit. As such, all higher order terms $\mathcal{O}(a^6)$ constitute contributions to an error, in that they cause a deviation of the lattice action from the continuum action. However when the naive continuum limit is taken $a \to 0$, these terms will vanish. Consequently their effect is to change the rate at which the continuum limit can be obtained, resulting in higher computational cost to compute physical observables. It is apparent from eq. (2.94) that these errors appear at the order of a^2, which correspond to contributions from dimension-6 operators given the additional pre-factor of a^4. The unwanted contributions can thus be cancelled by the inclusion of appropriate dimension-6

operators, with the $\mathcal{O}(a^2)$-improved gauge action then being given in general terms as;

$$S^G \propto a^4 \operatorname{tr}\{F_{\mu\nu}(x)F^{\mu\nu}(x)\} + a^6 \sum_{j=1}^{3} \mathcal{O}_j(x), \tag{2.97}$$

where there are three dimension-6 operators[32] required to cancel all such contributions[42], which can be expressed as;

$$\begin{aligned}
\mathcal{O}_1(x) &= \sum_{\mu,\nu=0}^{3} \operatorname{tr}\{D_\mu F_{\mu\nu}(x) D_\mu F_{\mu\nu}(x)\}, \\
\mathcal{O}_2(x) &= \sum_{\mu,\nu,\rho=0}^{3} \operatorname{tr}\{D_\mu F_{\nu\rho}(x) D_\mu F_{\nu\rho}(x)\}, \\
\mathcal{O}_3(x) &= \sum_{\mu,\nu,\rho=0}^{3} \operatorname{tr}\{D_\mu F_{\mu\rho}(x) D_\nu F_{\nu\rho}(x)\}.
\end{aligned} \tag{2.98}$$

The first operator $\mathcal{O}_1(x)$ arises at tree-level, with $\mathcal{O}_2(x)$ and $\mathcal{O}_3(x)$ arising beyond tree-level. However the majority of the unwanted contributions can be accounted for using only the tree-level $\mathcal{O}_1(x)$ operator combined with tadpole improvement, whereas the errors being cancelled by the other two operators are relatively small and can often be ignored[43]. The three operators are shown diagrammatically in fig. 2.6.

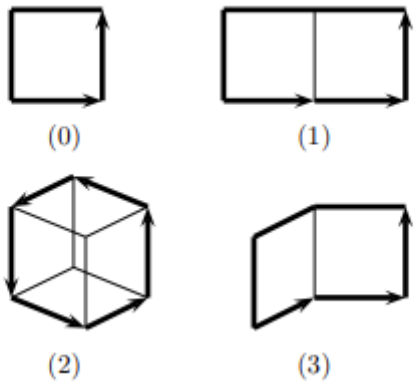

Fig. 2.6: Dimension-6 operators for $\mathcal{O}(a^2)$-improvement of the Wilson gauge action, taken from[44]. The figure labelled (0) is the basic plaquette operator for the unimproved Wilson gauge action, whilst (1), (2) and (3) are for $\mathcal{O}_1$, $\mathcal{O}_2$ and $\mathcal{O}_3$ respectively.

Thus there is only one dimension-6 term which must be checked for the manner in which the anisotropy factors appear, and the method is precisely the same as that for the dimension-4 term eq. (2.95). The result is given by;

[32] Note that for full QCD there are additional dimension-6 operators.

$$
\begin{aligned}
a^6\mathcal{O}_1(x) =& a^6 \sum_{\mu,\nu=0}^{3} \mathrm{tr}\{D_\mu F_{\mu\nu}(x) D_\mu F_{\mu\nu}(x)\} \\
=& a_s^3 a_t \Bigg(a_s^2 \sum_{i,j=1}^{3} \mathrm{tr}\Big\{ \hat{D}_i \hat{F}_{ij}(x) \hat{D}_i \hat{F}_{ij}(x) a_s^{-6} \Big\} + a_s^2 \sum_{i=1}^{3} \mathrm{tr}\Big\{ \hat{D}_i \hat{F}_{i0}(x) \hat{D}_i \hat{F}_{i0}(x) a_s^{-4} a_t^{-2} \Big\} \\
& + a_t^2 \sum_{i=1}^{3} \mathrm{tr}\Big\{ \hat{D}_0 \hat{F}_{0i}(x) \hat{D}_0 \hat{F}_{0i}(x) a_s^{-2} a_t^{-4} \Big\} \Bigg) \\
=& a_s^3 a_t \Bigg(a_s^2 \sum_{i,j=1}^{3} \mathrm{tr}\Big\{ \hat{D}_i \hat{F}_{ij}(x) \hat{D}_i \hat{F}_{ij}(x) a_s^{-6} \Big\} + a_s^2 \sum_{i=1}^{3} \mathrm{tr}\Big\{ \hat{D}_i \hat{F}_{i0}(x) \hat{D}_i \hat{F}_{i0}(x) a_s^{-4} a_t^{-2} \Big\} \Bigg) \\
=& \Bigg(\frac{1}{\gamma_g} \sum_{i,j=1}^{3} \mathrm{tr}\Big\{ \hat{D}_i \hat{F}_{ij}(x) \hat{D}_i \hat{F}_{ij}(x) \Big\} + \gamma_g \sum_{i=1}^{3} \mathrm{tr}\Big\{ \hat{D}_i \hat{F}_{i0}(x) \hat{D}_i \hat{F}_{i0}(x) \Big\} \Bigg),
\end{aligned}
\tag{2.99}
$$

where in the third equality, the second temporal term has been dropped, as $a_t \ll a_s$ and thus the a_t^2 corrections are negligible. A few words are in order regarding the factors of lattice spacing in the above expression. Within the first term of the second equality, the additional factor of a^2 is taken to be entirely spatial due to the fact that if the factor was $a_t a_s$ then the spatial anisotropy factor would be γ_g^{-2}, whilst for a factor of a_t^2 the resultant anisotropy factor is γ_g^{-3}, which in either case is incorrect for the spatial component of the action. Moreover it should be explicitly stated that whilst the temporal and spatial components can, and indeed should, contain different factors of anisotropy from one another, the various spatial terms within the action should possess the same level of anisotropy, and likewise for the various temporal terms. Furthermore in the second term of the second equality, for a factor of $a_s a_t$ there would be complete cancellation of lattice spacing factors and thus no anisotropy would exist, whereas for a factor of a_t^2 the resultant anisotropy would be γ_g^{-1}, and thus the factor must in fact be a_s^2. Similarly for the third term, a factor of $a_s a_t$ would result in γ_g^2 whereas a factor of a_s^2 would result in γ_g^3, with a factor of a_t^2 giving the expected factor of γ_g for the anisotropy for the second temporal term. It should be noted that this is exactly in line with expectations, as the rectangular operators shown in fig. 2.6 have 6 spatial contributions in total, and also 6 temporal contributions, three of which are those which extend twice in the temporal direction and thus the identification of the third term as being the one of order a_t^2 which ought to vanish for the case where $a_t \ll a_s$.

From this point, it is now possible to incorporate the extra dimension-6 operator $\mathcal{O}_1$ into the initial unimproved anisotropic Wilson gauge action eq. (2.96), where motivated by the form of this operator shown within fig. 2.6, the new rectangular contributions will be notated by $R_{\mu\nu}$. The general form of the tree-level $\mathcal{O}(a^2)$-improved gauge action is given as;

$$\begin{aligned}\hat{S}^G =&\frac{\beta}{N_c}\sum_x\left\{\frac{1}{\gamma_g}\sum_{i<j}\left[c_0\hat{P}_{ij}(x)+c_1\left(\hat{R}_{ij}(x)+\hat{R}_{ji}(x)\right)\right]\right.\\&\left.+\gamma_g\sum_{i=1}^{3}\left[c_0\hat{P}_{i0}(x)+c_1\left(\hat{R}_{i0}(x)+\hat{R}_{0i}(x)\right)\right]\right\}\\=&\frac{\beta}{N_c}\sum_x\left\{\frac{1}{\gamma_g}\sum_{i<j}\left[c_0\hat{P}_{ij}(x)+c_1\left(\hat{R}_{ij}(x)+\hat{R}_{ji}(x)\right)\right]\right.\\&\left.+\gamma_g\sum_{i=1}^{3}\left[(c_0+4c_1)\hat{P}_{i0}(x)+c_1\hat{R}_{i0}(x)\right]\right\},\end{aligned} \tag{2.100}$$

where the first equality is the most general form, and the second equality again uses the fact that $a_t \ll a_s$ in order to justify the removal of the rectangle which extends twice into the temporal direction. The coefficients can take various values, several choices of note are given by;

$$c_0 = 1,\ c_1 = 0, \tag{2.101}$$

$$c_0 = \frac{5}{3},\ c_1 = \frac{-1}{12}, \tag{2.102}$$

$$c_0 = 3.648,\ c_1 = -0.331. \tag{2.103}$$

The first set of values are the coefficients required to regain the original Wilson gauge action. The second pair of values are from tree-level Symanzik improvement[44], with the final pair due to the proposal of Iwasaki[45], and are based on renormalisation-group methods. Futhermore the requirement $c_0 + 8c_1 = 1$ ensures the correct normalisation of the bare coupling g_0, whilst the constraint $c_0 > 0$ ensures that all fields are locally pure gauge configurations[42].

Within this work $\mathcal{O}(a^2)$-improvement is achieved using tree-level Symanzik improvement, and thus when combined with tadpole improvement in the previously defined manner results in a final gauge action of the form;

$$\begin{aligned}\hat{S}^G =&\frac{\beta}{N_c}\sum_x\left\{\frac{1}{\gamma_g}\sum_{i<j}\left[\frac{5}{3u_s^4}\hat{P}_{ij}(x)-\frac{1}{12u_s^6}\left(\hat{R}_{ij}(x)+\hat{R}_{ji}(x)\right)\right]\right.\\&\left.+\gamma_g\sum_{i=1}^{3}\left[\frac{4}{3u_s^2u_t^2}\hat{P}_{i0}(x)-\frac{1}{12u_s^4u_t^2}\hat{R}_{i0}(x)\right]\right\}.\end{aligned} \tag{2.104}$$

The present work was performed using the FASTSUM configurations, which were generated using the aforementioned gauge action, eq. (2.104), and fermion action, eq. (2.86), with the parameters specified within table 2.6.

γ_g	4.3	C_s^{SW}	1.589	u_s	0.7336
γ_f	3.4	C_t^{SW}	0.903	u_t	1
$\tilde{\gamma}_f$	3.453(6)	$a_t m_u, a_t m_d$	-0.0860	$\tilde{u}_s$	0.9267
a_s	0.11208(31) fm	$a_t m_s$	-0.0743	$\tilde{u}_t$	1
a_t	0.032459(71) fm	M_π	236(2) MeV	β	1.5

Table. 2.6: Parameters for the action used by the FASTSUM collaboration in order to generate (Gen2L) configurations with $N_f = 2 + 1$ flavours. The values for the bare anisotropy factors and the tadpole factors, and thus clover coefficients, were determined in [2], whilst the value for the strange quark mass was obtained in [46], and then the target renormalised anisotropy, pion mass, light quark masses and lattice spacings being determined in [47, 48]. Note that here $\tilde{\gamma}_f = a_s/a_t$ and represents the renormalised fermion anisotropy, whereas γ_g and γ_f represent the bare gauge and fermion anisotropy respectfully.

2.2.4 Configuration Generation

This section will outline the manner in which the aforementioned actions, eq. (2.86) and eq. (2.104), with the associated parameters, table 2.6, are used to generate the field configurations which are used within the lattice approach to compute physical observables. The work presented within this thesis relies on previously generated FASTSUM configurations, and thus this exposition will be kept to a brief outline. The intricacies for generating lattice QCD gauge field configurations can get very technical, however the same key machinery can be easily displayed with the simpler case of lattice scalar field theory, which will thus be the case of interest below. This section follows closely the exposition given in [49]. An analogous overview for QCD can be found in chapter's 4 and 8 of [30].

The discrete lattice action for scalar field theory is given by;

$$S[\phi] = \sum_x \big[-2\kappa \sum_{\mu=1}^{D} \phi_x \phi_{x+\hat{\mu}} + \phi_x^2 + \lambda(\phi_x^2 - 1)^2 \big], \tag{2.105}$$

with the lattice expectation value of some observable O then being;

$$< O[\phi] >= \frac{1}{Z} \int \prod_x d\phi_x e^{-S[\phi]} O[\phi] : Z = \int \prod_x d\phi_x e^{-S[\phi]}. \tag{2.106}$$

Computing the partition function by brute force is unrealistic due to its size, however not all configurations contribute equally, and a good approximation can be achieved by considering only the subset of configurations that contribute significantly. This is called importance sampling and can be achieved by generating field configurations which are distributed according to the Boltzmann weight $e^{-S[\phi]}$, where the most important configurations, which are those with a smaller action, are more likely to be sampled. Thus, the objective is to obtain a series of field configurations, $\phi_1, \phi_2, ..., \phi_N$, in order to then estimate the expectation value from an average over measurements on those configurations;

$$< O >= \frac{1}{N} \sum_i^N O[\phi_i] + \mathcal{O}\left(\frac{1}{\sqrt{N}}\right), \tag{2.107}$$

where the second term is the error, which is entirely statistical. In order to ensure that the field configurations are distributed according to the required Boltzmann weight $e^{-S[\phi]}$, the configurations must be generated using a Markov process[33] which guarantees that configurations with larger probability are visited more often. Furthermore in order to achieve a good approximation it is required that any configuration can be obtained within a finite number of steps, which is called strong ergodicity.

Those algorithms which implement a Markov process, necessarily produce field configurations that are auto-correlated. From statistical mechanics the variance of some observable O is given by;

$$\text{Var}[O] =< (O- < O >)^2 > , \tag{2.108}$$

whereas the variance for the case of auto-correlated configurations is given by;

$$\text{Var}[O] =< (O- < O >)^2 > \left(\frac{2\tau_O}{N}\right), \tag{2.109}$$

where τ_O is the integrated auto-correlation time[34], and must be computed separately for each observable. The variance from statistical mechanics is dependent on the underlying QFT, whereas in the case of generating a Markov chain of field configurations the variance will additionally depend on the algorithm used via the τ factor and on the number of configurations N.

The Hybrid Monte Carlo (HMC) algorithm is the most common choice for generating the Markov chain of field configurations in full QCD, due to its high effectiveness. The HMC algorithm introduces an auxiliary field π_x, resulting in an enlarged partition function;

$$Z = \int \prod_x d\pi_x d\phi_x e^{-H(\pi,\phi)}. \tag{2.110}$$

The exponent in the modified Boltzmann weight is given by;

$$H(\pi,\phi) = \frac{1}{2}\sum_x \pi_x^2 + S[\phi], \tag{2.111}$$

with the arbitrary coefficient in the first term being chosen in analogy to the kinetic energy and $S[\phi]$ being thought of as a potential within a Hamiltonian $H(\pi,\phi)$. It is important to note that this is simply an analogy with classical mechanics[35], and indeed the purpose of adding the auxiliary field π_x is to permit the evolution of the field ϕ through phase space via Hamiltonian mechanics such that the field configurations are distributed according to $e^{-S[\phi]}$. In this context, the update of the field ϕ

[33] The algorithms that perform a Markov process are not guaranteed to start at an appropriate point in phase space, where the most important configurations exist. Typically an initial burn in period has to be performed, after which the correct equilibrium distribution will have been converged on, and the subsequently generated configurations are appropriate for use in computing observables.

[34] The auto-correlation time τ (also known as Monte Carlo time) is a fictitious time through which the fields ϕ and π evolve in the Markov chain.

[35] The field ϕ can be thought of as the generalised coordinate, with the field π being the corresponding conjugate momentum.

according to the Hamiltonian equations of motion;

$$\frac{d\phi}{d\tau} = \frac{\partial H}{\partial \pi}, \tag{2.112}$$

$$\frac{d\pi}{d\tau} = -\frac{\partial H}{\partial \phi}, \tag{2.113}$$

is known as Molecular Dynamics (MD) evolution. These equations of motion do not represent the underlying QFT, they simply represent the recipe for obtaining an ensemble of field configurations using the HMC algorithm. The above equations of motion are solved using numeric integration, which will always include some non-zero error, and thus the trajectory update will not be exact. However for studies of non-zero temperature it is required for the update to be exact, and thus a Metropolis accept-reject step is included in order to stochastically correct the error. The Metropolis step requires that the integration scheme is reversible and area preserving. This requirement is known as detailed balance, which ensures that the algorithm is convergent. Hence, in order for the update procedure to result in field configurations distributed according to the Boltzmann weight $e^{-S[\phi]}$, both the Hamiltonian $H(\pi, \phi)$ and the phase-space volume $d\pi d\phi$ must be conserved.

The total Monte Carlo time τ that is integrated over between successive field configurations is referred to as a trajectory. In order to obtain the next field configuration in the Markov chain, ϕ_2, the following three steps are taken with the starting point of some initial field configuration ϕ_1;

1. Momentum heat bath step,
2. Molecular Dynamics evolution,
3. Metropolis accept-reject step.

The momentum heat bath step involves generating new values for the conjugate momenta π_i from a Gaussian distribution. Each attempt at a trajectory update involves taking a uniformly distributed[36] random number $x \in [0, 1)$. A procedure such as the Box-Muller method is then used, whereby normally distributed random numbers are generated from the uniformly distributed random numbers via;

$$y_1 = \sqrt{-2\ln(1-x_1)}\cos(2\pi(1-x_2)), y_2 = \sqrt{-2\ln(1-x_1)}\sin(2\pi(1-x_2)), \tag{2.114}$$

where two inputs are required and two Gaussian random numbers are given as output. Strong ergodicity is ensured by repeating this momentum heat bath step when computing each new proposed trajectory. The initial field configuration ϕ_1 is also generated using a heat bath step.

In those cases where the computational requirements are very large, the Hamiltonian is decomposed for efficiency $H(\pi, \phi) = H_1(\pi) + H_2(\phi)$. The trajectory Monte Carlo time step τ is then split into M pieces[37] of size ϵ. The MD evolution is then performed by repeatedly implementing two steps, each of size ϵ, M times such that the total step size τ is achieved. The first step involves updating the

[36] This is done by using a random number generator such as that described within [50].
[37] These are typically equally spaced, although in principle they can vary in size providing that $\sum_i \epsilon_i = \tau$.

field configuration ϕ whilst holding π constant;

$$(\pi, \phi) \rightarrow (\pi, \phi + \epsilon \nabla_\mu H_1(\pi)), \tag{2.115}$$

with the second step updating only π;

$$(\pi, \phi) \rightarrow (\pi - \epsilon \nabla_\phi H_2(\phi), \phi). \tag{2.116}$$

In analogy[38] with classical mechanics the terms $F_\phi = -\nabla_\phi H_2(\phi)$ and $F_\pi = \nabla_\pi H_1(\pi)$ are called molecular dynamics forces. The Leap-Frog integrator is one of the most common choices for performing the MD evolution, whereby ϕ is updated twice, each with step size $\epsilon/2$, with an intermediate update of π with step size ϵ. The error is dependant on the choice of integrator, with the Leap-Frog being a second order integrator due to its leading error being of order $\mathcal{O}(\epsilon^2)$.

The explicit combination of the heat bath and MD evolution steps is called hybrid molecular dynamics, and this is a suitable recipe for a trajectory update providing that the MD evolution can be performed exactly. In practice, due to the integrator error the inclusion of the Metropolis step is required, resulting in the HMC algorithm, which provides an overall exact trajectory update. The Metropolis step involves accepting the update for the fields $(\pi_1, \phi_1) \rightarrow (\pi_2, \phi_2)$, based on some probability;

$$\min(1, e^{-\Delta H}) : \Delta H = H(\pi_2, \phi_2) - H(\pi_1, \phi_1), \tag{2.117}$$

such that $H(\pi_2, \phi_2) \leq H(\pi_1, \phi_1)$ results in the update being accepted, otherwise the update will be accepted with probability $e^{-\Delta H}$. If the update is accepted then the next trajectory update step begins, otherwise the current step will be restarted with a new value for π from the heat bath step[39].

Whilst the generation of configurations for QCD is more complicated than for a scalar field theory, the basic steps within the HMC algorithm still apply. Modern QCD studies are performed using $N_f = 2+1$ quark flavours, where the up and down quarks are taken to have the same mass, with the mass of the strange quark taking its physical value. However the HMC algorithm cannot be used for non-integer values of $\alpha = N_f/2$, and thus is not suitable for such modern studies. Furthermore, simulations using lighter quark masses are considerably more expensive, and as increasingly precise studies are performed, the quark masses are required to be taken closer to their physical values. Consequently the efficiency of the available algorithms becomes more important, and the expense of the HMC algorithm becomes prohibitively excessive. There are several alternate algorithms which can handle $N_f = 2 + 1$ studies, the most efficient and thus popular of which is the Rational Hybrid Monte Carlo (RHMC) algorithm, which is a variant of the HMC algorithm. Additionally, further improvements to the efficiency are possible through various methods which can be used in conjunction

[38] These are not the forces of the underlying QFT, this is simply an analogy.

[39] In the event that the integrator step ϵ is too large and thus $H(\pi_2, \phi_2) \gg H(\pi_1, \phi_1)$, then the update will still be accepted with probability $e^{-\Delta H}$. However this could result in the current update step being repeatedly restarted and eventually being accepted due to the probability condition. In order to determine whether such an inappropriate update has occurred it is necessary to observe the rate at which proposed updates are accepted. This acceptance rate should be at around $80 - 90\%$ in order to ensure that the constructed Markov chain of field configurations is valid. Additionally a validity condition of $< e^{-\Delta H} >= 1$ may be used.

with RHMC. Such technicalities are rather involved and not relevant to the work of interest here, however the details behind the RHMC algorithm and the additional methods can be found in [51], with details specific to the generation of the FASTSUM configurations available within [2].

2.3 High Temperature QCD

One of the motivating factors for studying QCD at non-zero temperature is that QCD predicts that at some critical temperature, $T_c \approx 200\ MeV$, there is a transition from the confined hadronic state of matter, to a deconfined state of asymptotically free quarks and gluons called the Quark Gluon Plasma (QGP). The spontaneously broken chiral symmetry is also regained at this critical temperature. In the early moments of the universe, roughly $10^{-5}\ s$ after the big bang, space was filled with a QGP, and understanding how the universe then evolved into what is seen today requires the non-perturbative study of QCD across a range of temperatures. These conditions are probed experimentally at facilities such as the Relativistic Heavy Ion Collider (RHIC) and the Large Hadron Collider (LHC). The RHIC uses nuclei as heavy as gold, with a resulting relativistic centre of mass energy of $E \approx 200n$ GeV, where n is the number of nucleons in a single nucleus. The LHC achieves yet higher energies by using lead nuclei, reaching relativistic center of mass energies of $E \approx 2.76n$ TeV.

From the theoretical side of the coin, such studies involve the use of hydrodynamics in order to simulate the evolution of the resultant fireball of nuclear matter. The usefulness of lattice QCD is that it can determine the relevant low energy input parameters for the hydrodynamics simulations such as pressure and temperature, which are intensive quantities that can vary in space and time but at a sufficiently low rate such that the system posses an approximate local thermal equilibrium. The stages of the thermalisation process are shown within fig. 2.7. Hydrodynamics is used to describe the system in between the stages of thermalisation and hadronisation, i.e. $\tau_0 < \tau < \tau_f$ within fig. 2.7, and can be considered as a low-energy effective theory, with its parameters encoding the infrared behaviour of QCD, which in this case is the corresponding underlying microscopic theory[40]. Such studies are important for understanding QCD itself, but moreover for understanding issues within early universe cosmology and astro-particle physics. For example, the QGP is an important element in understanding the baryon asymmetry and the seeding for structure formation of galaxies.

In order to understand the strong interactions fully, QCD must be understood across a range of conditions, as indicated by the phase diagram in fig. 2.8 which shows the phases of strongly interacting matter for a range of values of temperature T, and baryon chemical potential (net baryon density) μ_B. The deployment of lattice field theory to explorations of the phase diagram for non-zero values of chemical potential are hindered by the infamous sign problem. The work presented here will focus on the conditions of the early universe however, which are described by the slice of the phase diagram at $\mu_B = 0$ where no such technical difficulties arise, and so such complexities will not be discussed here. At a low enough temperature, roughly $T < 200$ MeV, strongly interacting matter takes on the hadronic phase whereby quarks and gluons are strongly interacting and thus cannot be

[40] For a brief review on effective field theory and renormalisation, see chapter 5.

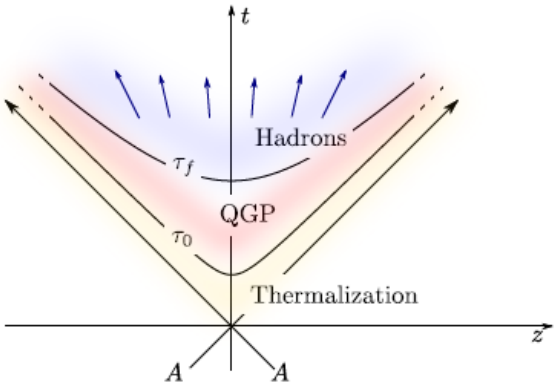

Fig. 2.7: Stages of the thermalisation process for the QGP [52]. The system reaches local thermal equilibrium, then the QGP exists up until the point where chemical and thermal freezout occur, whereby hadronisation then takes place.

described using perturbation theory. The manner in which the matter transitions into the deconfined QGP phase is also not within the scope of perturbation theory, for much the same reason, as the interactions are not yet sufficiently weak at the relevant temperature. The nature of this phase transitions has been shown by lattice calculations to be that of a crossover, where the matter slowly changes from one state to another, rather than a first or second order phase change. Consequently the transition cannot be explicitly claimed to take place at some specific temperature, however for a given observable there will exist a clear inflection point, which is often used to denote the transition temperature T_c, for that particular observable. This change of state at the crossover region relates to the spontaneous breaking of chiral symmetry, and can be observed using the chiral condensate as an order parameter[41]. More details about the QGP can be found within [52].

Some intuition of what will happen with varying temperature at $\mu_B = 0$ can however be gained without the use of lattice methods. The Deconfined QGP phase is obtained in the high temperature limit, and can be modelled by an ideal (non-interacting) gas with a pressure given by;

[41] More details on chiral symmetry, symmetry breaking and the chiral condensate can be found in chapter 5.

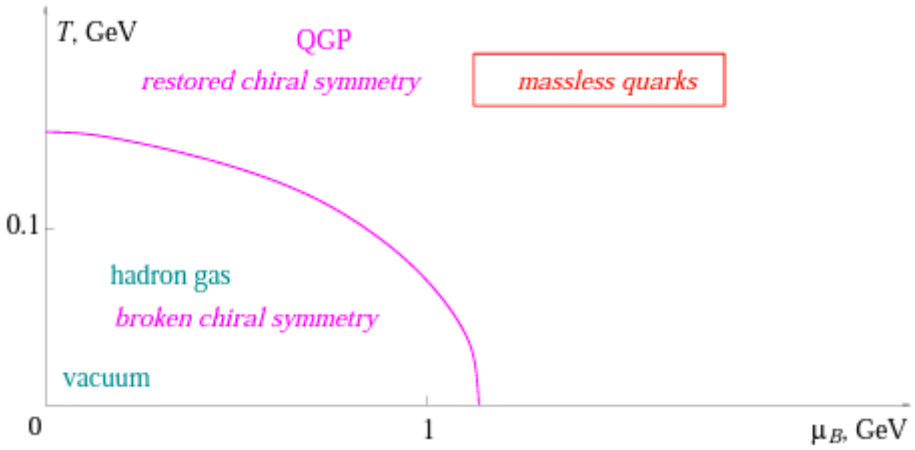

Fig. 2.8: Phase diagram for QCD, showing the state of strongly interacting matter across a range of values for temperature T and baryon chemical potential $\mu \equiv \mu_B$. This image was taken from [53].

$$\frac{p}{T^4} = \left(16 + \frac{7}{8}12N_f\right)\frac{\pi^2}{90}. \tag{2.118}$$

Conversely the confined hadronic phase exists at the low temperature limit, and can be modelled by a weakly interacting gas of hadrons, the so called hadron resonance gas model, with a pressure given as;

$$\frac{p}{T^4} = 3\frac{\pi^2}{90}. \tag{2.119}$$

It should then be clear that for $N_f = 2+1$, the pressure is expected to increase as the system evolves through the crossover region where the phase transition occurs. However these models only serve as a guide, and ultimately the goal is to compute thermodynamic quantities from first principles. In section 2.2 a formula from statistical mechanics was presented, eq. (2.32), which expresses the expectation value of some observable O, which is restated in more general terms for convenience here;

$$< O >= \frac{1}{Z}\sum_i \rho O[i], \tag{2.120}$$

where ρ is a generic Boltzmann weight factor and i is an arbitrary configuration that the system may be in. According to statistical mechanics there are many thermodynamics quantities that can be computed for a system in thermal equilibrium by taking the appropriate derivatives of the partition function. The Helmholtz free energy is given by;

$$F = -T\ln(Z), \tag{2.121}$$

with T being the temperature, and the pressure then being computed as the following derivative;

$$p = \frac{\partial(T\ln(Z))}{\partial V}, \tag{2.122}$$

where V is the spatial volume. Similarly the entropy of the system is given as the derivative;

$$S = \frac{\partial(T\ln(Z))}{\partial T}, \tag{2.123}$$

with the energy for the case of zero baryon chemical potential then being given by the sum;

$$E = -pV + ST. \tag{2.124}$$

In order to evaluate the Euclidean correlation function that was expressed in eq. (2.27), it is necessary to use Monte Carlo importance sampling due to the very high dimensionality of the functional integral. The issue with the above thermodynamic expressions is that when performing a Monte Carlo simulation, it is unfortunately not possible to directly access the partition function and hence these expressions cannot be evaluated in their present form. There are several approaches that

are in practice used to compute the desired thermodynamic quantities, such as to calculate the energy-momentum tensor $T_{\mu\nu}$, whose contents contain information on quantities such as the energy and pressure. Unfortunately computing $T_{\mu\nu}$ on the lattice is somewhat difficult in itself, and there are several approaches that have been used to overcome these difficulties. The various methods for computing thermodynamic properties on the lattice will be will be discussed in detail within chapter 4, with particular attention to the determination of the energy-momentum tensor through the use of gradient flow, the latter of which will be discussed presently.

2.4 Gradient Flow

Gradient flow is a quantum field theoretic tool for applying heat-equation evolution to fields, allowing for the construction of semi-local operators which acts as an effective filter for ultraviolet fluctuations. The flow is applied on a per configuration basis, with the fields used to construct operators essentially replaced by a semi-local average. Gradient flow is a non-perturbative method that respects gauge invariance.

One of the earliest occurrences of gradient flow was by Atiyah and Bott [54], where within mathematics the term often used is Yang-Mills gradient flow. Gradient flow has found a number of application within physics, from scale setting [55, 56], amelioration of ultraviolet fluctuations [57], and dealing with issues of renormalisation [58, 66]. Other interesting applications include in the study of beyond the standard model physics [59, 60], improving the efficiency of the HMC algorithm [61], dark matter models [62], super-symmetric Yang-Mills theory [63] and infinite N phase transitions [64].

Gradient flow is defined for gauge fields in the continuum as;

$$\frac{\partial B_\mu(x,\tau)}{\partial \tau} = D_\nu G_{\nu\mu}(x,\tau), \tag{2.125}$$

where the flowed field strength tensor is given by;

$$G_{\nu\mu}(x,\tau) = \partial_\nu B_\mu(x,\tau) - \partial_\nu B_\mu(x,\tau) + [B_\nu(x,\tau), B_\mu(x,\tau)], \tag{2.126}$$

and the associated initial conditions;

$$B_\mu(x,\tau=0) = A_\mu(x), \tag{2.127}$$

and;

$$G_{\nu\mu}(x,\tau=0) = F_{\nu\mu}(x). \tag{2.128}$$

The ultraviolet smoothing effect of gradient flow can be shown explicitly by looking at the continuum

flow equations perturbatively. It is preferable to show this using a modified version of the flow equation in order to side step some technical complexities which arise during perturbative analysis due to the gauge invariance of the flow equation. The modified flow equation takes the form;

$$\frac{\partial B_\mu(x,\tau)}{\partial \tau} \equiv \dot{B}_\mu(x,\tau) = D_\nu G_{\nu\mu}(x,\tau) + \lambda D_\mu \partial_\nu B_\nu, \tag{2.129}$$

where the additional term serves to damp the evolution of the gauge field, without interfering with the value of the gauge invariant observables [58]. The dependence on the flowed gauge field can be made explicit, temporarily dropping the arguments x and τ for simplicity;

$$\begin{aligned}\dot{B}_\mu = {} & \partial_\nu\partial_\nu B_\mu - \partial_\nu\partial_\mu B_\nu + \partial_\nu[B_\nu, B_\mu] \\ & + [B_\nu, \partial_\nu B_\mu] - [B_\nu, \partial_\mu B_\nu] + [B_\nu, [B_\nu, B_\mu]] \\ & + \lambda\partial_\mu\partial_\nu B_\nu + \lambda[B_\mu, \partial_\nu B_\nu],\end{aligned} \tag{2.130}$$

which can then be split into linear terms and a remainder R_μ;

$$\dot{B}_\mu = \partial_\nu\partial_\nu B_\mu + (\lambda - 1)\partial_\mu\partial_\nu B_\nu + R_\mu, \tag{2.131}$$

with the remainder term;

$$R_\mu = 2[B_\nu, \partial_\nu B_\mu] - [B_\nu, \partial_\mu B_\nu] + (\lambda - 1)[B_\mu, \partial_\nu B_\nu] + [B_\nu, [B_\nu, B_\mu]], \tag{2.132}$$

having used the substitution;

$$\partial_\nu[B_\nu, B_\mu] = [B_\nu, \partial_\nu B_\mu] - [B_\mu, \partial_\nu B_\nu]. \tag{2.133}$$

It is convenient to choose $\lambda = 1$ resulting in the simplification;

$$\dot{B}_\mu - \partial_\nu\partial_\nu B_\mu = R_\mu, \tag{2.134}$$

and remainder term;

$$R_\mu = 2[B_\nu, \partial_\nu B_\mu] - [B_\nu, \partial_\mu B_\nu] + [B_\nu, [B_\nu, B_\mu]]. \tag{2.135}$$

Following [67], in perturbative studies the fundamental gauge field is scaled with the bare coupling g_0, such that $A_\mu \to g_0 A_\mu$. The functional integral in then expanded in powers of g_0 resulting in the flow being expressed as an asymptotic expansion;

$$B_\mu = \sum_{k=1}^{\infty} g_0^k B_{\mu,k} \,:\, B_{\mu,k}|_{\tau=0} = \delta_{k1} A_\mu. \tag{2.136}$$

Inserting eq. (2.136) into eq. (2.134) results in the equations;

$$\dot{B}_{\mu,k} - \partial_\nu \partial_\nu B_{\mu,k} = R_{\mu,k} \,:\, k = 1, 2, \ldots, \tag{2.137}$$

where the first few remainder terms are given by;

$$R_{\mu,1} = 0, \tag{2.138}$$

$$R_{\mu,2} = 2[B_{\nu,1}, \partial_\nu B_{\mu,1}] - [B_{\nu,1}, \partial_\mu B_{\nu,1}], \tag{2.139}$$

$$\begin{aligned} R_{\mu,3} = {} & 2[B_{\nu,2}, \partial_\nu B_{\mu,1}] + 2[B_{\nu,1}, \partial_\nu B_{\mu,2}] \\ & + [B_{\nu,2}, \partial_\mu B_{\nu,1}] + [B_{\nu,1}, \partial_\mu B_{\nu,2}] + [B_{\nu,1}, [B_{\nu,1}, B_{\mu,1}]]. \end{aligned} \tag{2.140}$$

To leading order the flow is thus;

$$\dot{B}_{\mu,1} - \partial_\nu \partial_\nu B_{\mu,1} = 0, \tag{2.141}$$

which is of the form of the heat equation. The heat equation in general terms takes the form (with some initial condition and boundary condition);

$$\frac{\partial u(x,\tau)}{\partial \tau} - \nabla^2 u(x,\tau) = 0 \,:\, x \in \mathbb{R}^n,\, 0 < \tau < \infty, \tag{2.142}$$

with a solution then being expressed in terms of the fundamental solution (or Greens function) $\sigma(x,\tau)$;

$$u(x,\tau) = \int_{-\infty}^{\infty} \sigma(x-\xi,\tau) f(\xi) d\xi. \tag{2.143}$$

The fundamental solution, which in this context is also referred to as the heat kernel, is given as the solution to the auxiliary homogeneous problem;

$$\frac{\partial}{\partial \tau}\sigma(x,\tau) - \nabla^2 \sigma(x,\tau) = 0 \,:\, x \in \mathbb{R}^n,\, \tau > 0, \tag{2.144}$$

with initial condition;

$$\sigma(x,0) = \delta(x) \,:\, x \in \mathbb{R}^n. \tag{2.145}$$

For the one dimensional case the fundamental solution is given as;

$$\sigma(x,\tau) = \frac{e^{-x^2/4\tau}}{(4\pi\tau)^{1/2}}. \tag{2.146}$$

For the case in question, the flowed gauge field is then given in D dimensions as;

$$B_{\mu,1}(x,\tau) = \int K_\tau(x-y)A_\mu(y)d^D y, \tag{2.147}$$

with the heat kernel;

$$K_\tau(z) = \frac{e^{-z^2/4\tau}}{(4\pi\tau)^{D/2}}, \tag{2.148}$$

which makes explicit that the gradient flow is in fact a smoothing operation, which averages the gauge potential in four dimensions across a spherical volume of radius $\sqrt{8\tau}$. This averaging over local values is visualised in fig. 2.9.

It is a general property of the heat equation that discontinuities and singularities within the initial condition are rapidly smoothed out. This smoothing property of the flow then implies that for non-zero flow time $\tau > 0$, there exist no short distance (ultraviolet) singularities for correlation functions built from these flowed fields.

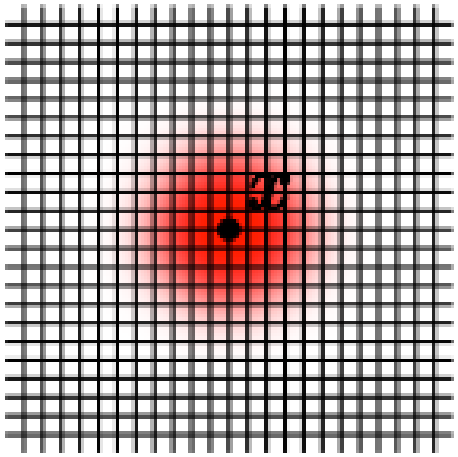

Fig. 2.9: A generic field $O(x,\tau)$ for positive flow time $\tau > 0$ depends on the value of the original unflowed field variable $O(x,0)$ within some local region of diameter $2\sqrt{8\tau}$. Figure taken from [55].

The lattice discretisation of the flow equation eq. (2.125) is given by;

$$a^2\partial_\tau V_\mu(x,\tau) = -g_0^2\{T^a\partial^a_{x,\mu}S_G(V)\}V_\mu(x,\tau) : V_\mu(x,0) = U_\mu(x), \tag{2.149}$$

where $S_G(V)$ is any lattice action, with the Lie derivative;

$$\partial^a_{x,\mu}f(U) = \frac{d}{ds}f(e^{sX(y,\nu)}U)|_{s=0}, \tag{2.150}$$

where;

$$X(u,\nu) = T^a \text{iff } (y,\nu) = (x,\mu),\ 0 \text{ otherwise.} \tag{2.151}$$

The gradient flow is intimately related to the older approach of stout link smearing [41], in that successive smearing steps essentially amount to the same procedure but performed with an Euler

integration scheme. A brief outline of general smearing in gauge theory can be found within [65]. The gauge action used within the flow equation eq. (2.149) provides some level of freedom for performing gradient flow. All possible valid choices for the flow action should reproduce the same Yang-Mills gradient flow, eq. (2.125), in the continuum limit. The work presented in this thesis uses the Wilson plaquette action within the flow equation, thus then being referred to as Wilson flow.

This chapter has covered the basic background material required for understanding the work presented within this thesis. Next, chapter 3 will walk through the validation of the anisotropic Wilson flow and will perform basic tests for numerical stability of the integrator. Then chapter 4 will present the specific background details and the results for the main work of this thesis.

Chapter 3

Validation of Anisotropic Flow and Numerical Stability Checks

In order to ensure that the anisotropic gradient flow is being correctly implemented, a sanity check must be performed utilising a known result to act as a benchmark. The implementation of such a check was performed by using the method set out by Fodor et al within [68], whereby the anisotropic gradient flow is used to compute the renormalised gauge anisotropy $\tilde{\gamma}_g$. In the current work the Gen2L configurations were used, for which $\tilde{\gamma}_f$ is already known, thus providing a clear method and target result in the instance where the implementation of the anisotropic gradient flow is correct. Within this chapter the outline and results for this sanity check will be presented, along with some tests for the numerical stability of the integrator.

The discretised lattice flow equation can be written as;

$$\frac{dU_\mu}{d\tau} = X_\mu(U)U_\mu, \tag{3.1}$$

where τ is the flow time, U_μ is the lattice gauge link which is an element of the Lie group whereas $X_\mu(U)$ is an element of the associated Lie algebra and is also the generator of the stout smearing transformation;

$$X_\mu(x,\tau) = P_A\left[\sum_{\pm\nu\neq\mu} \rho_{\mu\nu}U_\nu(x,\tau)U_\mu(x+\nu,\tau)U_\nu^\dagger(x+\mu,\tau)U_\mu^\dagger(x,\tau)\right], \tag{3.2}$$

where P_A is an operator projecting onto traceless anti-hermitian matrices, and the coefficients $\rho_{\mu\nu}$ are defined below. The above expression holds true for both the isotropic and anisotropic cases. Moreover this uses the specific choice of the Wilson gauge action, and so is more specifically referred to as the Wilson flow, rather than the more general gradient flow.

The Wilson flow provides a length scale, $\sqrt{t_0}$, which can be used in lattice computations to set the scale [67]. However in [56] Fodor et al derived an alternate scale using the Wilson flow, ω_0,

which has the benefits of being measurable to high precision on the lattice, being defined without fitting or extrapolation, having small quark mass dependence and not depending on the details of the discretisation. The ω_0 scale was computed in physical units within [56], and found to be $\omega_0 = 0.1755(18)(04)$ fm, using the definition for the isotropic case;

$$\left[\tau\frac{d}{d\tau}\tau^2 < E(\tau) >\right]_{\tau=\omega_0^2} = 0.30, \tag{3.3}$$

with the Yang-Mills action density;

$$E(\tau) = \frac{1}{4}\sum_x F^2_{\mu\nu}(x,\tau). \tag{3.4}$$

When using an anisotropic lattice the constraints $\rho_{i0} = \gamma_w^2$ and $\rho_{ij} = \rho_{0i} = 1$ are imposed to ensure that the correct flow equation is regained in the continuum limit. In the simple case of a non-interacting theory, the bare and renormalised gauge anisotropies are equal, $\gamma_g = \tilde{\gamma}_g$. For the interacting theory, the action is expressed in terms of unrenormalised fields and the bare gauge anisotropy γ_g, which describes the theory on the scale of the lattice spacing. Moreover the renormalised gauge anisotropy $\tilde{\gamma}_g$ will differ from its bare counterpart, and will describe the theory on the physical scale and thus can be determined by measuring physical observables. Furthermore, given that for any flow time $\tau > 0$ the gauge field is automatically renormalised, it is expected that the appropriate value for the anisotropy parameter within the flow equation is in fact $\gamma_w = \tilde{\gamma}_g$. When flowing on an anisotropic lattice it is important that the appropriate anisotropy parameter is applied within the flow equation, $\rho_{i0} = \gamma_w^2$, such that the fields are averaged equally by the heat equation in all directions of Euclidean spacetime.

The equivalent formulas for the anisotropic case are given by;

$$E_{ss}(\tau) = \frac{1}{4}\sum_{x,i\neq j} F^2_{ij}(x,\tau), \tag{3.5}$$

for the spatial component of the action density, whereas for the temporal component it is;

$$E_{st}(\tau) = \frac{1}{2}\sum_{x,i} F^2_{i0}(x,\tau). \tag{3.6}$$

The expectation values of the spatial and temporal components of the action density are equal in physical units (i.e. in dimensionful form), and given that these operators are renormalised for $\tau > 0$, they must then provide a definition of the renormalised gauge anisotropy. Furthermore the components of the action density can be written in dimensionless form such that;

$$\begin{aligned} E_{ss}(\tau) &= \hat{E}_{ss}(\hat{\tau})a_s^{-4}, \\ E_{st}(\tau) &= \hat{E}_{st}(\hat{\tau})a_s^{-2}a_t^{-2}, \end{aligned} \tag{3.7}$$

where the length scale ω_0 and flowtime τ variables are also expressed in dimensionless form (or so called lattice units);

$$\begin{aligned} \tau &= \hat{\tau} a_s^2, \\ \omega_0 &= \hat{\omega}_0 a_s. \end{aligned} \tag{3.8}$$

The ratio of the expectation values for the action density can then be written into dimensionless form;

$$\frac{< E_{ss}(\tau) >}{< E_{st}(\tau) >} = \frac{< \hat{E}_{ss}(\hat{\tau}) a_s^{-4} >}{< \hat{E}_{st}(\hat{\tau}) a_s^{-2} a_t^{-2} >} = \frac{< \hat{E}_{ss}(\hat{\tau}) > a_s^{-2}}{< \hat{E}_{st}(\hat{\tau}) > a_t^{-2}} = \frac{< \hat{E}_{ss}(\hat{\tau}) >}{< \hat{E}_{st}(\hat{\tau}) >} \tilde{\gamma}_g^{-2} = 1, \tag{3.9}$$

where the first equality simply substitutes eq. (3.7), and the final equality comes from the fact that the spatial and temporal components are equal in physical units. It is then immediately apparent that the ratio of the action densities in dimensionless form, which is referred to as being in lattice units in [68], must relate to the renormalised gauge anisotropy via;

$$\frac{< \hat{E}_{ss}(\hat{\tau}) >}{< \hat{E}_{st}(\hat{\tau}) >} \stackrel{!}{=} \tilde{\gamma}_g^2, \tag{3.10}$$

where once again the substitution eq. (3.7) can be applied to obtain;

$$\frac{< a_s^4 E_{ss}(\tau) >}{< a_s^2 a_t^2 E_{st}(\tau) >} = \tilde{\gamma}_g^2, \tag{3.11}$$

as is given within the above cited paper.

However the scaling features of the derivatives of the field strength tensors (action density) are superior to the plain ratio, and are thus used instead [68]. The method for computing $\tilde{\gamma}_g$ is implemented by first selecting a value for γ_w, then calculating the action density as a function of flow time.

Subsequently the ratio of the derivatives of the action density, R_E, is computed;

$$R_E = \frac{\left[\hat{\tau} \frac{d}{d\hat{\tau}} \hat{\tau}^2 < \hat{E}_{ss}(\hat{\tau}) > \right]_{\hat{\tau}=\hat{\omega}_0^2}}{\left[\hat{\tau} \frac{d}{d\hat{\tau}} \hat{\tau}^2 < \hat{E}_{st}(\hat{\tau}) > \right]_{\hat{\tau}=\hat{\omega}_0^2}} = \tilde{\gamma}_g^2, \tag{3.12}$$

where the $\hat{\omega}_0$ scale setting condition is given as;

$$\left[\hat{\tau} \frac{d}{d\hat{\tau}} \hat{\tau}^2 < \hat{E}_{ss}(\hat{\tau}) > \right]_{\hat{\tau}=\hat{\omega}_0^2} = 0.15. \tag{3.13}$$

However, the computation of R_E itself requires the correct value of the renormalised gauge anisotropy within the flow equation eq. (3.2), and thus eq. (3.12) and eq. (3.13) are a pair of coupled equations for the unknowns $\tilde{\gamma}_g$ and $\hat{\omega}_0$. Thus in order to solve these equations and determine $\tilde{\gamma}_g$, the above process is performed for a range of γ_w^2 values until the following condition is met;

$$\frac{R_E(\gamma_w)}{\gamma_w^2} = 1, \tag{3.14}$$

at which point $\tilde{\gamma}_g = \gamma_w$, hence providing the renormalised gauge anisotropy $\tilde{\gamma}_g$. It is worth noting that typically the lattice Yang-Mills action takes the form;

$$\begin{aligned} E \propto& \beta E_{st} + \beta E_{ss}, \\ \hat{E} \propto& \beta \frac{a_s}{a_t} \hat{E}_{st} + \beta \frac{a_t}{a_s} \hat{E}_{ss}, \\ \propto& \beta \gamma_g \hat{E}_{st} + \beta \frac{1}{\gamma_g} \hat{E}_{ss}, \\ \propto& \beta^{(1)} \hat{E}_{st} + \beta^{(2)} \hat{E}_{ss}, \end{aligned} \tag{3.15}$$

where two distinct β values naturally arise for the anisotropic case. Such concerns do not factor into this computation as it is the action density being used, whereas the bare gauge anisotropy factors and beta factors only enter into the observable explicitly for the total action as outlined above.

In order to evolve the gauge fields through flowtime, the flow equation eq. (3.1) was solved using numerical integration with the third order Runge-Kutta integrator. Recasting the differential equation into the general form;

$$\partial_\tau V_\tau = Z(V_\tau) V_\tau, \tag{3.16}$$

and with the initial condition;

$$V(x, \mu, \tau = 0) = U(x, \mu), \tag{3.17}$$

the integration from flowtime τ to $\tau + \epsilon$ is given by;

$$\begin{aligned} X_0 =& V_\tau, \\ X_1 =& \exp\left\{ \frac{Z_0}{4} \right\} X_0, \\ X_2 =& \exp\left\{ \frac{8Z_1}{9} - \frac{17Z_0}{36} \right\} X_1, \\ V_{\tau+\epsilon} =& \exp\left\{ \frac{3Z_2}{4} - \frac{8Z_1}{9} + \frac{17Z_0}{36} \right\} X_2, \end{aligned} \tag{3.18}$$

where $Z_i \equiv \epsilon Z(X_i)$. The first part of the procedure is demonstrated by the original work from Fodor et al within fig. 3.1, which shows the determination of the $\hat{\tau} = \hat{\omega}_0^2$ scale as per eq. (3.13), along with both factors within R_E. The correct value of the flow anisotropy, where $\gamma_w = \tilde{\gamma}_g$, is given by the

value of γ_w for which the derivatives of both the spatial and temporal action density overlap at a value of 0.15. In practice however it is sufficient to determine the flowtime $\hat{\tau}$ for which eq. (3.13) is satisfied, for a range of flow anisotropy values γ_w. The second part of the procedure is then shown in fig. 3.2, whereby at the aforementioned flowtime the value of R_E has been determined and then plotted according to eq. (3.14). The desired value of γ_w is then obtained via interpolation, which is precisely that value for which the spatial and temporal derivatives of action density overlap at 0.15 in fig. 3.1. It should be reiterated that these computations are performed on the same ensemble, but each time with a different value of the flow anisotropy γ_w. This method for computing the renormalised gauge anisotropy is performed at zero temperature and is thus performed using the FASTSUM ensemble for which $N_t = 128$ and $N_s = 32$.

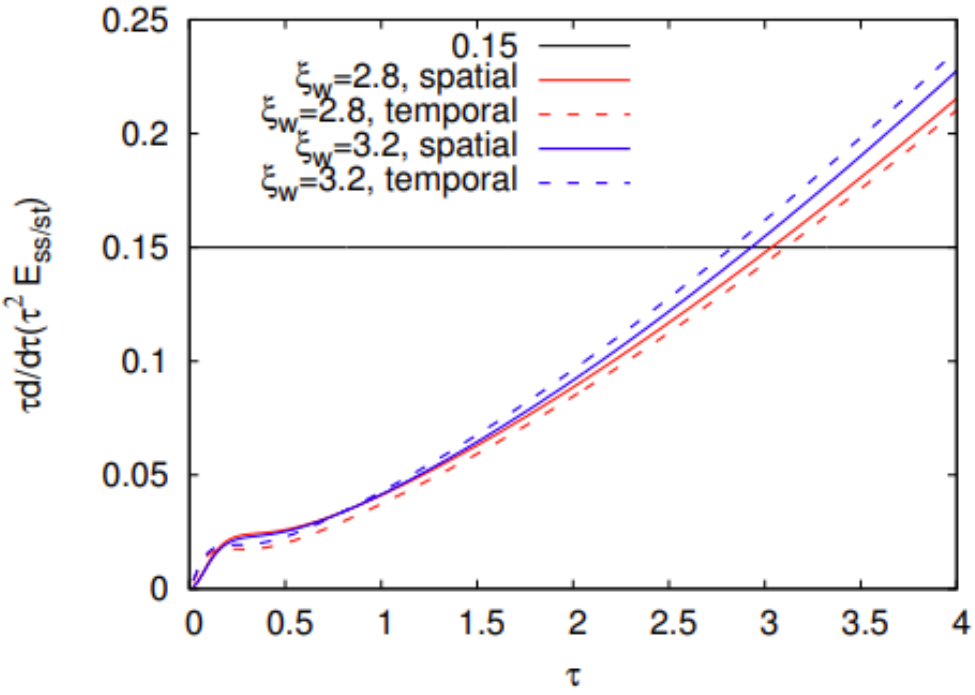

Fig. 3.1: Figure taken from [68]. The derivative of the action density is shown against the flowtime for two levels of anisotropy, $\xi_w = \{2.8, 3.2\}$, where a difference of notation is noted by $\xi_w \equiv \gamma_w$. The spatial and temporal components switch order for the two anisotropy values, indicating that the renormalised gauge anisotropy lies between these values. Moreover the identification of $\gamma_w = \tilde{\gamma}_g$ is made for that value of γ_w where the spatial and temporal components are equal at $\hat{\tau} = \hat{\omega}_0^2$.

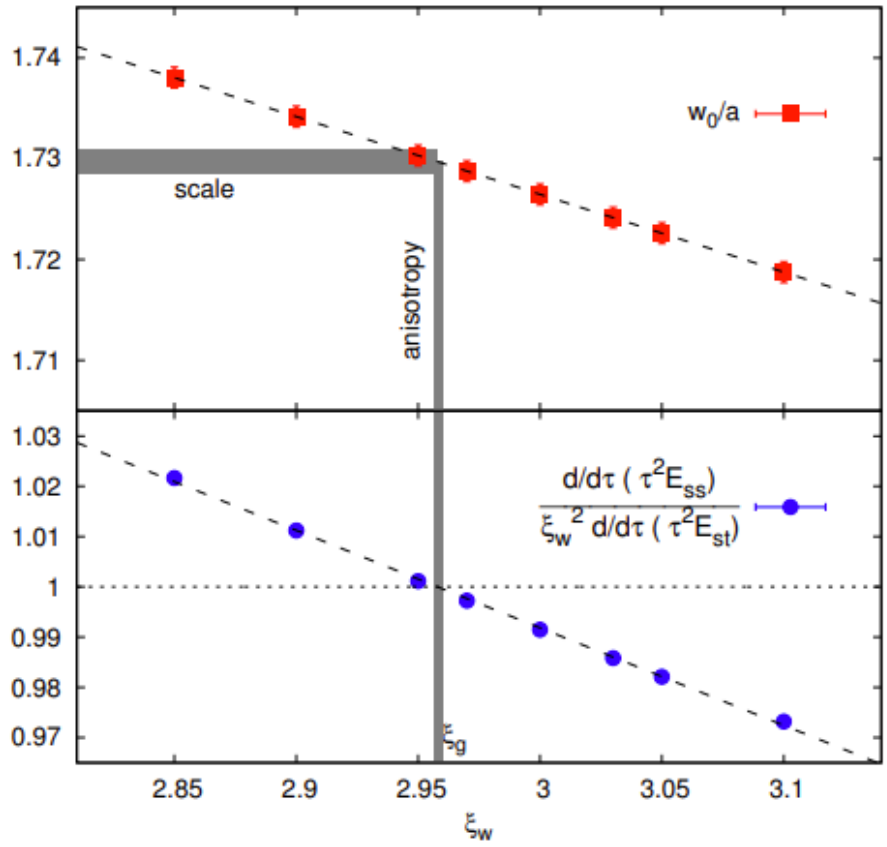

Fig. 3.2: Figure taken from [68]. The renormalised gauge anisotropy is determined using the Wilson flow, by determining the spatial $\hat{\omega}_0$ scale for various values of γ_w, and then determining the value of R_E at the point $\hat{\tau} = \hat{\omega}_0^2$. Within the lower panel the value of R_E/γ_w^2 is used on the vertical axis, such that condition eq. (3.14) is met at the unit value. The upper panel shows the interpolation of ω_0/a_s to the relevant point at $\gamma_w = \tilde{\gamma}_g$.

Numerical stability tests were performed for the N_t x $N_s^3 = 8$ x 32^3 ensemble, which are shown in fig. 3.3 to fig. 3.8 for several integrator step sizes ϵ and at several flow anisotropy values γ_w. The step size $\epsilon = 0.015$ which has been highlighted within the figures using a different marker, is shown to be stable for all values of flow anisotropy, and is thus used throughout this work. This value for the step size is chosen due to it being fast to use whilst being far away from any issues of instability which are present at larger step sizes. All errors are included and were computed using Jackknife error analysis, with typical results being of the order of 1%. The minor discrepancy between the different step sizes at low flow time is a consequence of the data points not being equally spaced for the different ϵ values, not due to a legitimate disagreement.

Numerical stability tests were also performed for the N_t x $N_s^3 = 128$ x 32^3 ensemble, which are shown in fig. 3.9 to fig. 3.14. Once again the step size $\epsilon = 0.015$ is stable for all cases of interest. It is therefore assumed that the same step size is stable for all intermediate values of flow anisotropy within the range $\gamma_w = 1.00 \rightarrow 3.65$. More specifically, as will be discussed in chapter 4, for each lattice there exists a maximum flow time that can be safely used before over-smearing occurs, according to eq. (4.41), with the values for each temperature being given in table 4.1. Accordingly the stability

of lattices $N_t = 8 \rightarrow 32$ and $N_t = 128$ were checked for $\epsilon = 0.015$ within fig. 3.15 and fig. 3.16 for $\gamma_w = 1.00$ and $\gamma_w = 3.65$ respectively, whereas the intermediate lattices from $N_t = 32 \rightarrow 128$ all have the same maximum safe flow time, and are thus assumed to be stable for $\epsilon = 0.015$ for all values of interest for γ_w.

All data for the N_t x $N_s^3 = 8$ x 32^3 ensemble at $\epsilon = 0.015$ are shown together within fig. 3.17, and likewise within fig. 3.18 for the N_t x $N_s^3 = 128$ x 32^3 ensemble data. As expected, the temporal components of the action density E_{st} are more strongly affected by the level of flow anisotropy applied than the spatial components E_{ss}. Interestingly the difference between E_{st} for the $\gamma_w = 1.00$ and $\gamma_w = 3.25$ data is stronger at higher temperature, whereas there is more significant spread within the range $\gamma_w = 3.25 \rightarrow 3.65$ at lower temperature.

The determination of the appropriate flow time for the $\hat{w}_0$ condition and the subsequent determination of the ratio R_E are shown for $\gamma_w = 3.65$ within fig. 3.19, with the data given in table 3.2. The determination of the spatial lattice spacing a_s and the renormalised gauge anisotropy $\tilde{\gamma}_g$ are then shown in fig. 3.20 with the data given in table 3.3, with the results compared to the known FASTSUM values given in table 3.1.

The value of the physical w_0 scale which was quoted above in relation to eq. (3.3) and determined in [56], has since been updated with a more precise value of $w_0 = 0.17236(29)(63)$ fm, which was computed within [69] and then used in [71]. This more recent value for the w_0 scale was used within this work. The errors quoted for this work were determined by using jackknife analysis directly on the end quantities a_s and $\tilde{\gamma}_g$. The error for a_s also included adding the output from this step in quadrature with the known error in w_0, the formula for which is given by;

$$\Delta a_s = a_s \sqrt{\left(\frac{\Delta \hat{w}_0}{\hat{w}_0}\right)^2 + \left(\frac{\Delta w_0}{w_0}\right)^2}, \tag{3.19}$$

where the error for $\hat{w}_0$ was determined by jackknife analysis, with the final value with statistical error being $\hat{w}_0 = 1.41954(2)$. The earlier computation of w_0 within [56] demonstrated a difference of approximately 0.003 for the physical pion mass and that used for the FASTSUM Gen2l configurations which are used in this work. A similar mass dependence is not clearly shown for the updated computation within [69] and thus the difference is assumed to be the same. The systematic error for a_s was thus determined by repeating the analysis with values of $w_0 = 0.16936 \rightarrow 0.17236$, with the error being taken as the standard deviation of the resultant uniform distribution.

The discrepancy between the known FASTSUM value for $\tilde{\gamma}_f$ and the value for $\tilde{\gamma}_g$ obtained in this work is equal to 1.13% of the known value for $\tilde{\gamma}_f$, with a discrepancy of 8.32% for a_s. The known values for $\tilde{\gamma}_f$ and a_s were obtained within [47, 48], with the $\tilde{\gamma}_f$ determination using fermion dispersion methods and a_t using a baryon mass fit, with a_s then being taken as the product of $\tilde{\gamma}_f$ and a_t. The values from this work utilised the gradient flow on gauge fields, and thus given the different nature of the methods used, the difference of 1.13% for $\tilde{\gamma}_g$ and 8.32% for a_s is considered to represent an acceptable agreement. This level of discrepancy for a_s is within the expected level of agreement when

comparing fermion and gauge estimations, which typically differ by $5-10\%$.

	FASTSUM		This Work
a_s	0.11208(31)	a_s	0.1214(5)(6)
$\tilde{\gamma}_f$	3.453(6)	$\tilde{\gamma}_g$	3.41408(8)

Table. 3.1: Comparison of the known FASTSUM values and the values for this validation check of the anisotropic flow, for the spatial lattice spacing a_s and the renormalised anisotropy ($\tilde{\gamma}_g$ vs $\tilde{\gamma}_f$). This work was performed using the N_t x $N_s^3 = 128$ x 32^3 ensemble with 990 configurations. This is for the Gen2L data, the full parameter list for which can be found within table 2.6. The error on $\tilde{\gamma}_g$ for this work is statistical, with the first and second errors on a_s being statistical and systematic respectively.

The action density output from the OpenQCD-FASTSUM code is also plotted against that from the Borsanyi et al code[1] for the FASTSUM Gen2L configurations, within fig. 3.21, with the errors being computed once again by jackknife analysis.

In this chapter the implementation of the anisotropic Wilson flow was validated, successfully reproducing the known FASTSUM values to within an acceptable margin for the spatial lattice spacing a_s, and the renormalised anisotropy ($\tilde{\gamma}_g$ vs $\tilde{\gamma}_f$), using the method introduced within [68]. The action density output from the OpenQCD-FASTSUM code also showed good agreement from the code of Borsanyi et al, both using the FASTSUM Gen2L configurations. The integrator step size $\epsilon = 0.015$ was shown to be stable across all parameters of interest and is thus used throughout the remainder of this work. The next chapter will introduce the background content for the main work of this thesis, which is the determination of thermodynamic properties within $N_f = 2+1$ QCD, and will then present the corresponding results.

[1]This code can be found on the arXiv page for the work presented within [56].

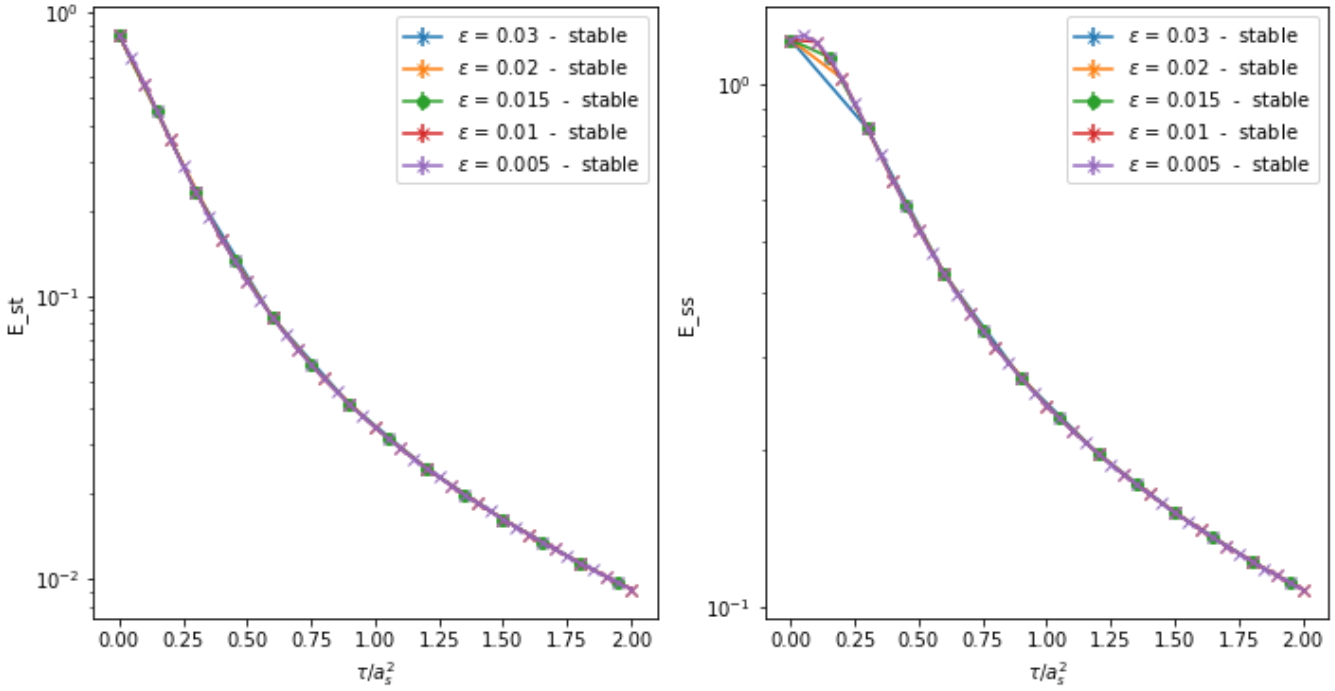

Fig. 3.3: $< \hat{E}_{st}(\hat{\tau}) >$ and $< \hat{E}_{ss}(\hat{\tau}) >$ vs $\hat{\tau}$ for various integrator step sizes ϵ (eps) for $\gamma_w = 1.00$. This data is for the N_t x $N_s^3 = 8$ x 32^3 ensemble.

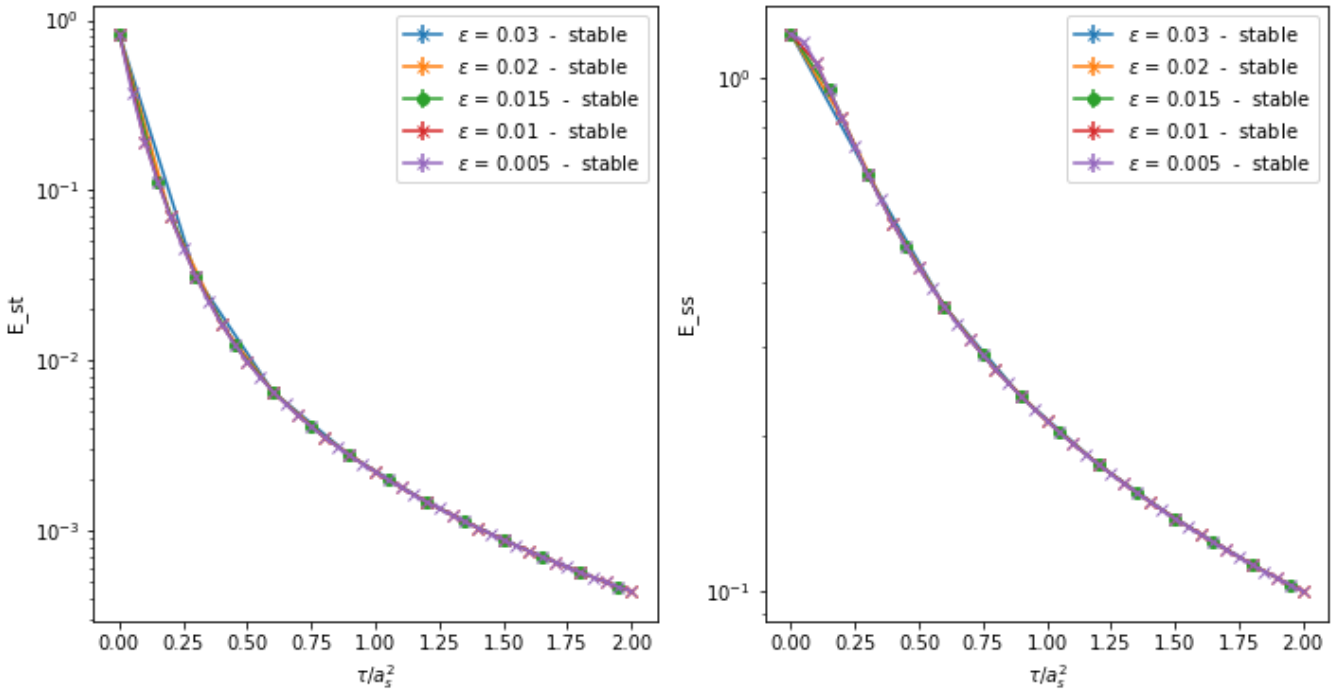

Fig. 3.4: $< \hat{E}_{st}(\hat{\tau}) >$ and $< \hat{E}_{ss}(\hat{\tau}) >$ vs $\hat{\tau}$ for various integrator step sizes ϵ (eps) for $\gamma_w = 3.25$. This data is for the N_t x $N_s^3 = 8$ x 32^3 ensemble.

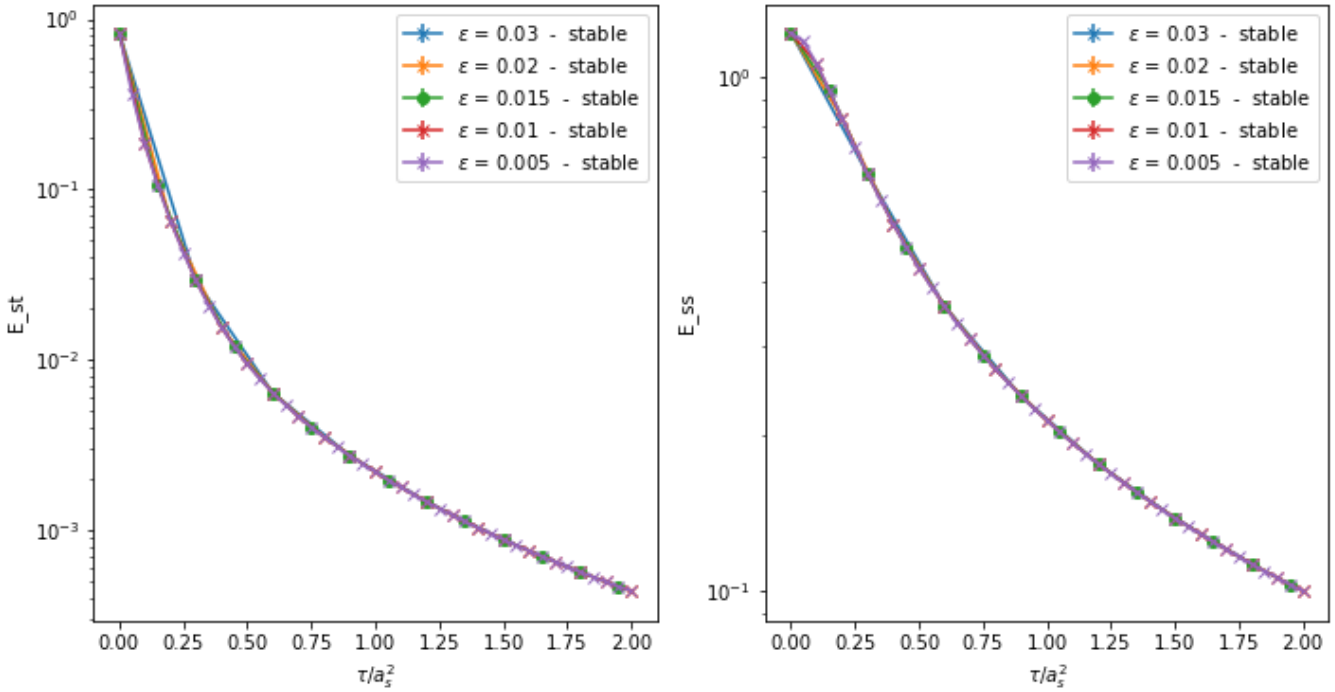

Fig. 3.5: $< \hat{E}_{st}(\hat{\tau}) >$ and $< \hat{E}_{ss}(\hat{\tau}) >$ vs $\hat{\tau}$ for various integrator step sizes ϵ (eps) for $\gamma_w = 3.35$. This data is for the N_t x $N_s^3 = 8$ x 32^3 ensemble.

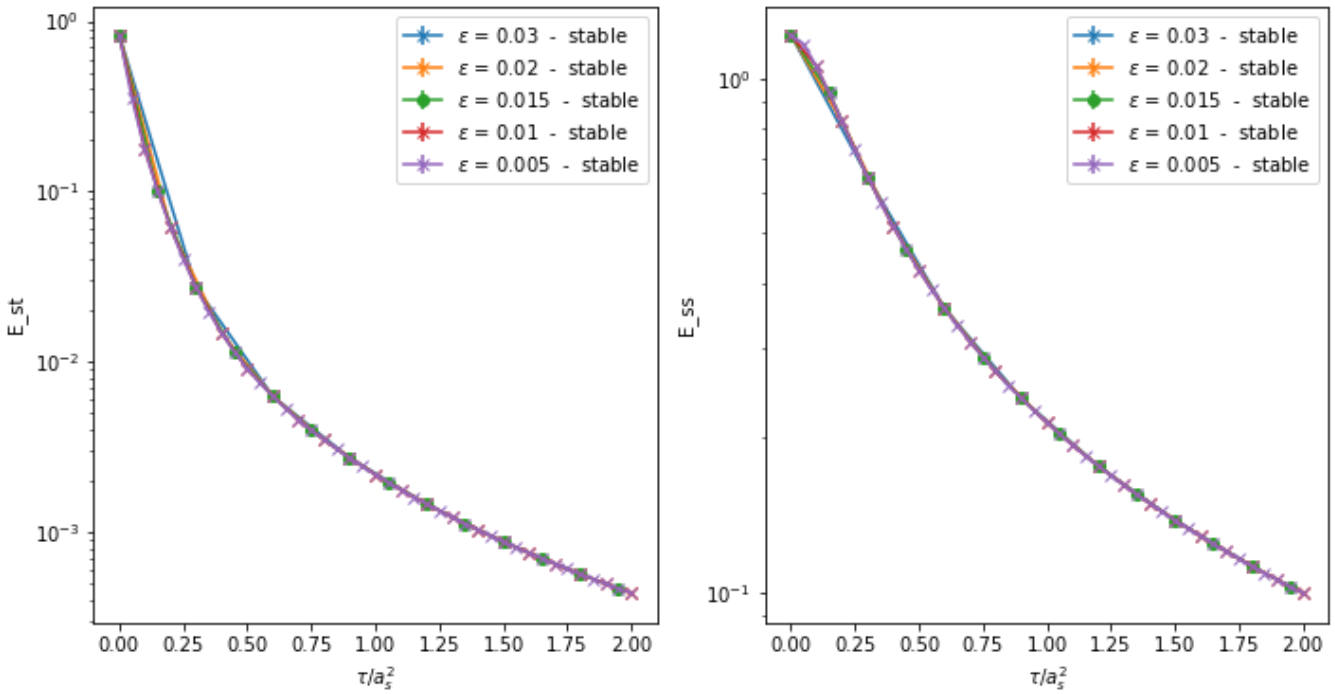

Fig. 3.6: $< \hat{E}_{st}(\hat{\tau}) >$ and $< \hat{E}_{ss}(\hat{\tau}) >$ vs $\hat{\tau}$ for various integrator step sizes ϵ (eps) for $\gamma_w = 3.45$. This data is for the N_t x $N_s^3 = 8$ x 32^3 ensemble.

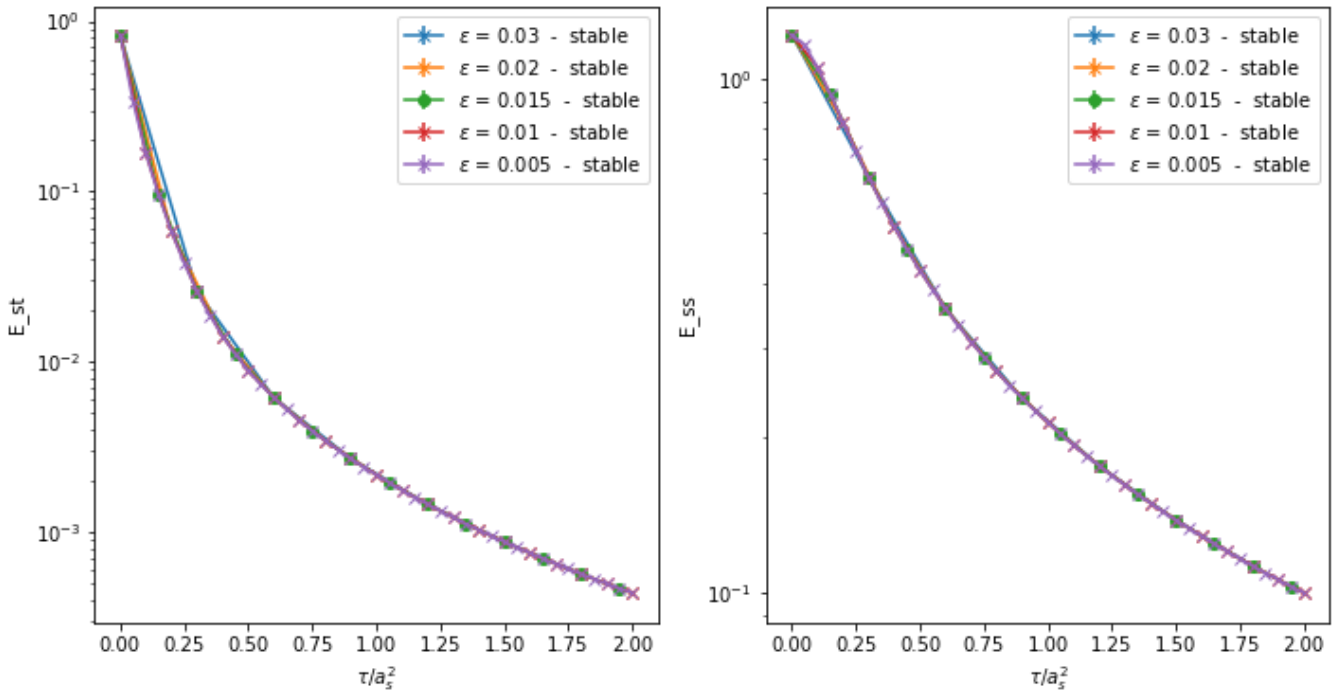

Fig. 3.7: $< \hat{E}_{st}(\hat{\tau}) >$ and $< \hat{E}_{ss}(\hat{\tau}) >$ vs $\hat{\tau}$ for various integrator step sizes ϵ (eps) for $\gamma_w = 3.55$. This data is for the N_t x $N_s^3 = 8$ x 32^3 ensemble.

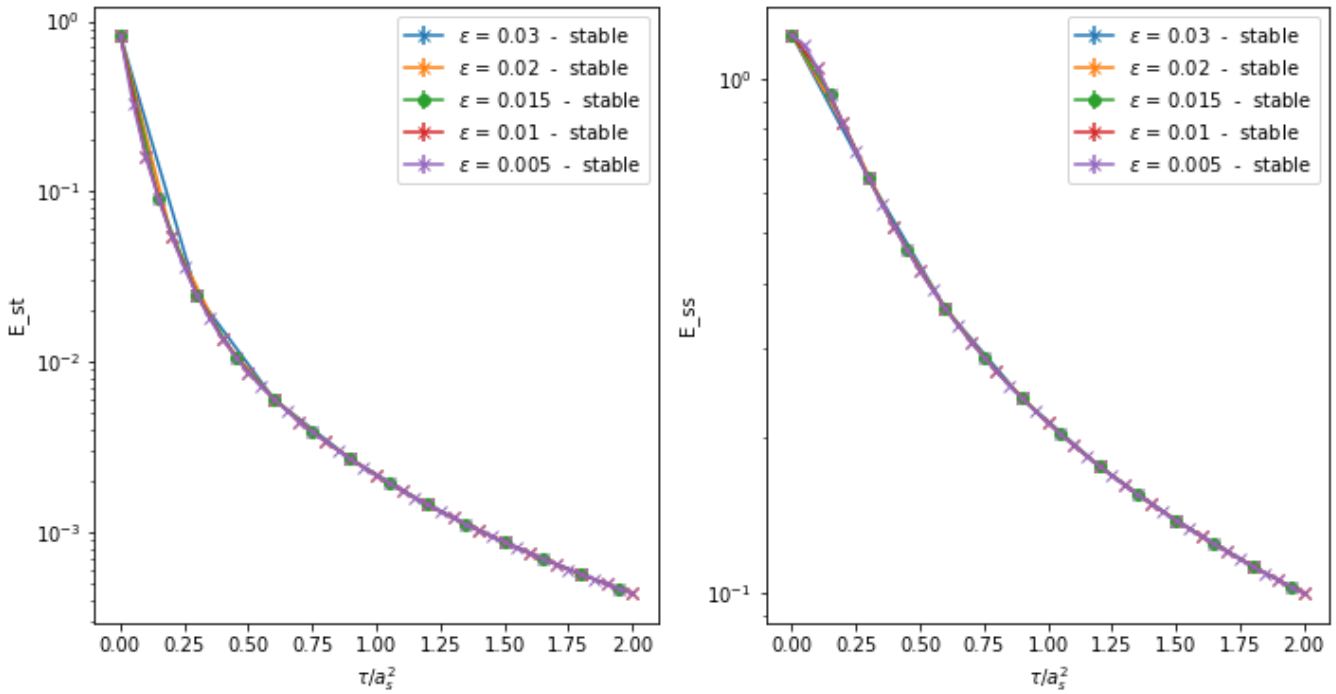

Fig. 3.8: $< \hat{E}_{st}(\hat{\tau}) >$ and $< \hat{E}_{ss}(\hat{\tau}) >$ vs $\hat{\tau}$ for various integrator step sizes ϵ (eps) for $\gamma_w = 3.65$. This data is for the N_t x $N_s^3 = 8$ x 32^3 ensemble.

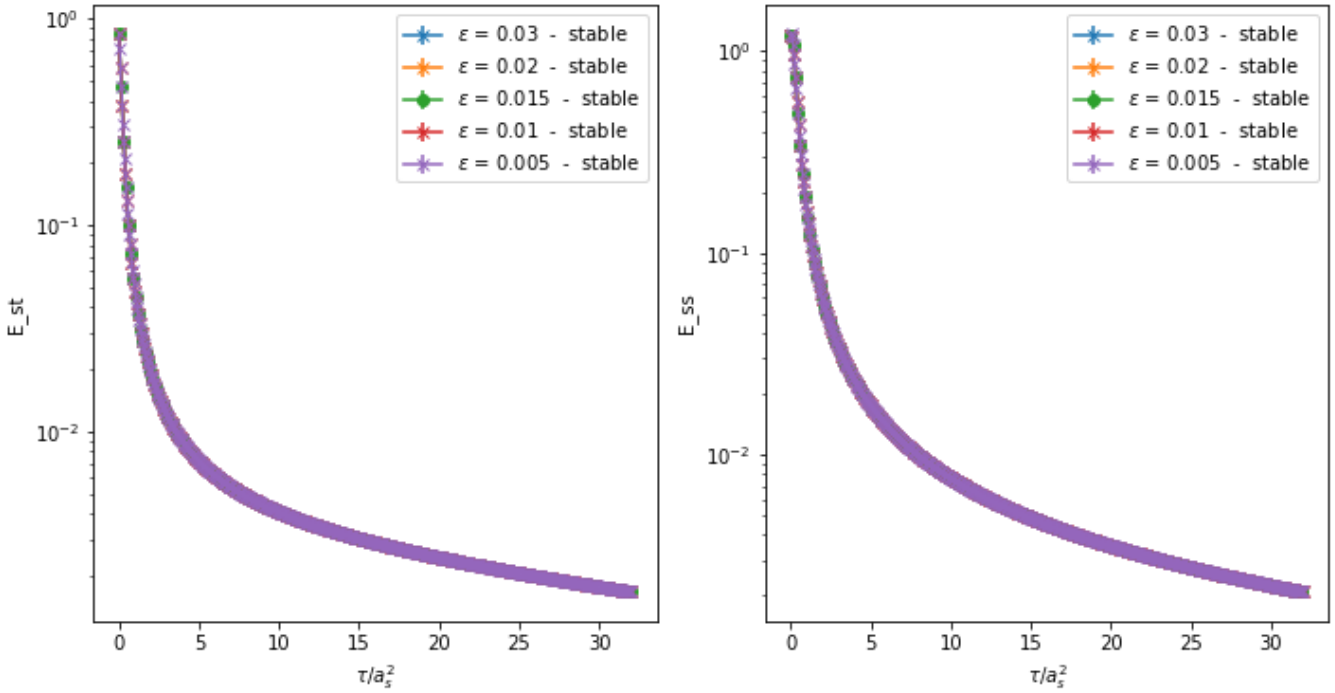

Fig. 3.9: $< \hat{E}_{st}(\hat{\tau}) >$ and $< \hat{E}_{ss}(\hat{\tau}) >$ vs $\hat{\tau}$ for various integrator step sizes ϵ (eps) for $\gamma_w = 1.00$. This data is for the N_t x $N_s^3 = 128$ x 32^3 ensemble.

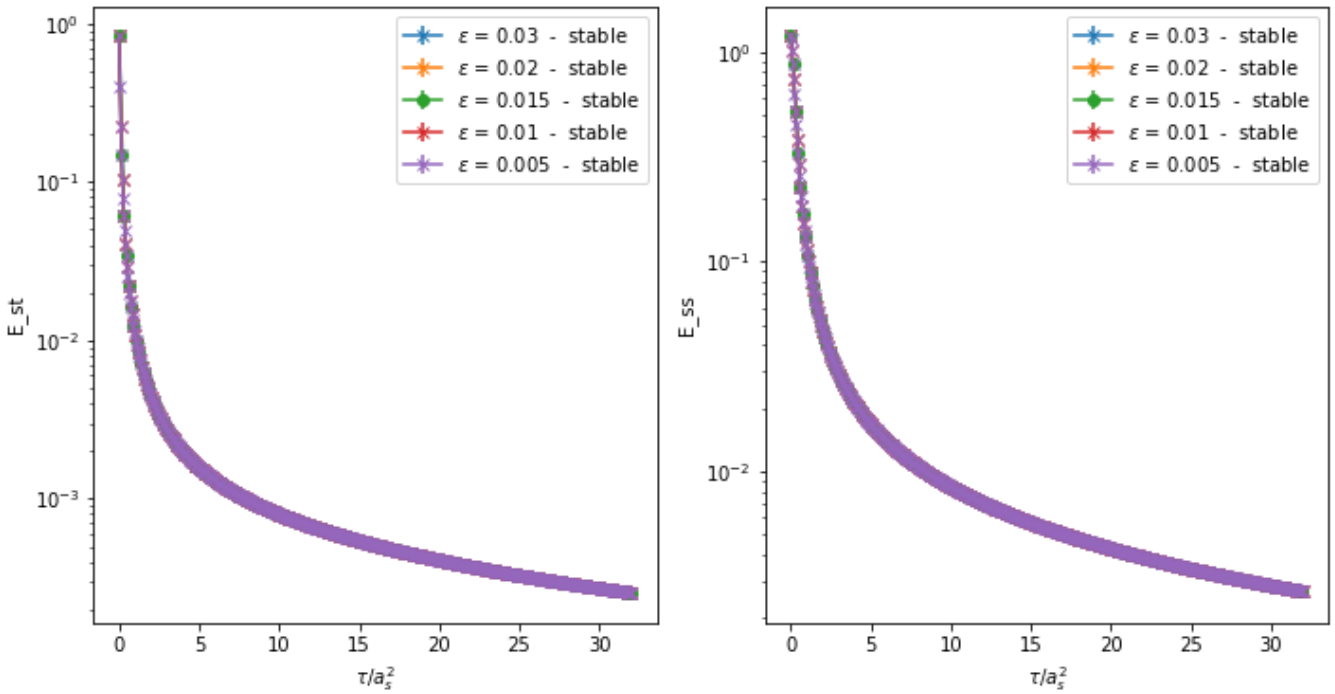

Fig. 3.10: $< \hat{E}_{st}(\hat{\tau}) >$ and $< \hat{E}_{ss}(\hat{\tau}) >$ vs $\hat{\tau}$ for various integrator step sizes ϵ (eps) for $\gamma_w = 3.25$. This data is for the N_t x $N_s^3 = 128$ x 32^3 ensemble.

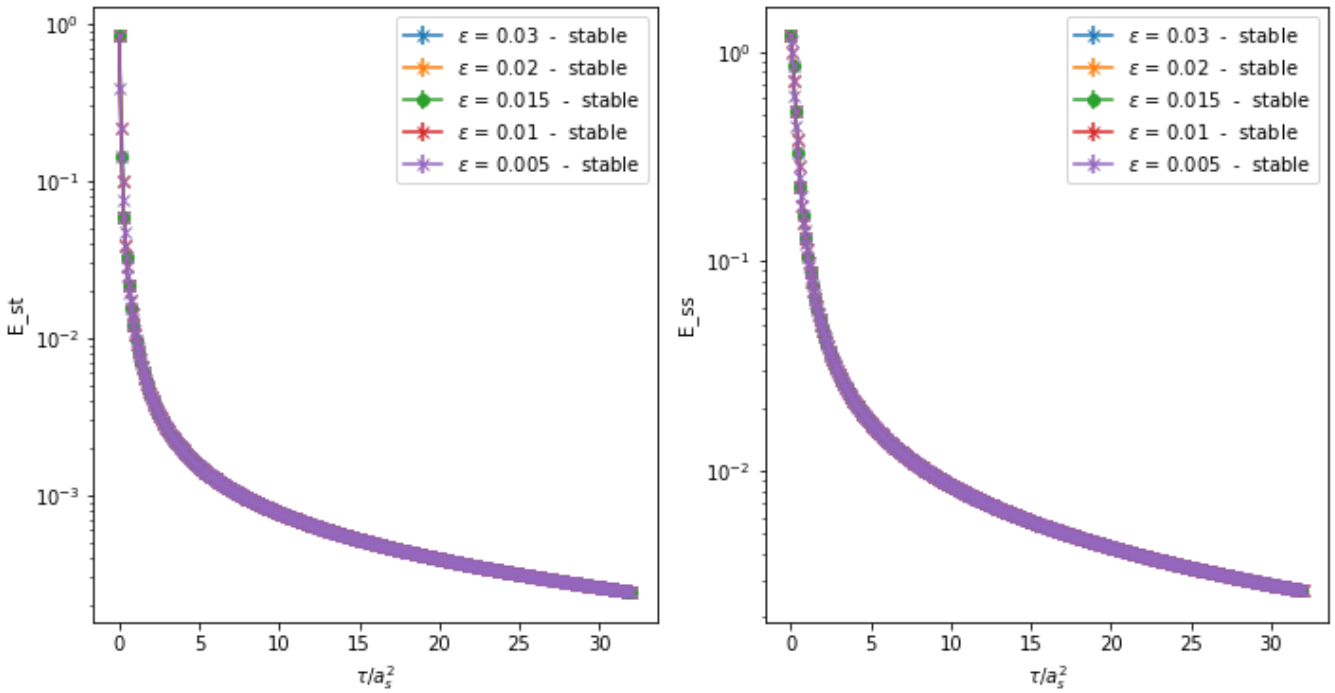

Fig. 3.11: $< \hat{E}_{st}(\hat{\tau}) >$ and $< \hat{E}_{ss}(\hat{\tau}) >$ vs $\hat{\tau}$ for various integrator step sizes ϵ (eps) for $\gamma_w = 3.35$. This data is for the N_t x $N_s^3 = 128$ x 32^3 ensemble.

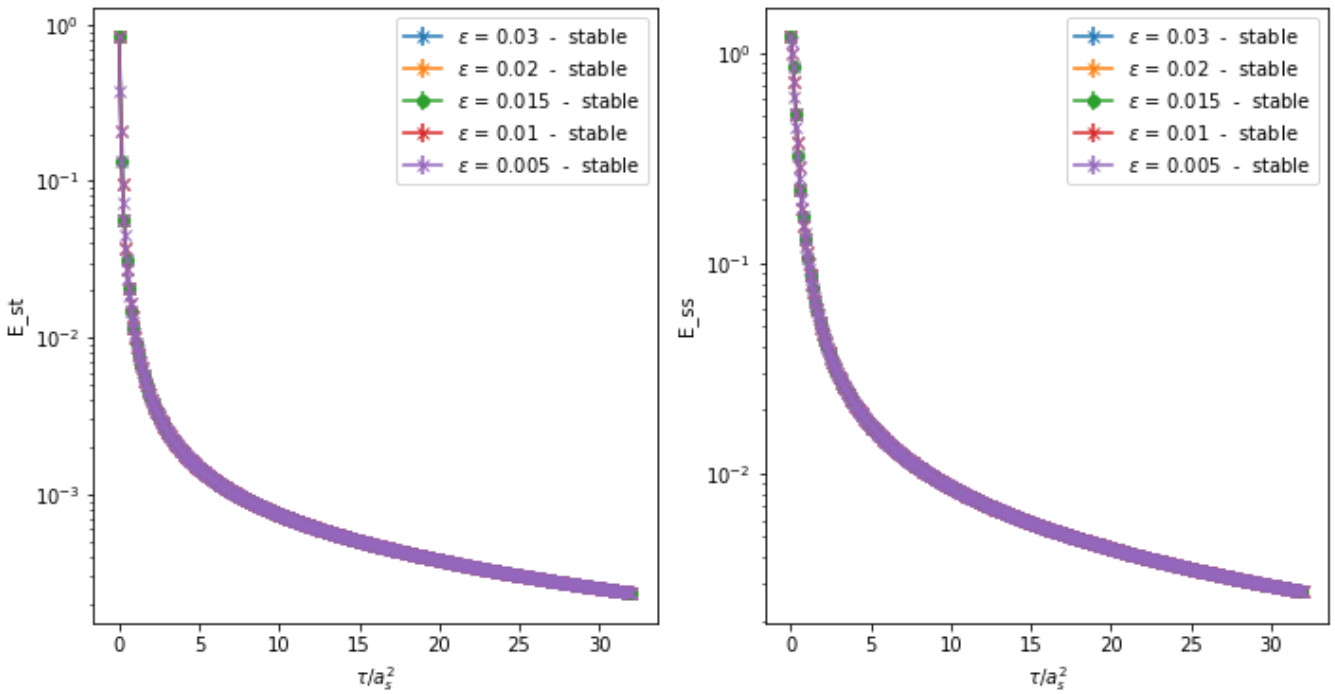

Fig. 3.12: $< \hat{E}_{st}(\hat{\tau}) >$ and $< \hat{E}_{ss}(\hat{\tau}) >$ vs $\hat{\tau}$ for various integrator step sizes ϵ (eps) for $\gamma_w = 3.45$. This data is for the N_t x $N_s^3 = 128$ x 32^3 ensemble.

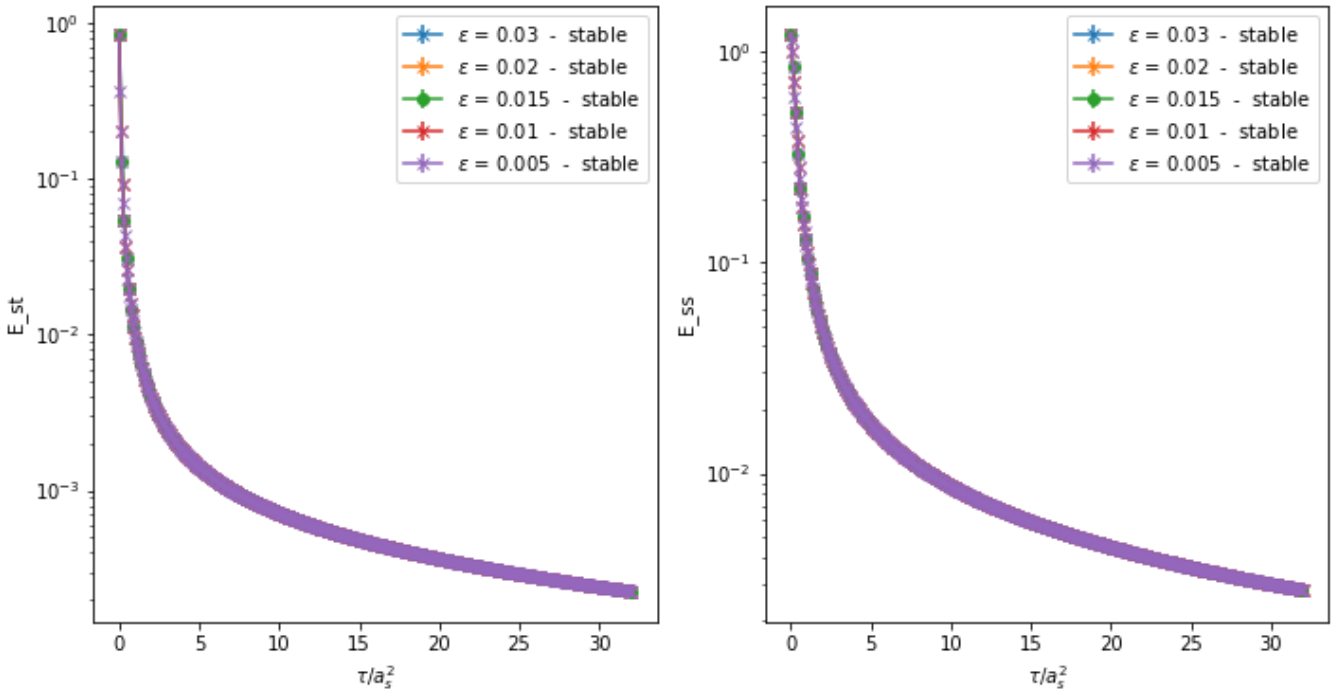

Fig. 3.13: $< \hat{E}_{st}(\hat{\tau}) >$ and $< \hat{E}_{ss}(\hat{\tau}) >$ vs $\hat{\tau}$ for various integrator step sizes ϵ (eps) for $\gamma_w = 3.55$. This data is for the N_t x $N_s^3 = 128$ x 32^3 ensemble.

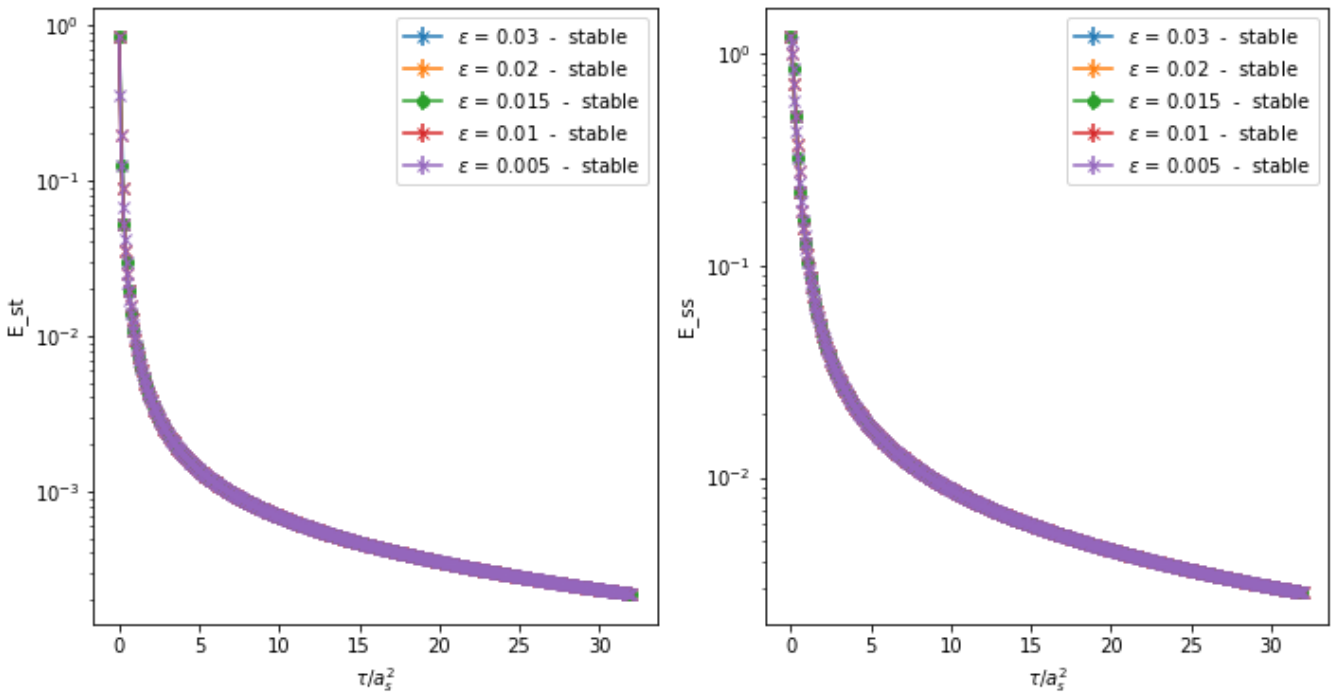

Fig. 3.14: $< \hat{E}_{st}(\hat{\tau}) >$ and $< \hat{E}_{ss}(\hat{\tau}) >$ vs $\hat{\tau}$ for various integrator step sizes ϵ (eps) for $\gamma_w = 3.65$. This data is for the N_t x $N_s^3 = 128$ x 32^3 ensemble.

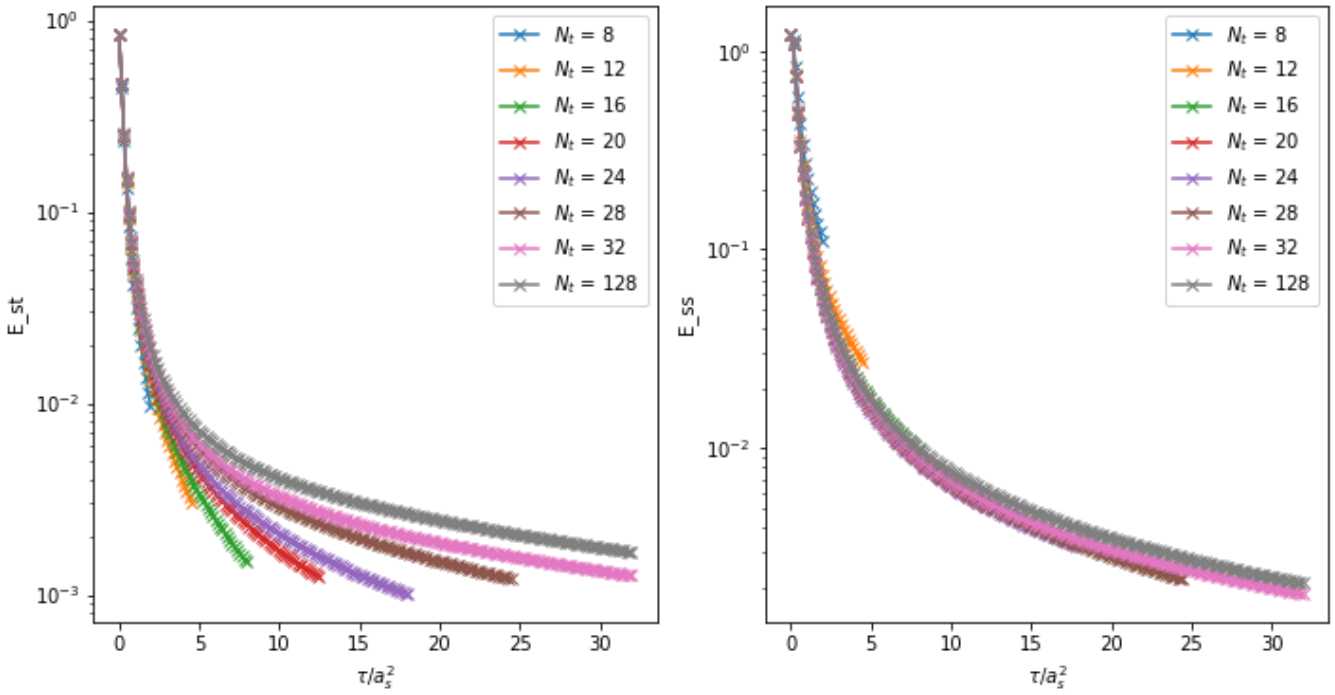

Fig. 3.15: $< \hat{E}_{st}(\hat{\tau}) >$ and $< \hat{E}_{ss}(\hat{\tau}) >$ vs $\hat{\tau}$ for integrator step size $\epsilon = 0.015$ and $\gamma_w = 1.00$, at multiple temperatures.

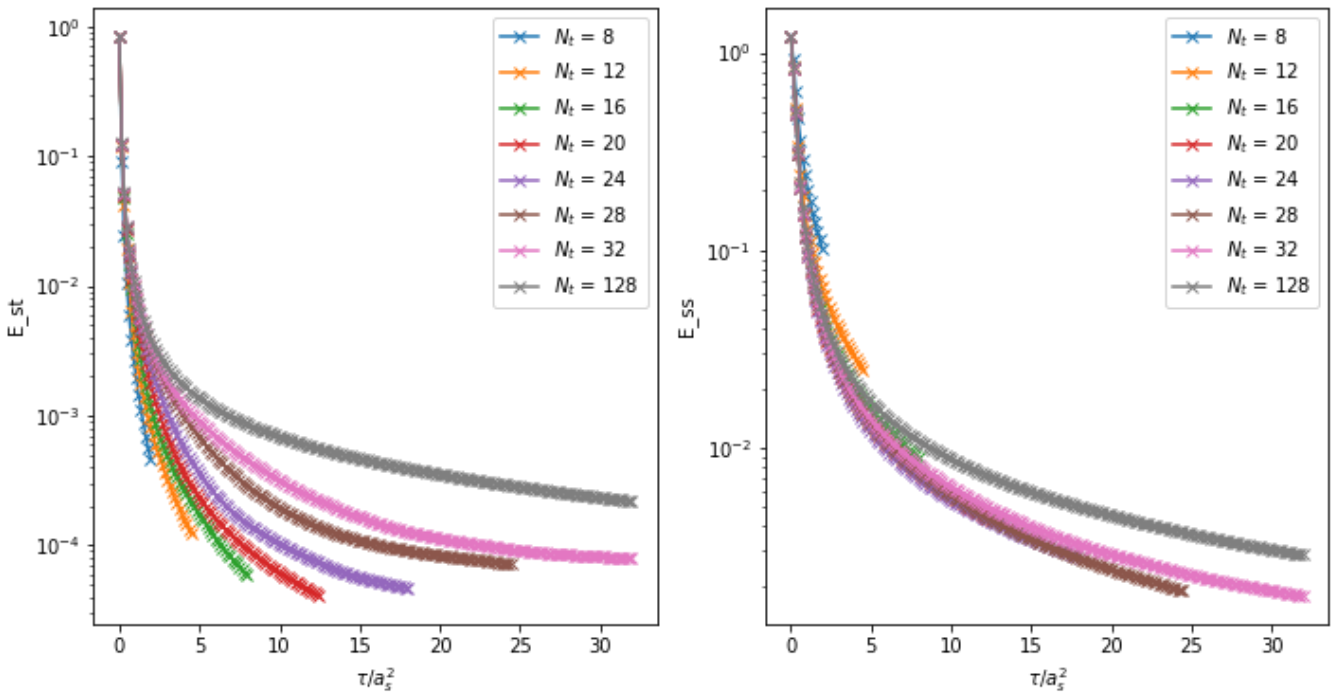

Fig. 3.16: $< \hat{E}_{st}(\hat{\tau}) >$ and $< \hat{E}_{ss}(\hat{\tau}) >$ vs $\hat{\tau}$ for integrator step size $\epsilon = 0.015$ and $\gamma_w = 3.65$, at multiple temperatures.

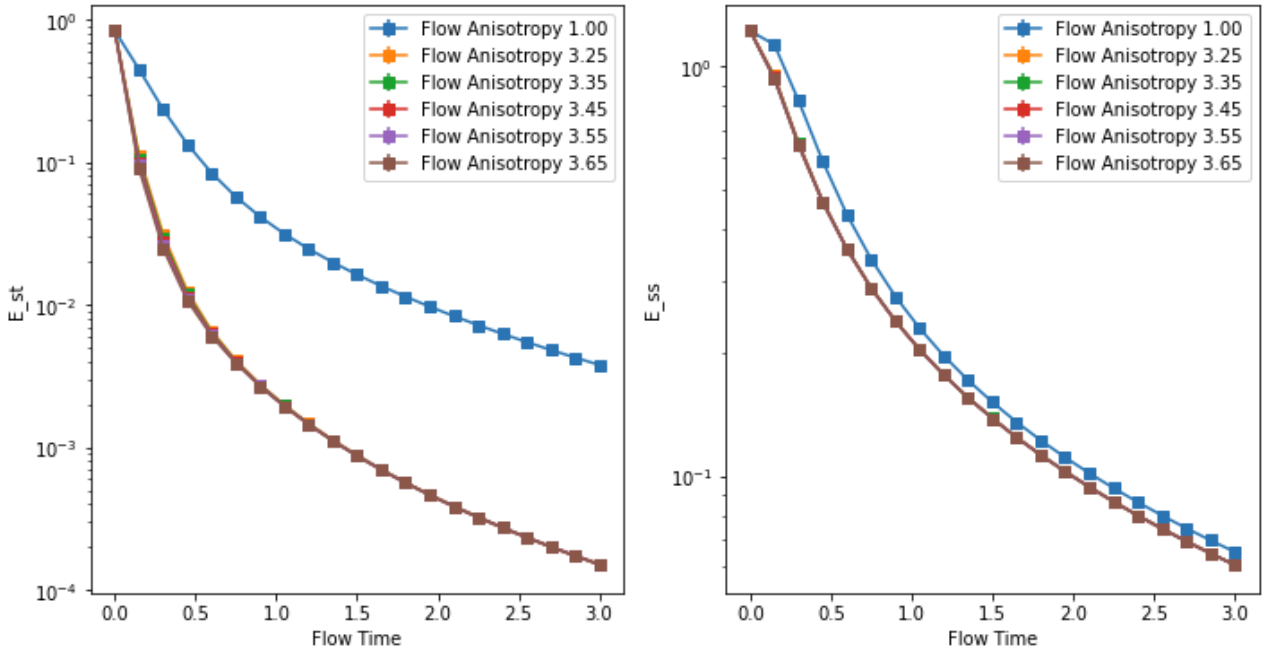

Fig. 3.17: $< \hat{E}_{st}(\hat{\tau}) >$ and $< \hat{E}_{ss}(\hat{\tau}) >$ vs $\hat{\tau}$ for integrator step size $\epsilon = 0.015$ and $N_t = 8$, at multiple values of flow anisotropy γ_w.

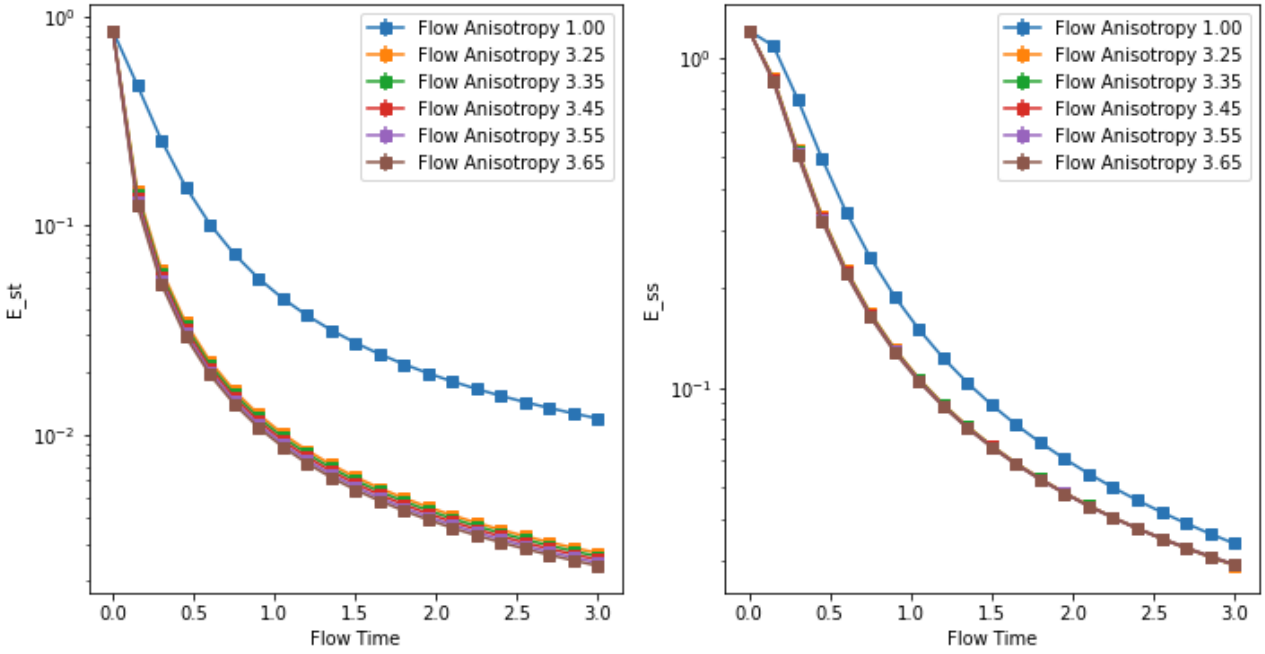

Fig. 3.18: $< \hat{E}_{st}(\hat{\tau}) >$ and $< \hat{E}_{ss}(\hat{\tau}) >$ vs $\hat{\tau}$ for integrator step size $\epsilon = 0.015$ and $N_t = 128$, at multiple values of flow anisotropy γ_w.

$\hat{\tau}$	R_E Numerator	R_E Denominator	$\hat{\tau}$	R_E Numerator	R_E Denominator
0.06	0.0066844	0.00115790	1.56	0.1158547	0.00901525
0.12	0.0207904	0.00217884	1.62	0.1205829	0.00938432
0.18	0.0336306	0.00263413	1.68	0.1253556	0.00975613
0.24	0.0417861	0.00284951	1.74	0.1301703	0.01013062
0.3	0.0458824	0.00296539	1.8	0.1350254	0.01050772
0.36	0.0477051	0.00306197	1.86	0.1399196	0.01088736
0.42	0.0487052	0.00317966	1.92	0.1448516	0.01126949
0.48	0.0497138	0.00333376	1.98	0.1498205	0.01165406
0.54	0.0511004	0.00352588	2.04	0.1548255	0.01204104
0.6	0.0529744	0.00375160	2.1	0.1598657	0.01243041
0.66	0.0553233	0.00400480	2.16	0.1649404	0.01282212
0.72	0.0580885	0.00427962	2.22	0.1700489	0.01321613
0.78	0.0612014	0.00457122	2.28	0.1751902	0.01361239
0.84	0.0645984	0.00487586	2.34	0.1803633	0.01401084
0.9	0.0682261	0.00519078	2.4	0.1855673	0.01441142
0.96	0.0720416	0.00551398	2.46	0.1908014	0.01481406
1.02	0.0760113	0.00584400	2.52	0.1960649	0.01521869
1.08	0.0801095	0.00617982	2.58	0.2013573	0.01562525
1.14	0.0843161	0.00652069	2.64	0.2066778	0.01603370
1.2	0.0886158	0.00686607	2.7	0.2120258	0.01644402
1.26	0.0929967	0.00721556	2.76	0.2174007	0.01685619
1.32	0.0974495	0.00756884	2.82	0.2228022	0.01727021
1.38	0.1019669	0.00792565	2.88	0.2282297	0.01768603
1.44	0.1065432	0.00828578	2.94	0.2336825	0.01810361
1.5	0.1111737	0.00864903	-	-	-

Table. 3.2: The data associated with fig. 3.19, which was computed for $\gamma_w = 3.65$. Note that the error for both a_s and $\tilde{\gamma}_g$ were computed via jackknife analysis on these final quantities, not at the level of the components of R_E or $\hat{E}(\hat{\tau})$, thus no error is quoted here for these intermediate quantities.

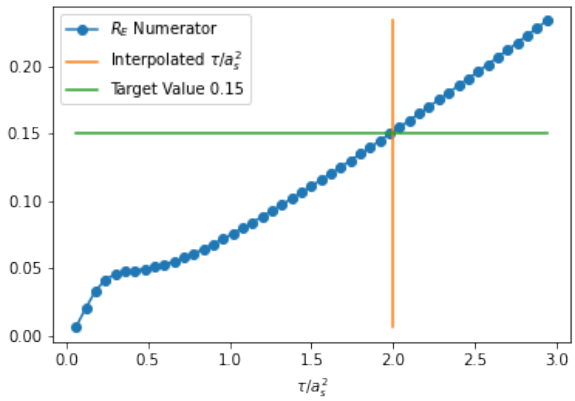

(a) Determination of the target flow time using $\left[\hat{\tau}\frac{d}{d\hat{\tau}}\hat{\tau}^2 < \hat{E}_{ss}(\hat{\tau}) > \right]_{\hat{\tau}=\hat{\omega}_0^2} = 0.15$.

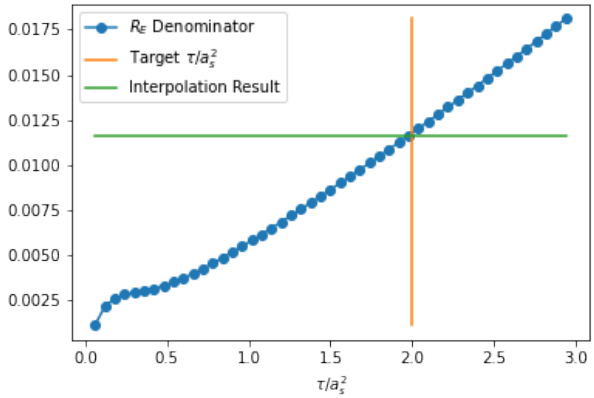

(b) Interpolation of $\left[\hat{\tau}\frac{d}{d\hat{\tau}}\hat{\tau}^2 < \hat{E}_{st}(\hat{\tau}) > \right]_{\hat{\tau}=\hat{\omega}_0^2}$ for target flow time $\hat{\tau}$.

Fig. 3.19: This data is for the N_t x N_s^3 = 128 x 32^3 ensemble, with an integrator step size of $\epsilon = 0.015$, using 990 configurations and with $\gamma_w = 3.65$.

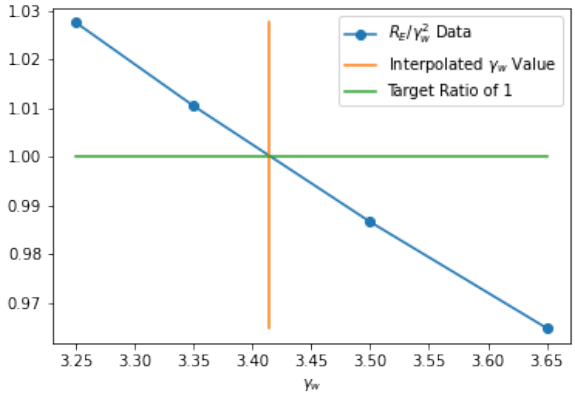

(a) Interpolation of the flow anisotropy γ_w which corresponds to the renormalised gauge anisotropy $\tilde{\gamma}_g$.

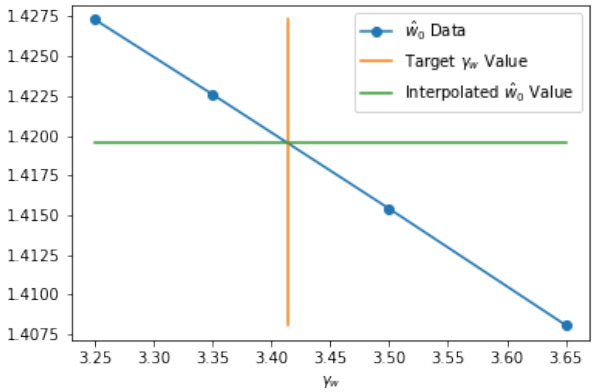

(b) Interpolation of the $\hat{w}_0$ scale, determined at the flow anisotropy value $\gamma_w = \tilde{\gamma}_g$.

Fig. 3.20: This data is for the N_t x N_s^3 = 128 x 32^3 ensemble, with an integrator step size of $\epsilon = 0.015$, using 990 configurations.

γ_w	R_E/γ_w^2	$\hat{w}_0$
3.25	1.0276	1.4273
3.35	1.0104	1.4226
3.5	0.9866	1.4154
3.65	0.9648	1.4081

Table. 3.3: The data associated with fig. 3.20. The determination of a_s involved determining the $\hat{w}_0$ value for each γ_w as shown in eq. (3.13) and presented here within this table. The $\hat{w}_0$ value for the renormalised gauge anisotropy where $\gamma_w = \tilde{\gamma}_g$ is then interpolated from this data. This is repeated for each jackknife re-sample and the final $\hat{w}_0$ with statistical error is thus determined, and used within the Δa_s computation shown in eq. (3.19). Thus at no point is there an error directly computed for the actual data points $\hat{w}_0$ given in this table, and hence they are quoted here without an associated error. Likewise the error on the final renormalised gauge anisotropy, $\Delta\tilde{\gamma}_g$, was determined by jackknife analysis, not the intermediate data presented within this table and thus no error is quoted here for R_E/γ_w^2.

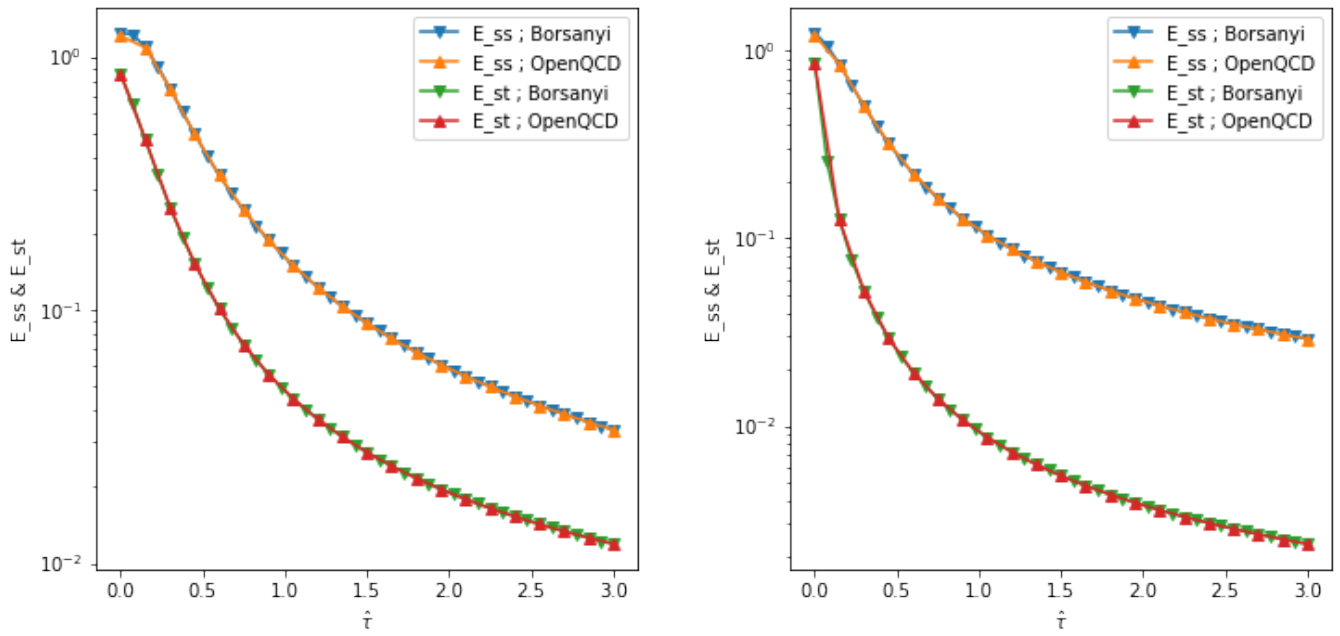

(a) $\gamma_w = 1.00$. **(b)** $\gamma_w = 3.65$.

Fig. 3.21: Comparison of the output of the code, in this case the action density E_{ss} and E_{st} as a function of flow time $\hat{\tau}$, from Borsanyi et al, and the OpenQCD-FASTSUM code. This data is for the N_t x $N_s^3 = 128$ x 32^3 ensemble, with an integrator step size of $\epsilon = 0.015$.

Chapter 4

Energy-Momentum Tensor and Thermodynamics

4.1 Equation of State

As was mentioned within the introduction there exist several methods for attempting to obtain thermodynamic quantities within lattice QCD, namely the derivative method and the integral method. Those methods are briefly outlined below, followed by a discussion of constructing the lattice energy-momentum tensor using gradient flow. Present results from the expectation value of the energy-momentum tensor are then discussed along with appropriate comparison to those results from the literature.

4.1.1 Derivative Method

It was previously stated within section 2.3 that the thermodynamic quantities could not be computed by direct access of the partition function. However the partition function can already be related to the action $-T \ln Z = S = S_F + S_G$, as was seen previously in eq. (2.28). The energy density and pressure are defined in relation to the partition function via [70];

$$\epsilon(T) = \frac{-1}{V} \frac{\partial \ln Z}{\partial (1/T)}\bigg|_V = \frac{-\xi}{N_s^3 N_t a_s^3 a_t} \left\langle \frac{\partial S}{\partial \gamma_g}\bigg|_{a_s} \right\rangle , \tag{4.1}$$

$$p(T) = T \frac{\partial \ln Z}{\partial V}\bigg|_T = \frac{-a_s}{3 N_s^3 N_t a_s^3 a_t} \left\langle \frac{\partial S}{\partial a_s}\bigg|_{a_t} \right\rangle , \tag{4.2}$$

where γ_g is again the bare gauge anisotropy, and the partition function has been substituted for the action S, factors of lattice spacing and the spatial volume $V = N_s^3 a_s^3$. The action can then be made explicit which will result in factors of the form;

$$\frac{\partial\beta}{\partial V} \; ; \; \frac{\partial\gamma_g}{\partial V}. \tag{4.3}$$

These partial derivatives are known as Karsch coefficients, named after the person who initially attempted to compute them perturbatively [72]. The temperature on the lattice is controlled by the following equation;

$$T = \frac{1}{N_t a_t}, \tag{4.4}$$

where as usual N_t is the number of lattice points in the temporal direction, and a_t is the temporal lattice spacing. Scanning various temperatures by holding N_t fixed and varying a_t is known as the fixed-N_t approach. In order to relieve physical observables of their ultraviolet divergences, it is often the case that a vacuum expectation value (VEV) will be subtracted from the determined value of the observable irrespective of the non-zero temperature at which it was computed. This VEV amounts to the value of that same observable at zero temperature. The fixed-N_t approach involves varying the lattice spacing a_t and thus each temperature requires a separate set of zero-temperature configurations in order to accommodate for the different renormalisation at each scale a_t. Consequently the fixed-N_t approach can be rather computationally expensive.

Alternatively the temperature may be scanned by varying N_t whilst holding a_t constant, which is hence known as the fixed-scale approach. This approach only contains a single value of lattice spacing a_t and thus requires only a single set of zero temperature configurations, and is free of the associated complexities of ensuring that a constant line of physics is adhered to. On the other hand, care must be taken to wisely select the initial value of a_t, and unlike with the fixed-N_t approach the temperature can only be scanned in discrete steps rather than continuously. Likewise, due to the small number of lattice points in the temporal direction at high temperature, lattice artifacts, or lattice volume effects, may become problematic.

In this way the Karsch coefficients can be studied non-perturbatively by observing the manner in which the parameters of the action β, γ_g depend on the microscopic quantities such as the lattice spacing a_s and renormalised anisotropy ξ, via $V = N_s^3 a_s^3$ and $\xi = a_s/a_t$.

Whilst the fixed-scale approach is numerically cheaper than the fixed-N_t approach, it still requires the determination of the β function, which is not a cheap task. The initial inadequacies of the perturbative approach [73] and the prohibitive numerical expense of the non-perturbative approach led to the development of the so called integral method.

4.1.2 Integral Method

The trace anomaly I, aptly named due to it's otherwise zero value being non-zero as a result of a quantum anomaly, is given by the trace of the energy-momentum tensor and can be expressed in

terms of derivatives as;

$$I = \varepsilon - 3p = \frac{T}{V}\left(a_s \frac{\partial S_G}{\partial a_s}\bigg|_{\gamma_g} + a_s \frac{\partial S_F}{\partial a_s}\bigg|_{\gamma_g} \right). \tag{4.5}$$

This is cheaper to compute than the derivative method as it contains no derivatives with respect to the anisotropy γ_g. However due to the derivatives with respect to the lattice spacing a_s, the non-perturbative determination of the β functions are still required.

Utilising the fixed-N_t approach results in what is known plainly as the integral method [74], whereas the fixed-scale approach results in what is known as the T-integral method [75].

4.1.3 Small Flow Time Expansion Method

When computing the equation of state using the derivative method or the integral method, whilst taking the fixed-scale approach may save on computational expense, the non-perturbative determination of the β functions is nevertheless a significant task. One of the advantages of the gradient flow approach is to ameliorate this cost.

Gradient flow is defined for gauge fields in the continuum as;

$$\frac{\partial B_\mu(x,\tau)}{\partial \tau} = D_\nu G_{\nu\mu}(x,\tau) \,:\, B_\mu(x,\tau=0) = A_\mu(x), \tag{4.6}$$

where the flowed field strength tensor is given by;

$$G_{\nu\mu}(x,\tau) = \partial_\nu B_\mu(x,\tau) - \partial_\nu B_\mu(x,\tau) + [B_\nu(x,\tau), B_\mu(x,\tau)] \,:\, G_{\nu\mu}(x,\tau=0) = F_{\nu\mu}(x), \tag{4.7}$$

and the covariant derivative by;

$$D_\nu G_{\nu\mu} = \partial_\nu G_{\nu\mu} + [B_\nu, G_{\nu\mu}]. \tag{4.8}$$

The flowed fermion fields are defined by;

$$\partial_t \chi_f(x,\tau) = \Delta \chi_f(x,\tau) \,:\, \chi_f(x,\tau=0) = \psi_f(x), \tag{4.9}$$

$$\partial_t \bar{\chi}_f(x,\tau) = \bar{\chi}_f(x,\tau)\overleftarrow{\Delta} \,:\, \bar{\chi}_f(x,\tau=0) = \bar{\psi}_f(x), \tag{4.10}$$

with the derivatives being given as;

$$\Delta \chi_f(x,\tau) \equiv D_\mu D_\mu \chi_f(x,\tau) \,:\, D_\mu \chi_f(x,\tau) \equiv (\partial_\mu + B_\mu(x,\tau))\chi_f(x,\tau), \tag{4.11}$$

$$\bar{\chi}_f(x,\tau)\overleftarrow{\Delta} \equiv \bar{\chi}_f(x,\tau)\overleftarrow{D}_\mu\overleftarrow{D}_\mu : \bar{\chi}_f(x,\tau)\overleftarrow{D}_\mu \equiv (\overleftarrow{\partial}_\mu - B_\mu(x,\tau))\bar{\chi}_f(x,\tau). \tag{4.12}$$

The method outlined within this section follows the work presented by Suzuki et al [76]. The first step in the construction is to use the small flow time expansion to compute the energy-momentum tensor for quenched QCD ($N_f = 0$). The small flow time expansion [58], suggests that a composite operator $\tilde{O}(x,\tau)$ at flow time $\tau > 0$ can be related in the small flow time limit $\tau \to 0$, to a linear superposition of renormalised operators $O_i^R(x)$ for the gauge theory at zero flow time;

$$\tilde{O}(x,\tau) \xrightarrow[\tau\to 0]{} \sum_i c_i(\tau) O_i^R(x). \tag{4.13}$$

In quenched QCD studies [77–79] the flowed operators $\tilde{O}(x,\tau)$ are then taken to be;

$$E(\tau) = \frac{1}{4} G^a_{\mu\nu}(\tau) G^a_{\mu\nu}(\tau), \tag{4.14}$$

and;

$$U_{\mu\nu}(x,\tau) = G^a_{\mu\rho}(x,\tau)G^a_{\nu\rho}(x,\tau) - \frac{1}{4}\delta_{\mu\nu}G^a_{\rho\sigma}(x,\tau)G^a_{\rho\sigma}(x,\tau). \tag{4.15}$$

The small flowtime expansion then provides the expressions;

$$E(x,\tau) =< E(x,\tau) >_0 + \alpha_E(\tau) T^R_{\rho\rho}(x) + \mathcal{O}(\tau), \tag{4.16}$$

$$U_{\mu\nu}(x,\tau) = \alpha_U(\tau)\left(T^R_{\mu\nu}(x) - \frac{1}{4}\delta_{\mu\nu}T^R_{\rho\rho}(x)\right) + \mathcal{O}(\tau), \tag{4.17}$$

which can be combined to give the renormalised energy-momentum tensor;

$$T^R_{\mu\nu}(x) = \lim_{\tau\to 0}\left(\frac{1}{\alpha_U(\tau)}U_{\mu\nu}(x,\tau) + \frac{\delta_{\mu\nu}}{4\alpha_E(\tau)}(E(x,\tau) - < E(x,\tau) >_0)\right), \tag{4.18}$$

where as in the above references, the coefficients α_E and α_U are computed perturbatively. This expression is sometimes referred to as a universal formula for the energy-momentum tensor since it is valid for any regularisation scheme, including the lattice. Results for quenched QCD can be found within [80, 81], with similar work also done for pure $SU(2)$ gauge theory [57]. This work has also been extended to full QCD [82], with the universal formula for full QCD being validated also by a study within the Gross-Neveu model [83]. The correctly normalised energy-momentum tensor for full QCD is then given by [76];

$$T_{\mu\nu}(x) = \lim_{\tau\to 0}\left(\tilde{\mathcal{O}}_G + \tilde{\mathcal{O}}_F\right), \tag{4.19}$$

with the gluonic component given as;

$$\tilde{\mathcal{O}}_G = c_1(\tau)\left(\tilde{\mathcal{O}}_{1\mu\nu}(x,\tau) - \frac{1}{4}\tilde{\mathcal{O}}_{2\mu\nu}(x,\tau)\right) + c_2(\tau)\left(\tilde{\mathcal{O}}_{2\mu\nu}(x,\tau) - \left\langle \tilde{\mathcal{O}}_{2\mu\nu}(x,\tau)\right\rangle_0\right), \tag{4.20}$$

with the composite operators at $\tau > 0$;

$$\tilde{\mathcal{O}}_{1\mu\nu}(x,\tau) \equiv G^a_{\mu\rho}(x,\tau)G^a_{\nu\rho}(x,\tau), \tag{4.21}$$

$$\tilde{\mathcal{O}}_{2\mu\nu}(x,\tau) \equiv \delta_{\mu\nu}G^a_{\rho\sigma}(x,\tau)G^a_{\rho\sigma}(x,\tau). \tag{4.22}$$

The fermionic contribution is then given as;

$$\begin{aligned}\tilde{\mathcal{O}}_F = c_3(\tau)\sum_{f=u,d,s}&\left(\tilde{\mathcal{O}}^f_{3\mu\nu}(x,\tau) - 2\tilde{\mathcal{O}}^f_{4\mu\nu}(x,\tau) - \left\langle \tilde{\mathcal{O}}^f_{3\mu\nu}(x,\tau) - 2\tilde{\mathcal{O}}^f_{4\mu\nu}(x,\tau)\right\rangle_0\right)\\ + c_4(\tau)\sum_{f=,u,d,s}&\left(\tilde{\mathcal{O}}^f_{4\mu\nu}(x,\tau) - \left\langle \tilde{\mathcal{O}}^f_{4\mu\nu}(x,\tau)\right\rangle_0\right) + \sum_{f=u,d,s} c^f_5(\tau)\left(\tilde{\mathcal{O}}^f_{5\mu\nu}(x,\tau) - \left\langle \tilde{\mathcal{O}}^f_{5\mu\nu}(x,\tau)\right\rangle_0\right),\end{aligned} \tag{4.23}$$

with composite operators defined as;

$$\tilde{\mathcal{O}}^f_{3\mu\nu}(x,\tau) \equiv \phi_f(\tau)\bar{\chi}_f(x,\tau)(\gamma_\mu \overleftrightarrow{D}_\nu + \gamma_\nu \overleftrightarrow{D}_\mu)\chi_f(x,\tau), \tag{4.24}$$

$$\tilde{\mathcal{O}}^f_{4\mu\nu}(x,\tau) \equiv \phi_f(\tau)\delta_{\mu\nu}\bar{\chi}_f(x,\tau)\overleftrightarrow{\not{D}}\chi_f(x,\tau), \tag{4.25}$$

$$\tilde{\mathcal{O}}^f_{5\mu\nu}(x,\tau) \equiv \phi_f(\tau)\delta_{\mu\nu}\bar{\chi}_f(x,\tau)\chi_f(x,\tau). \tag{4.26}$$

The covariant derivative used here is given by;

$$\overleftrightarrow{D}_\mu \equiv D_\mu - \overleftarrow{D}_\mu, \tag{4.27}$$

and the normalisation factor for $N_f = 2+1$ QCD being given by;

$$\phi_f(\tau) \equiv -\frac{6}{(4\pi\tau)^2\left\langle \bar{\chi}_f(x,\tau)\overleftrightarrow{D}\chi_f(x,\tau)\right\rangle_0}. \tag{4.28}$$

In order for this universal energy-momentum tensor to be used the following coefficients must be

computed, which again were determined within [82] in the $\bar{\text{MS}}$ scheme at scale $\mu = 1/\sqrt{8\tau}$;

$$c_1(\tau) = \frac{1}{\bar{g}(1/\sqrt{8\tau})^2} - \frac{1}{(4\pi)^2}\left[9(\gamma - 2\ln 2) + \frac{19}{4}\right], \tag{4.29}$$

$$c_2(\tau) = \frac{1}{(4\pi)^2}\frac{33}{16}, \tag{4.30}$$

$$c_3(\tau) = \frac{1}{4}\left(1 + \frac{\bar{g}(1/\sqrt{8\tau})^2}{(4\pi)^2}\left[2 + \frac{4}{3}\ln 432\right]\right), \tag{4.31}$$

$$c_4(\tau) = \frac{1}{(4\pi)^2}\bar{g}(1/\sqrt{8\tau})^2, \tag{4.32}$$

$$c_5(\tau) = -\bar{m}_f(1/\sqrt{8\tau})\left(1 + \frac{\bar{g}(1/\sqrt{8\tau})^2}{(4\pi)^2}\left[4(\gamma - 2\ln 2) + \frac{14}{3} + \frac{4}{3}\ln 432\right]\right). \tag{4.33}$$

These coefficients are straightforward apart from the determination of the running gauge coupling $\bar{g}(\mu)$ and the running quark mass $\bar{m}_f(\mu)$ in them. These terms are determined according to the prescription laid out in appendix C of [76], where the renormalisation group invariant scale is defined by;

$$\frac{\Lambda}{\mu} = \left(b_0\bar{g}(\mu)^2\right)^{-b_1/(2b_0^2)} \exp\left\{-\frac{1}{2b_0\bar{g}(\mu)^2}\right\} \exp\left\{-\int_0^{\bar{g}(\mu)} dg\left(\frac{1}{\beta(g)} + \frac{1}{b_0 g^3} + \frac{b_1}{b_0^2 g}\right)\right\}, \tag{4.34}$$

and the running mass and renormalisation group invariant mass M are defined by;

$$\bar{m}(\mu) = M\left(2b_0\bar{g}(\mu)^2\right)^{d_0/(2b_0)} \exp\left\{\int_0^{\bar{g}(\mu)} dg\left(\frac{\tau(g)}{\beta(g)} + \frac{d_0}{b_0 g}\right)\right\}, \tag{4.35}$$

which using the values for b_i, d_i, $\tau(g)$ and $\beta(g)$ defined in the above reference, can be solved numerically. Alternatively for the running gauge coupling, an approximate formula from the particle data group [84] can be used;

$$\begin{aligned}\bar{g}(\mu)^2 =& \frac{1}{b_0 t}\left(1 - \frac{b_1}{b_0^2}\frac{\ln(t)}{t} + \frac{b_1^2(\ln(t)^2 - \ln(t) - 1) + b_0 b_2}{b_0^4 t^2}\right. \\ &\left. - \frac{b_1^3(\ln(t)^3 - \frac{5}{3}\ln(t)^2 - 2\ln(t) + \frac{1}{2}) + 3b_0 b_1 b_2 \ln(t) - \frac{1}{2}b_0^2 b_3}{b_0^6 t^3}\right) : t \equiv \ln\left(\frac{\mu^2}{\Lambda^2}\right).\end{aligned} \tag{4.36}$$

Once the energy-momentum tensor is computed the expectation value can be used to compute the pressure p and energy density ϵ at temperature T as a function of flow time τ/a_s^2;

$$p/T^4 = \sum_i < T_{ii} > /(3T^4), \tag{4.37}$$

$$\epsilon/T^4 = - < T_{00} > /T^4, \tag{4.38}$$

with the entropy density then being given by;

$$\frac{\epsilon + p}{T^4} = -\frac{4}{3T^4} < T_{00} - 4^{-1} T_{\mu\mu} > , \tag{4.39}$$

and the trace anomaly by;

$$\frac{\epsilon - 3p}{T^4} = -\frac{1}{T^4} < T_{\mu\mu} > . \tag{4.40}$$

There are a few technical subtleties that are required for using the above prescription to determine the lattice energy-momentum tensor. Firstly the maximum safe flow time where boundary effects from over-smearing are avoided is given by;

$$\frac{\tau}{a_s^2} \leq \tau_{1/2} \equiv \frac{1}{8}\left[\min\left(\frac{N_t}{2}, \frac{N_s}{2}\right)\right]^2. \tag{4.41}$$

Secondly when the required limit $\tau \to 0$ is taken, small flow time effects must be accounted for and when the continuum limit is taken $a \to 0$, lattice artifacts must also be taken into account. The relation between the energy-momentum tensor on the lattice that is constructed from flowed operators, $T_{\mu\nu}(x, \tau, a)$, and the physical target energy-momentum tensor $T_{\mu\nu}(x)$, is given by;

$$T_{\mu\nu}(x,\tau,a) = T_{\mu\nu}(x,\tau) + A_{\mu\nu}(x)\frac{a^2}{\tau} + \sum_f B_{f\mu\nu}(am_f)^2 + C_{\mu\nu}(aT)^2 + D_{\mu\nu}(x)(a\Lambda_{QCD})^2 + a^2 S'_{\mu\nu}(x) + \mathcal{O}(a^4), \tag{4.42}$$

$$T_{\mu\nu}(x,\tau) = T_{\mu\nu}(x) + \tau S_{\mu\nu}(x) + \mathcal{O}(\tau^2). \tag{4.43}$$

The FASTSUM research program has not yet reached the point of being able to take the continuum limit thanks to the time taken to tune each set of parameters on the anisotropic lattice. Thus it is necessary to take the small flow time limit $\tau \to 0$ without first having taken the continuum limit $a \to 0$, for which it is clear that a singular term appears at small enough flow time. The solution, as is taken in [76], is to recognise that the lattice energy-momentum tensor is related to the physical target value by the addition of a term which is linear in flow time. Thus if this linear region can be observed with flow time, then it can be used to safely linearly extrapolate to $\tau \to 0$ without interference from the singular term.

At this point the prescription for how to construct the lattice energy-momentum tensor, and how to

obtain physical results is clear. The only remaining question is how to implement the flow equations eq. (4.6) and eq. (4.9). The implementation for the gauge fields was given in chapter 3 and is recapitulated here for the reader's convenience. In order to evolve the gauge fields through flowtime, the lattice discretisation of the gauge field flow equation eq. (3.1) is solved using numerical integration with the third order Runge-Kutta integrator. Recasting the differential equation into the general form;

$$\partial_\tau V_\tau = Z(V_\tau)V_\tau, \tag{4.44}$$

and with the initial condition;

$$V(x,\mu,\tau=0) = U(x,\mu), \tag{4.45}$$

the integration from flowtime τ to $\tau+\epsilon$ is given by;

$$\begin{aligned} X_0 =& V_\tau, \\ X_1 =& \exp\left\{\frac{Z_0}{4}\right\}X_0, \\ X_2 =& \exp\left\{\frac{8Z_1}{9} - \frac{17Z_0}{36}\right\}X_1, \\ V_{\tau+\epsilon} =& \exp\left\{\frac{3Z_2}{4} - \frac{8Z_1}{9} + \frac{17Z_0}{36}\right\}X_2, \end{aligned} \tag{4.46}$$

where $Z_i \equiv \epsilon Z(X_i)$.

Following the exposition laid out in appendix A of [76], the fermion flow is required to compute those expectation values of the form;

$$t^f_{\mu\nu}(\tau) \equiv \frac{1}{N_\Gamma}\sum_x < \bar{\chi}_f(x,\tau)\gamma_\mu(D_\mu - \overleftarrow{D}_\nu)\chi_f(x,\tau) > , \tag{4.47}$$

$$s^f(\tau) \equiv \frac{1}{N_\Gamma}\sum_x < \bar{\chi}_f(x,\tau)\chi_f(x,\tau) > , \tag{4.48}$$

with the number of lattice points N_Γ. These expectation values can be re-expressed in the form;

$$t^f_{\mu\nu}(t) = \frac{2}{N_\Gamma}\,\mathrm{Re}\left\langle\left\langle \sum_{\alpha,i}\left[\sum_\nu \psi_{\mu\nu}(t;0,\nu)^\dagger \sum_w S_f(\nu,w)\xi(t;0,w)\right]_{\alpha i,\alpha i}\right\rangle_\eta\right\rangle, \tag{4.49}$$

$$\begin{aligned} s^f(t) =& -\frac{1}{N_\Gamma}\left\langle\left\langle \sum_{\alpha,i}\left[\sum_\nu \xi(t;0,\nu)^\dagger \sum_w S_f(\nu,w)\xi(t;0,w)\right]_{\alpha i,\alpha i}\right\rangle_\eta\right\rangle \\ &+c_{fl}\frac{1}{N_\Gamma}\left\langle\left\langle \sum_{\alpha,i}\left[\sum_\nu \xi(t;0,\nu)^\dagger\xi(t;0,\nu)\right]_{\alpha i,\alpha i}\right\rangle_\eta\right\rangle, \end{aligned} \tag{4.50}$$

where;

$$\xi(t;s,w) \equiv \sum_x K(t,x;s,w)^\dagger \eta(x), \tag{4.51}$$

$$\psi_{\mu\nu}(t;s,w) \equiv \gamma_\mu \sum_x K(t,x;s,w)^\dagger D_\nu \eta(x), \tag{4.52}$$

and is composed of the randomly generated complex scalar field $\eta(x)$ (noisy estimator method) which satisfies;

$$< \eta(x) >_\eta = 0 \ , \ < \eta(x)\eta(y)^* >= \delta_{x,y}, \tag{4.53}$$

and $K(t,x;s,y)$ is the fundamental solution to the flow equation and is defined by;

$$(\partial_t - \Delta)K(t,x;s,y) = 0 \ , \ K(t,x;t,y) = \delta_{x,y}. \tag{4.54}$$

The quark propagator $S_f(x,y)$ with the bare mass m_{f0} is given by;

$$(\not{D} + m_{f0})S_f(x,y) = \delta_{x,y}. \tag{4.55}$$

The task then involves solving the so called adjoint flow equations;

$$(\partial_s + \Delta)\xi(t;s,w) = 0 \ , \ \xi(t;t,w) = \eta(w) \tag{4.56}$$

$$(\partial_s + \Delta)\psi_{\mu\nu}(t;s,w) = 0 \ , \ \psi_{\mu\nu}(t;t,w) = \gamma_\mu D_\nu \eta(w), \tag{4.57}$$

backwards from flowtime $\tau = t$ to $\tau = 0$. However the flow is unstable when flowed in this direction [85], and thus is computationally expensive as it required multiple sweeps forward through flowtime. The equation to solve can be expressed in a more abstract form as;

$$\partial_s \xi_s = -\Delta(V_s)\xi_s, \tag{4.58}$$

which can then be solved using the iterative procedure;

$$\begin{aligned}
\lambda_3 =& \xi_{s+\epsilon}, \\
\lambda_2 =& \frac{3}{4}\Delta_2 \lambda_3, \\
\lambda_1 =& \lambda_3 + \frac{8}{9}\Delta_1 \lambda_2, \\
\lambda_0 =& \lambda_1 + \lambda_2 + \frac{1}{4}\Delta_0 \left(\lambda_1 - \frac{8}{9}\lambda_2 \right),
\end{aligned} \tag{4.59}$$

where $\Delta_i = \epsilon\Delta(W_i)$ for $i = 0, 1, 2$ and $\xi_s = \lambda_0$. The error is of order $\mathcal{O}(\epsilon^4)$.

Before discussing the results of this thesis, it is worth noting that several other methods for determining the energy-momentum tensor on the lattice have been devised. As demonstrated within [19] the correctly normalised energy-momentum tensor that reproduces the correct Ward-Takahashi relation in the continuum limit can be written as;

$$\hat{T}_{\mu\nu}(x) = Z_6\hat{T}^{[6]}_{\mu\nu}(x) + Z_3\hat{T}^{[3]}_{\mu\nu}(x) + Z_1\left[\hat{T}^{[1]}_{\mu\nu}(x) - <\hat{T}^{[1]}_{\mu\nu}(x)>\right], \tag{4.60}$$

where $\hat{T}^{[6]}_{\mu\nu}(x)$ contains only off diagonal elements whilst $\hat{T}^{[3]}_{\mu\nu}(x)$ contains only diagonal elements and is traceless, with both being well defined in the above reference. The task is then to determine the renormalisation constants Z_6, Z_3 and Z_1. One approach is to use shifted boundary conditions in order to derive physical normalisation conditions which can then be used to compute Z_i [86–89]. This approach can enable the determination of the coefficients via one-point correlators which can typically be well determined and thus the results are accurate. This method requires the construction of special configurations however and thus can't be readily applied to existing lattice data. Another approach is to use the gradient flow to probe the Ward-Takahasi relation in order to determine the values of Z_i [90–92]. This approach can be applied to any lattice data, however in order to avoid small flow time artifacts large flow times are required, which often results in poor signal to noise ratio and thus requires high statistics, making this approach expensive for full QCD. The Suzuki method can be performed on any data, and has been successfully applied at smaller flow times without any substantial issues from artifacts. The key advantage of the Suzuki method is that in principle, for a sufficiently small coupling, the renormalisation coefficients involved have been perturbatively determined and thus provides an easier path to non-perturbatively determining the energy-momentum tensor.

Results

The work presented within this section represents the first implementation on an anisotropic lattice of the method laid out by Suzuki et al [76], for constructing the energy-momentum tensor. Hence the work presented here will include only the gluonic contribution to the energy-momentum tensor, with the fermionic contribution left as a next step within this research program.

The coefficients c_1 and c_2 which were given in eq. (4.29) and eq. (4.30) and computed within [82], were determined perturbatively. The determination of the running gauge coupling $\bar{g}(\mu)$ was not possible for the present lattice spacing of $a_s = 0.11208$ fm, as a solution to eq. (4.34) is not available for this coupling at sufficiently large flow times up to $\tau = 32$, with no solution being available even for such low flow times as $\tau = 1.5$. The approximate formula eq. (4.36) can obtain a solution to slightly larger flow times around $\tau = 3.25$, with the clear sign of strong coupling being shown within fig. 4.1a. The strong coupling suggests that the form of the c_1 and c_2 coefficients are themselves not appropriate for use in this case and thus even the constant c_2 coefficient cannot be used. Thus within this work

the coefficients are set to $c_1 = c_2 = 1$, and must be determined non-perturbatively in the next stages of this research program before a final comparison to the literature will be possible.

It is clear from the construction of the energy-momentum tensor eq. (4.20) and the definition of the pressure eq. (4.37), and energy density eq. (4.38), that the trends for pressure and energy density as functions of flow time should be sensitive to the c_1 and c_2 coefficients, which are themselves functions of flow time. Consequently the extrapolation of the pressure and energy density to $\tau = 0$ is expected to change considerably once the values of c_1 and c_2 have been determined and incorporated within this analysis. With that said it does appear that both the energy density ϵ, and pressure p, demonstrate a linear window for extrapolation within the safe flow time for all temperatures in the range $T = 95 \rightarrow 380$ MeV, with only the smallest two lattices failing to provide a usable fiducial window, and thus the analysis is performed as usual on the presently available data with a clear understanding that these results are exploratory and cannot yet be compared to the literature. The data for $T = 47$ MeV was used as the zero temperature data point to compute the vacuum expectation value for eq. (4.20), and is thus itself omitted from the energy density and pressure results.

The data for the energy density as a function of flow time is presented within fig. 4.2a to fig. 4.7b, with all lattices providing the expected linear region for extrapolation within a safe flow time apart from the two smallest lattices $N_t = 8, 12$. The upper limit on a possible fiducial window for the extrapolation is provided by the maximum safe flow time, determined by eq. (4.41) and computed for each lattice within table 4.1. However the requirement is to provide a linear region for extrapolation and thus it was deemed appropriate to use the linear regression goodness of fit parameter R^2, to determine whether the data within the fiducial window is well captured by the linear model, and hence whether the data within that region was in fact linear. The final extrapolated values and the corresponding R^2 values are given for both the energy density and pressure within table 4.2. The linear windows within the safe flow time were selected so as to provide a fit with $R^2 \geq 0.950$.

The error included within these figures is entirely statistical and was determined by jackknife analysis performed directly on the energy density for each flow time measurement. A systematic error was determined by varying the fiducial window within the chosen region so as to sample ten subsets of the selected data, with the standard deviation of the resultant distribution being taken as the error, which is given in table 4.2. Each subset used to determine the systematic error also showed good linear behaviour, with an $R^2 \geq 0.950$. The chi-squared per degree of freedom, χ^2_{dof}, was also computed for each extrapolation, the values for which are also included within table 4.2. The statistical errors were consistently on the sub-percent level, whereas the systematic error was substantially larger, often at the percent level. This larger systematic error is not to be taken too seriously at the present level of analysis whilst $c_1 = c_2 = 1$, given that the trend in the data is expected to change, with the extent of that change being unknown. Likewise, the small statistical error is expected to provide a slightly larger percentage error once the values for ϵ itself are brought under better control by the application of the appropriate c_1 and c_2 coefficients. The data for the energy density demonstrates the anticipated singular behaviour towards $\tau = 0$, however the magnitude of the extrapolated values

is significantly larger than anticipated and their sign is not expected to be negative. Again it must be firmly stated that this deviation from the expected behaviour is not to be interpreted as significant in the absence of the appropriate c_1 and c_2 coefficients, which are expected to change the resultant data considerably. The extrapolations were performed with a generalised least squares fit in order to account for any correlation within the data. Furthermore when c_1 and c_2 have been determined non-perturbatively, they will provide another source of systematic error. Within the work of Suzuki et al [76], different fits are performed in order to determine the systematic error associated with the fit Ansätze. One of the Ansätze used is a linear+log fit, which is not appropriate for use within this work as it is based on the error within c_1 and c_2, which are set to unity here. Anther fit Ansätze could include a non-linear term involving a^2/τ, however as shown by Suzuki et al this only contributes significantly for values of τ near zero, and thus with the fiducial window within this work being so high in flow time, it is not anticipated to be significant relative to the systematic error that was computed by varying the fiducial widow. This will however be investigated once the correct c_1 and c_2 values and their systematic errors are determined and the resultant trends with flow time in the ϵ and p data are physically meaningful.

The resultant energy density as a function of temperature is displayed within fig. 4.14, showing only the statistical error, with the expected trend from the literature being given in fig. 4.16a. Whilst the results presented here are not final, it is nevertheless interesting to compare against the literature to see how these results can be anticipated to change once the c_1 and c_2 coefficients are included at a later stage. There are two key discrepancies between the data presented within fig. 4.14b and that of Suzuki et al within fig. 4.16a, the first being the negative magnitude within the results of this work, which is not physically meaningful, and the second is that the spread of values between the lowest and highest temperature is far larger in the work presented here. The latter of these discrepancies is reason to believe that although the overall trend may be somewhat similar from around $T \geq 200$ MeV, that this is likely coincidental and not to be seen favourably. The data presented within fig. 4.14a shows the energy density for all available temperatures, including temperatures as low as 95 MeV. The χ^2_{dof} values show good agreement between the fit and the data for all ensembles, with the R^2 value suggesting that the data within the fiducial window is linear in nature.

The data for the pressure as a function of flow time is presented within fig. 4.8a to fig. 4.13b, with the resultant extrapolated values given in table 4.2. The details of the determination of the statistical error and systematic error are identical to that of the energy density. The fiducial window was taken to be the same as that used for the energy density. A linear region within the safe flow time was again successfully identified for all but the smallest two lattices $N_t = 8, 12$. The anticipated singular behaviour can be seen near $\tau = 0$, with the data all being positive. The final data for pressure as a function of temperature is shown within fig. 4.15, with the expected trend from the literature shown in fig. 4.16b. The work presented here within fig. 4.15 demonstrates a nonphysical negative trend with increasing temperature, which further supports the expectation that the contribution of the c_1 and c_2 coefficients is significant and thus that the current level of analysis with $c_1 = c_2 = 1$ cannot be meaningfully compared to the literature. Similarly the spread in the pressure values with temperature is again substantially larger than that observed within the work of Suzuki et al within

fig. 4.16b. The trend in the pressure with decreasing temperature shown within fig. 4.15a is consistent with the opposite of the physical expectation, which would be a smoothly decreasing pressure with temperature.

The discussion of the work presented within this section has been necessarily exploratory due to the lack of knowledge of the coefficients c_1 and c_2. Comparison against the literature can however be insightful in specifying the anticipated changes in the results once this analysis is performed with the non-perturbatively determined c_1 and c_2. The spread in magnitude for both energy density and pressure with increasing temperature is expected to decrease, with the energy density taking positive values and the pressure reversing its trend with relation to increasing temperature.

The key next step is to determine the c_1 and c_2 coefficients non-perturbatively. Another objective within the research program is to include the fermion contribution to the energy-momentum tensor. Based on the work of Suzuki et al within [76], the expectation is that the heavier strange quark will contribute similarly to the gauge component, whilst the lighter up and down quarks will contribute several times as much. The determination of the fermionic contribution will however require its own determination of the coefficients c_3, c_4 and c_5.

A key reason for selecting the method of Suzuki et al for the application on the anisotropic lattice was the belief that the method presented fewer technical tasks, in particular with no renormalisation coefficients needing to be determined. However it has become clear that due to the parameters used to generate the configurations which were used within this work, the signal of interest is present at larger flow times, for which with the present coupling the perturbative determination of the coefficients within eq. (4.20) cannot be used. It is not clear at present whether this method requires more work to utilise than its competitors, but the determination of the coefficients c_i will not be trivial to determine non-perturbatively. It should be noted that these configurations were not tuned with such studies in mind and perhaps a different parameter setup would alleviate this issue. This analysis will be repeated in the near future on subsequent generations of configurations with different parameters to those used here, at which point it will be interesting to see how high in flow time the fields must be taken in order to obtain the required signal for the observables of interest. A final comment should be made on the applicability of the small flow time expansion [58], which the Suzuki method is based on. Whilst the physical interpretation of the data is only given in the $\tau \to 0$ limit (and $a \to 0$ limit), it may be that the extent to which the flow time has needed to be taken within this work is such that the method cannot be applied. However this can only be determined once the correct c_1 and c_2 coefficients are applied and the physical results are compared to the literature.

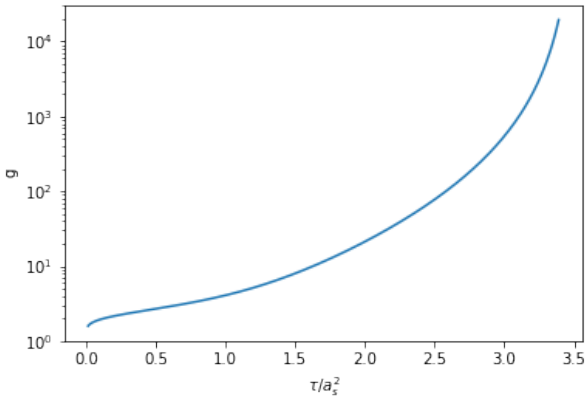

(a)

Fig. 4.1: The running gauge coupling as a function of flowtime for a lattice spacing of $a_s = 0.11208$ fm, computed using the approximate formula given in eq. (4.36).

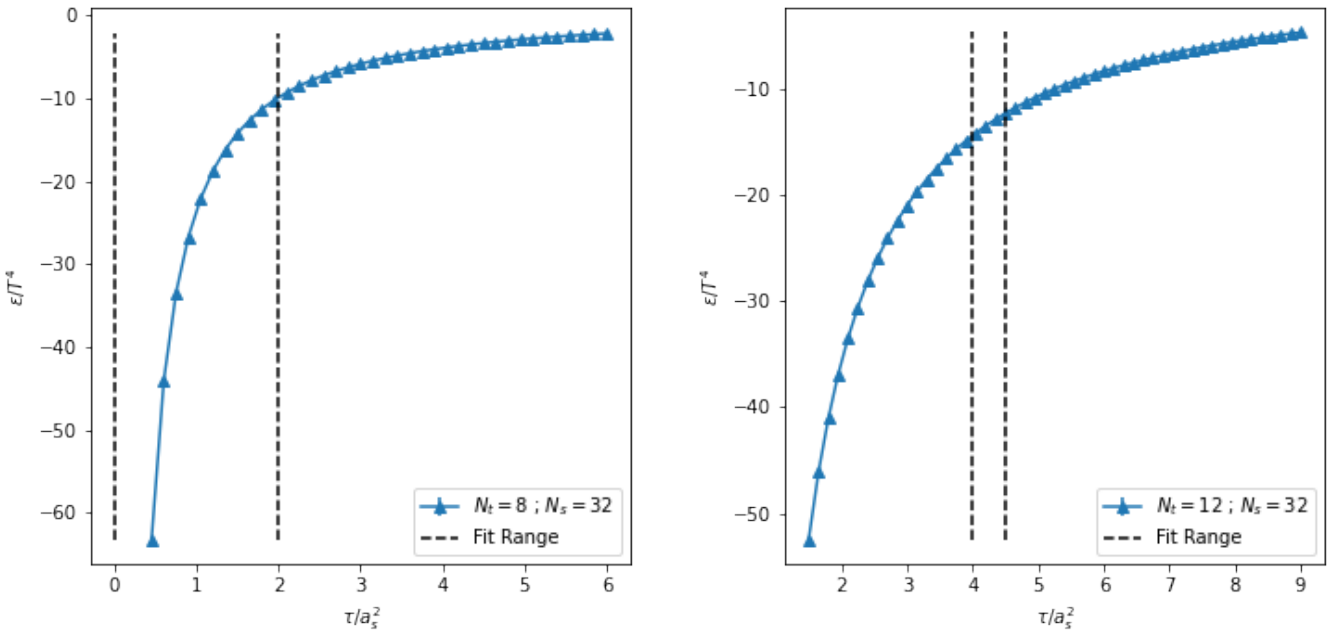

(a) **(b)**

Fig. 4.2: Energy density vs flow time, computed using the gluonic contribution to the expectation value of the energy-momentum tensor.

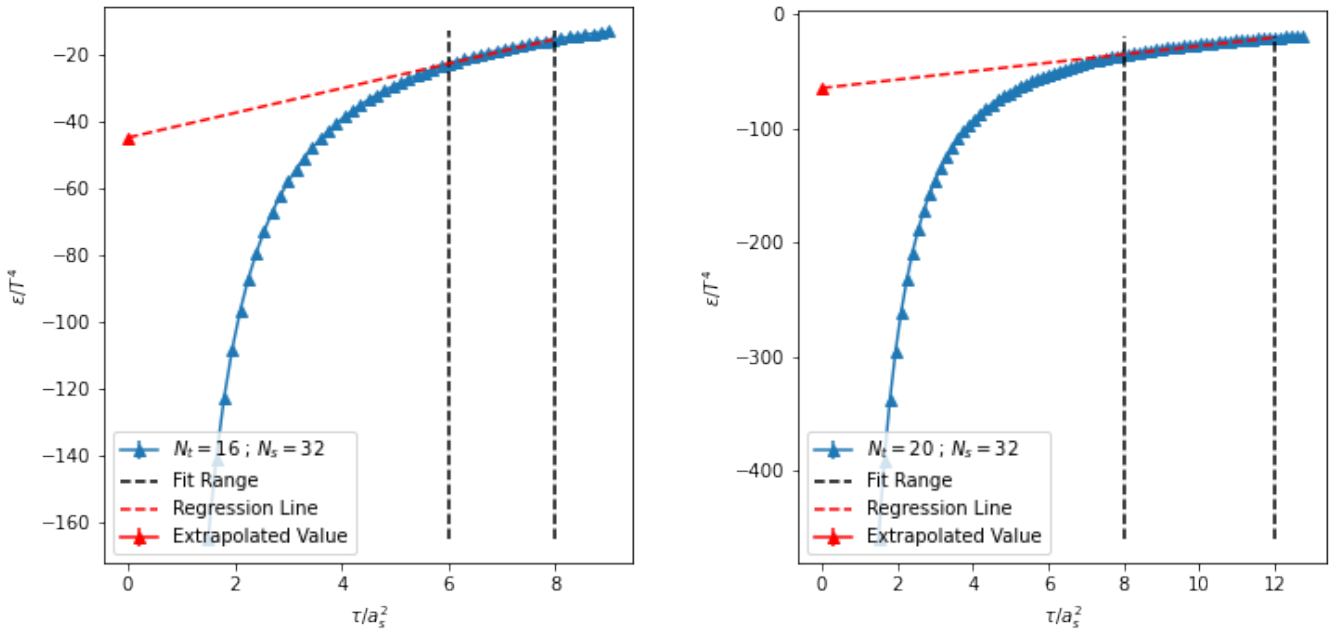

(a) **(b)**

Fig. 4.3: Energy density vs flow time, computed using the gluonic contribution to the expectation value of the energy-momentum tensor.

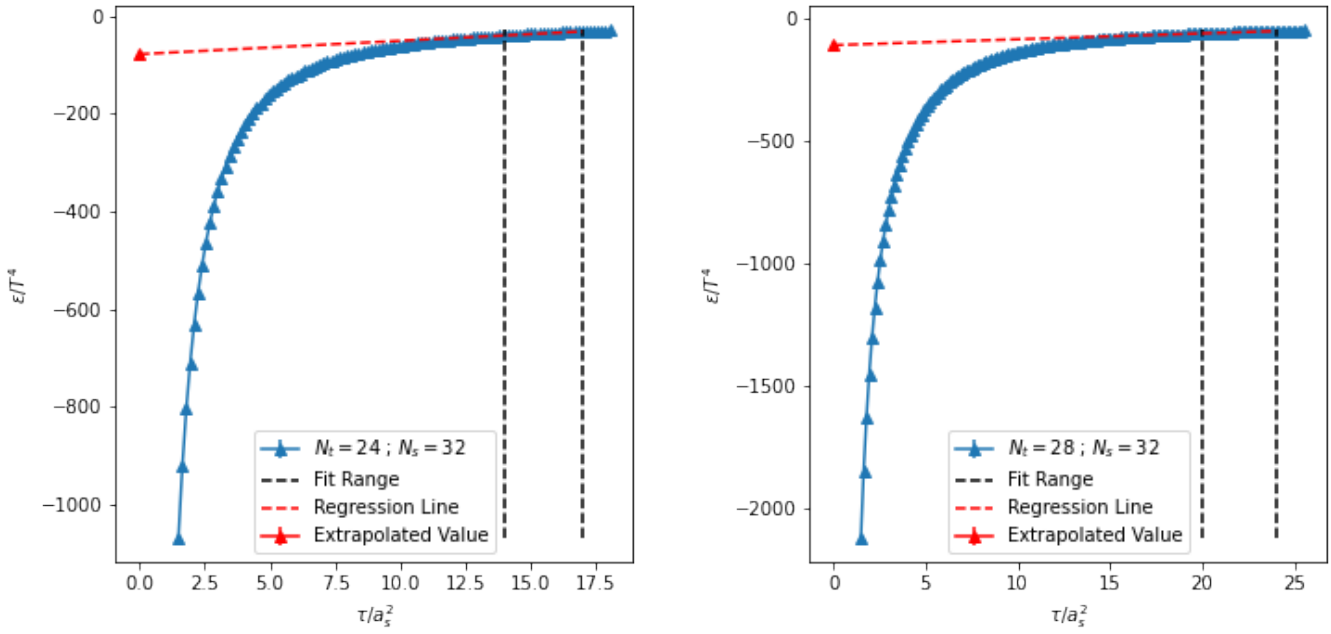

(a) **(b)**

Fig. 4.4: Energy density vs flow time, computed using the gluonic contribution to the expectation value of the energy-momentum tensor.

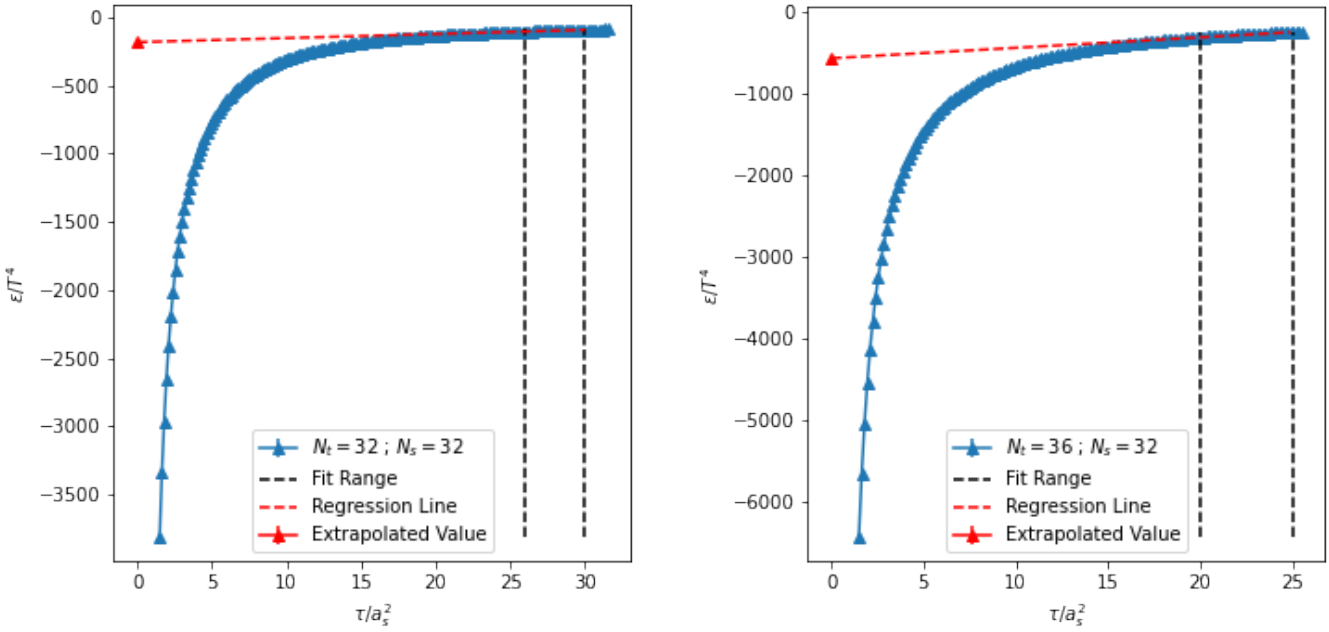

(a) **(b)**

Fig. 4.5: Energy density vs flow time, computed using the gluonic contribution to the expectation value of the energy-momentum tensor.

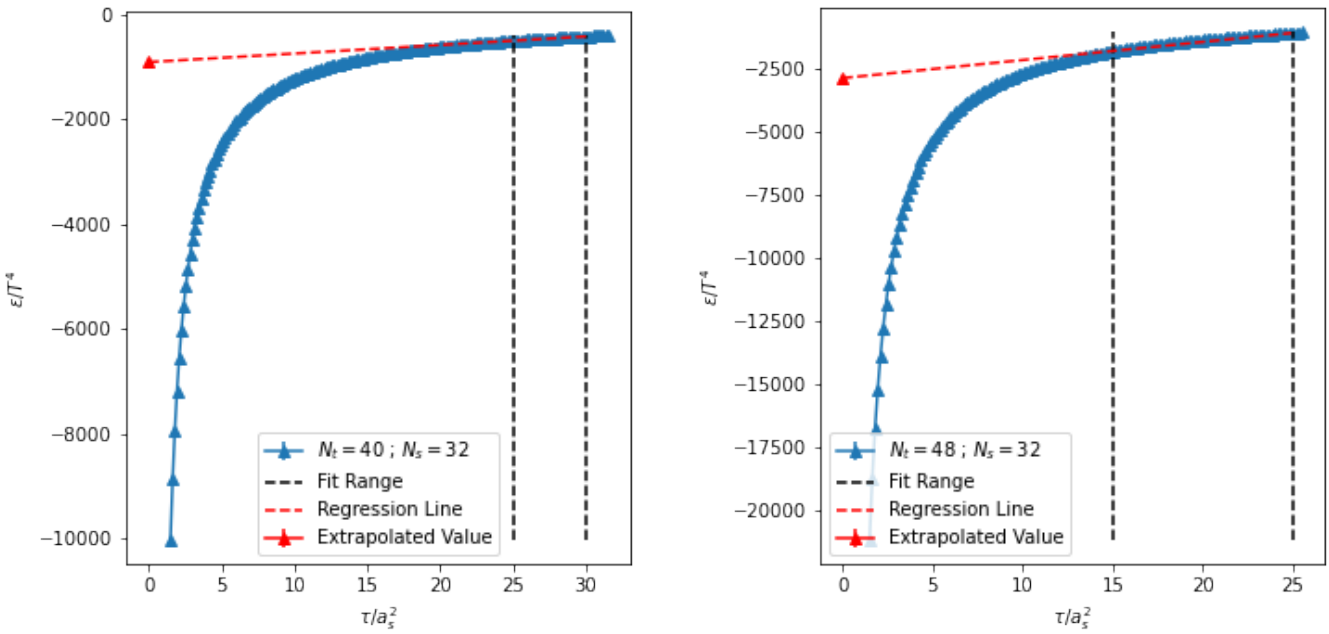

(a) **(b)**

Fig. 4.6: Energy density vs flow time, computed using the gluonic contribution to the expectation value of the energy-momentum tensor.

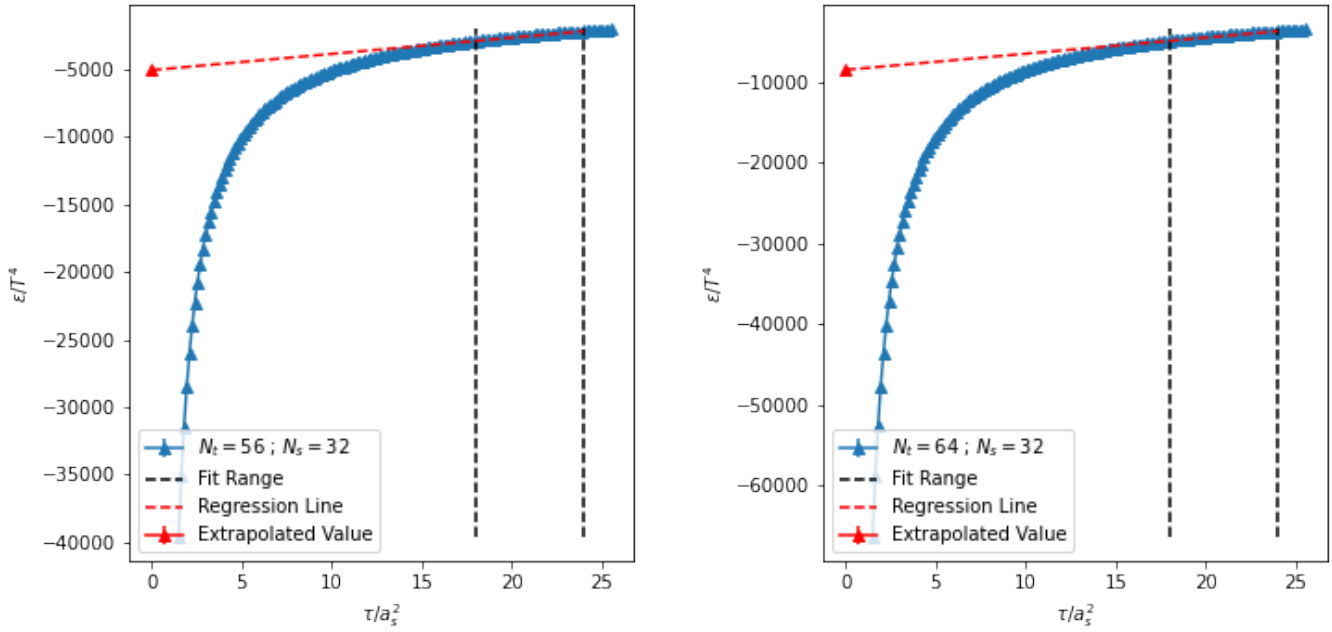

(a) **(b)**

Fig. 4.7: Energy density vs flow time, computed using the gluonic contribution to the expectation value of the energy-momentum tensor.

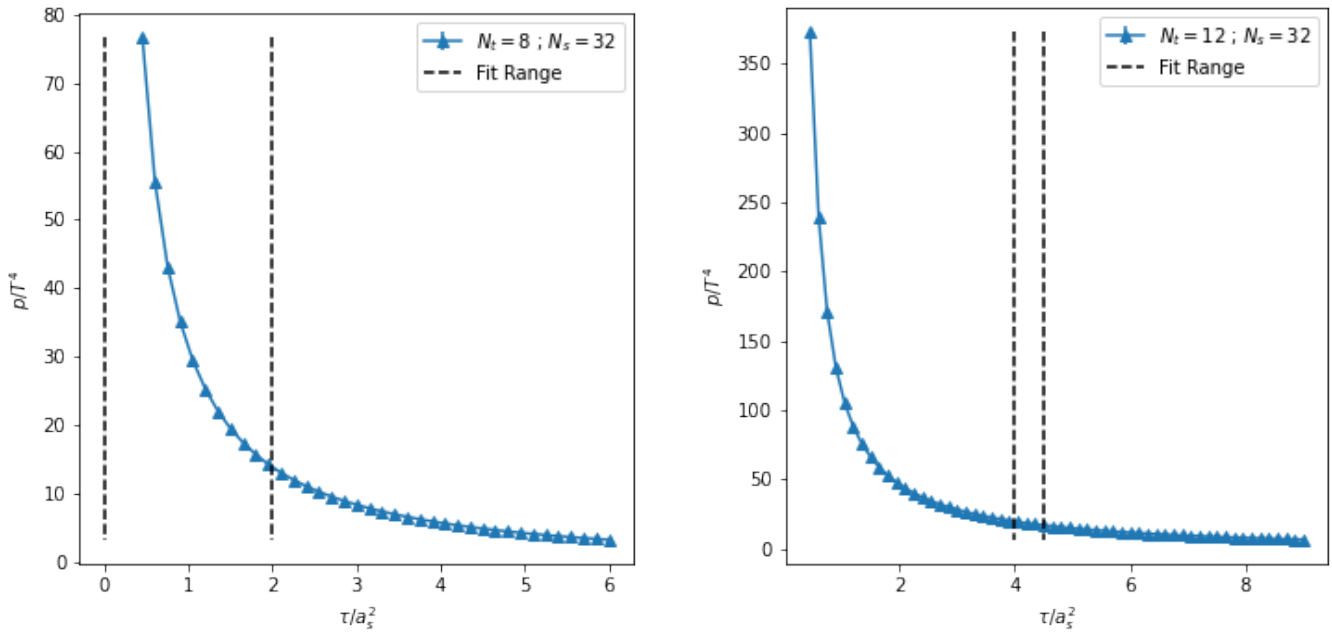

(a) **(b)**

Fig. 4.8: Pressure vs flow time, computed using the gluonic contribution to the expectation value of the energy-momentum tensor.

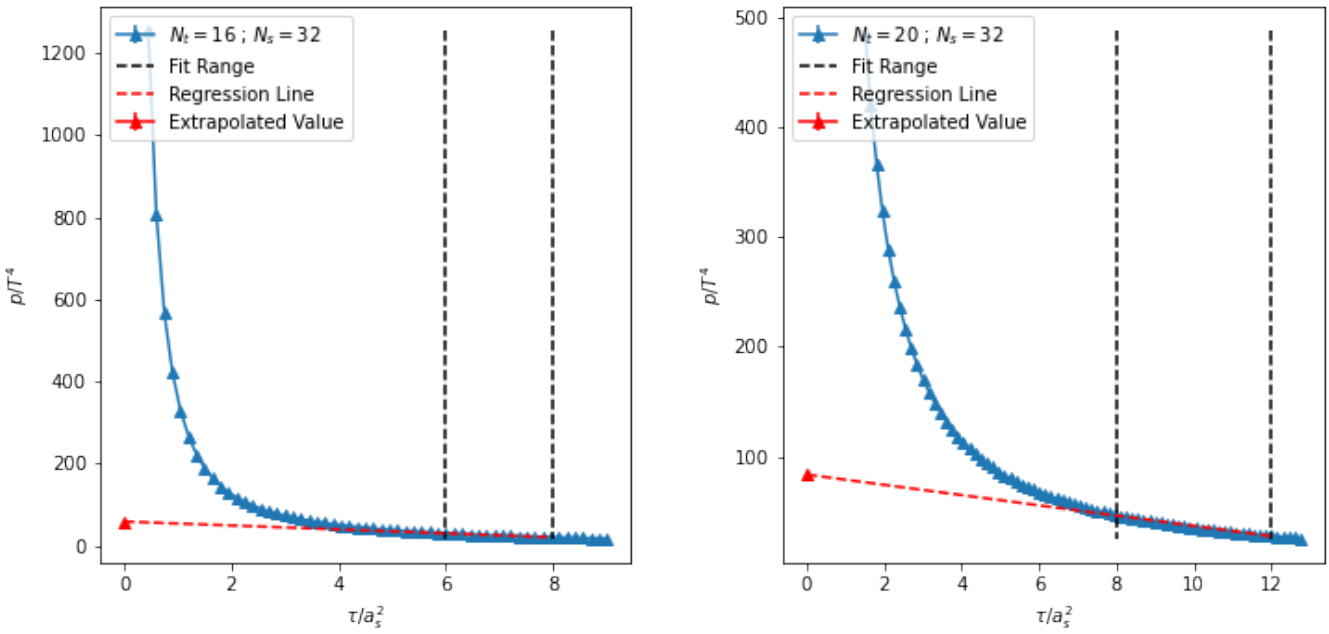

(a) **(b)**

Fig. 4.9: Pressure vs flow time, computed using the gluonic contribution to the expectation value of the energy-momentum tensor.

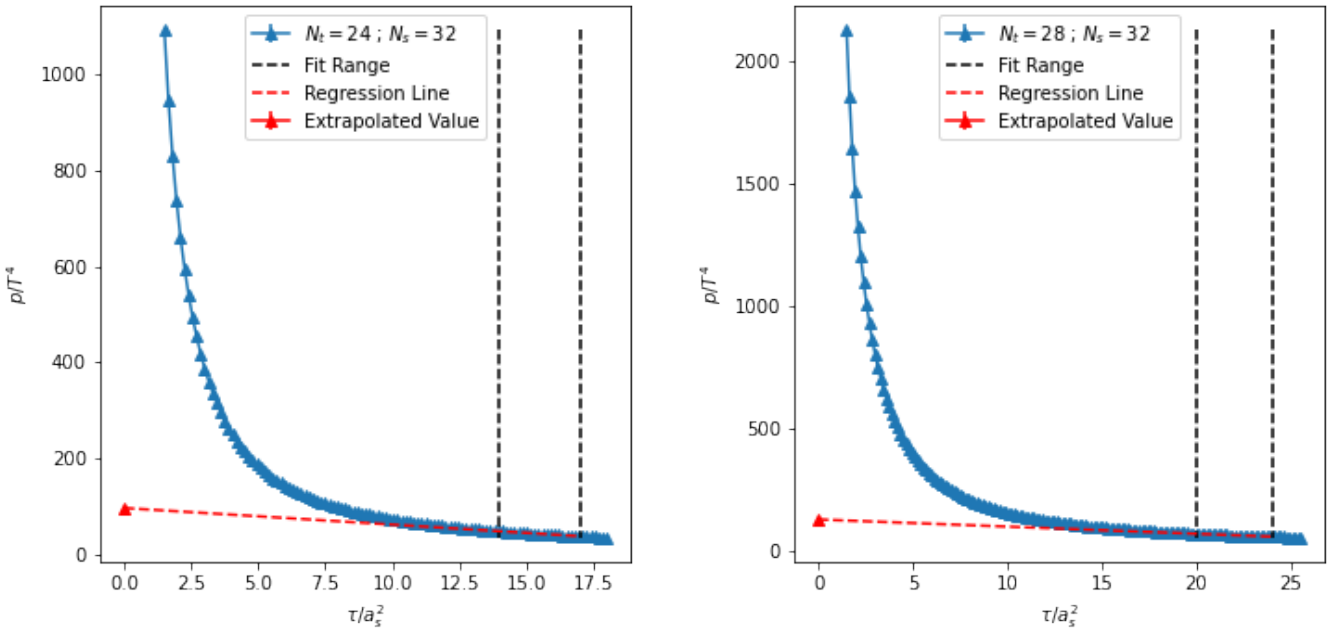

(a) **(b)**

Fig. 4.10: Pressure vs flow time, computed using the gluonic contribution to the expectation value of the energy-momentum tensor.

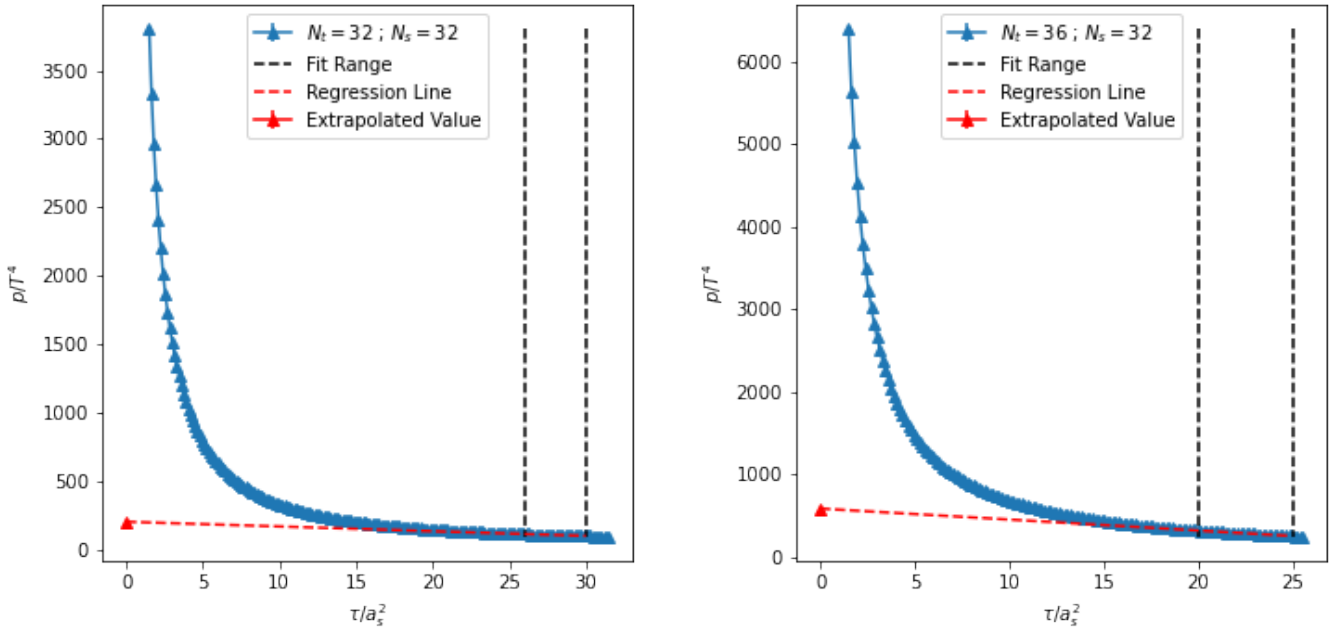

(a) **(b)**

Fig. 4.11: Pressure vs flow time, computed using the gluonic contribution to the expectation value of the energy-momentum tensor.

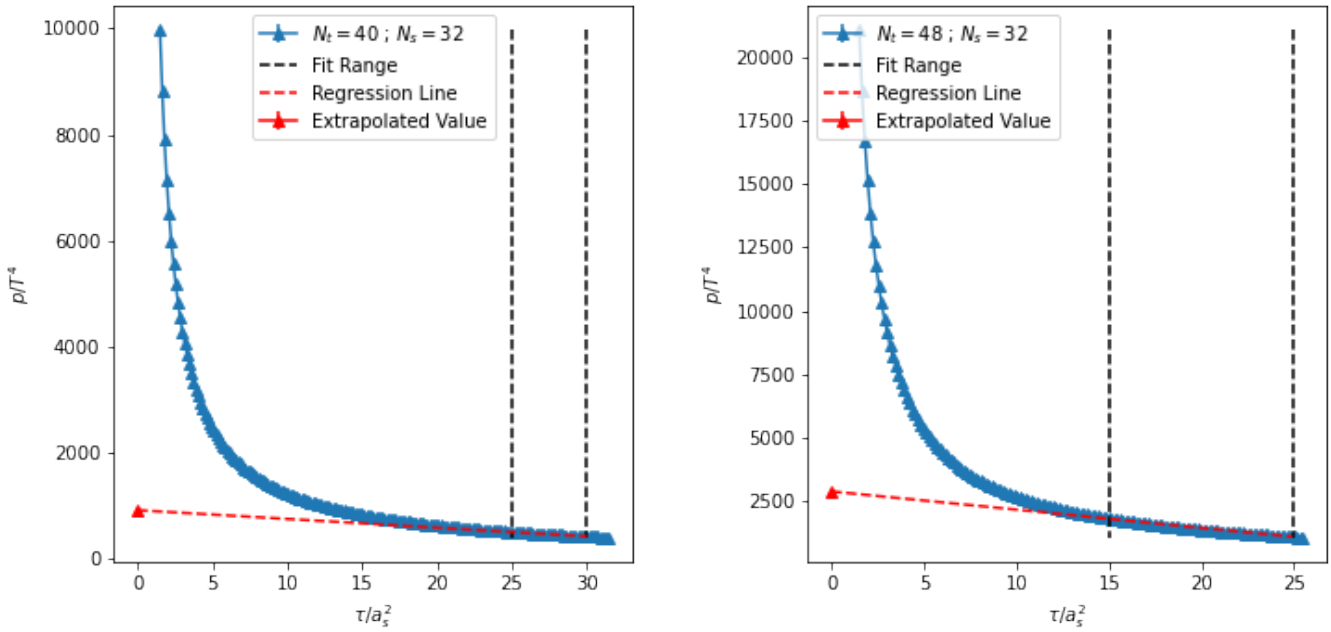

(a) **(b)**

Fig. 4.12: Pressure vs flow time, computed using the gluonic contribution to the expectation value of the energy-momentum tensor.

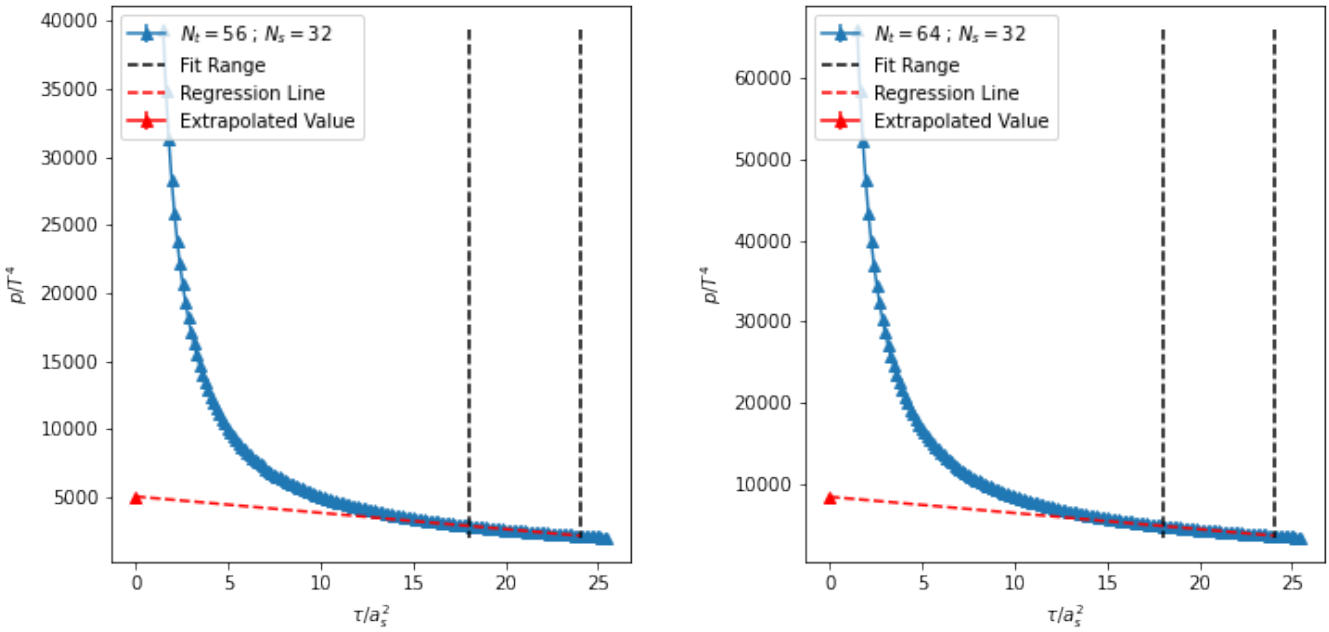

(a) **(b)**

Fig. 4.13: Pressure vs flow time, computed using the gluonic contribution to the expectation value of the energy-momentum tensor.

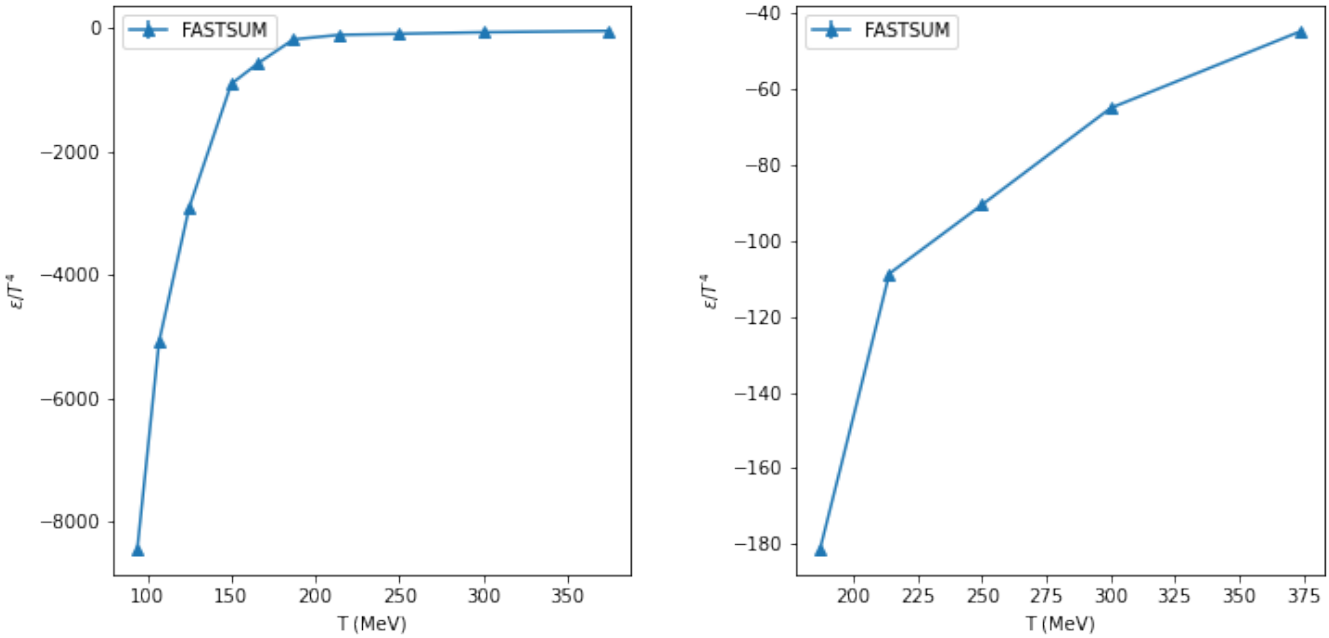

(a) Energy density vs temperature from the gluonic energy-momentum tensor, showing the data for all temperatures.

(b) Energy density vs temperature from the gluonic energy-momentum tensor, focusing on region of interest for comparison with Suzuki et al.

Fig. 4.14: Preliminary data for the energy density as a function of temperature. These values were extrapolated using eq. (4.20) with the coefficients set to $c_1 = c_2 = 1$. The errors within these plots are statistical only.

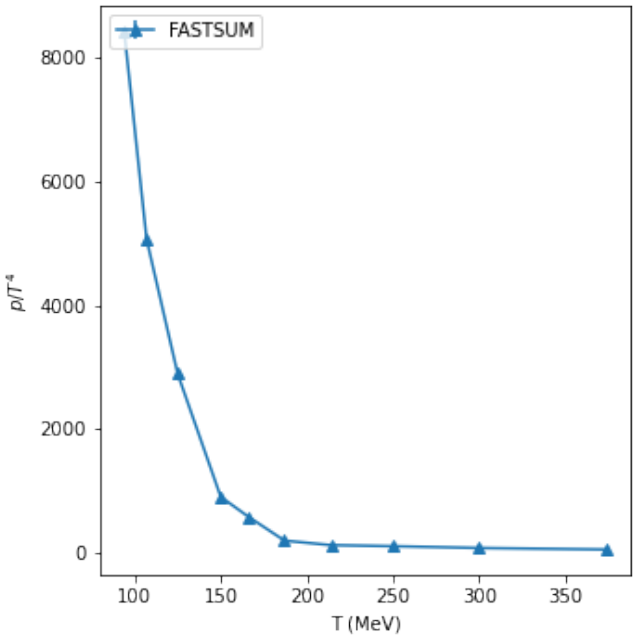

(a) Pressure vs temperature from the gluonic energy-momentum tensor, showing the data for all temperatures.

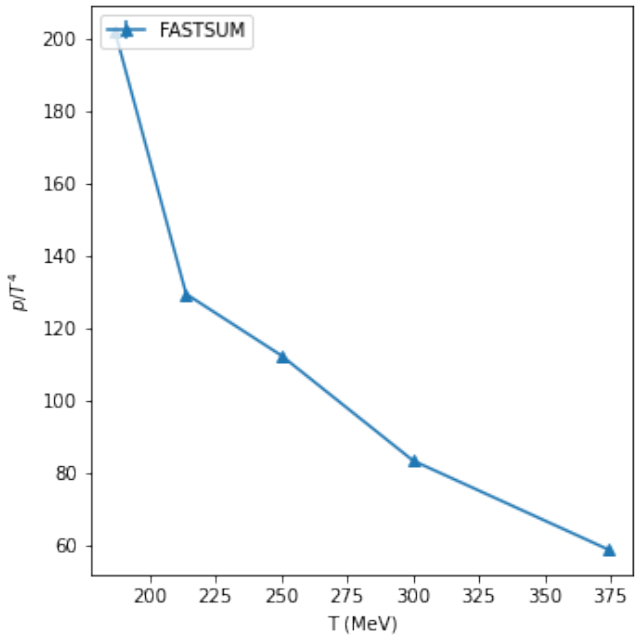

(b) Pressure vs temperature from the gluonic energy-momentum tensor, focusing on region of interest for comparison with Suzuki et al.

Fig. 4.15: Preliminary data for the pressure as a function of temperature. These values were extrapolated using eq. (4.20) with the coefficients set to $c_1 = c_2 = 1$. The errors within these plots are statistical only.

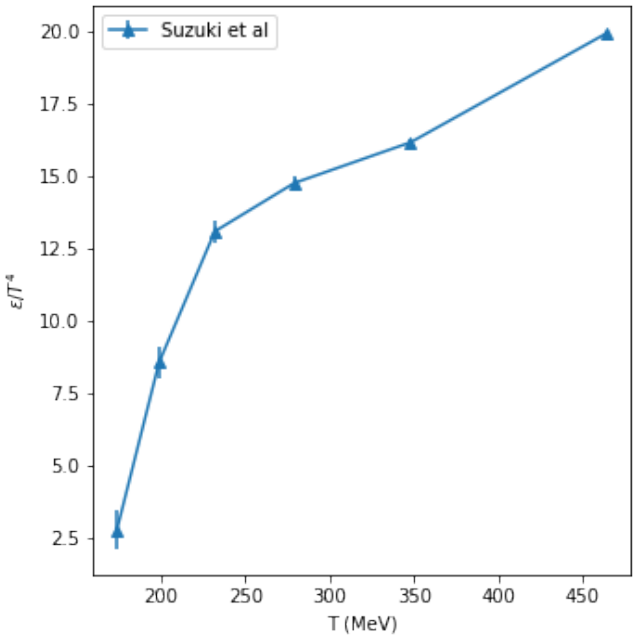

(a) Energy density vs temperature from the gluonic energy-momentum tensor, taken from the work of Suzuki et al.

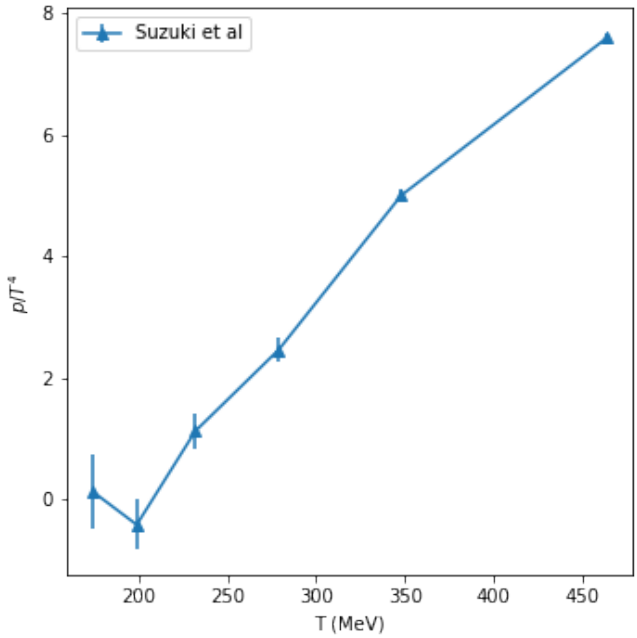

(b) Pressure vs temperature from the gluonic energy-momentum tensor, taken from the work of Suzuki et al.

Fig. 4.16: This data is taken from the work of Suzuki et al [76]. The errors included within these plots are statistical only.

N_t	T (MeV)	$\tau_{1/2}$	Gauge Configurations	Fermion Configurations
8	760	2	1048	-
12	507	4.5	1267	-
16	380	8	1102	-
20	304	12.5	1030	-
24	253	18	1016	-
28	217	24.5	274	-
32	190	32	1090	-
36	169	32	504	-
40	152	32	513	-
48	127	32	556	-
56	109	32	508	-
64	95	32	522	-
128	47	32	306	-

Table. 4.1: Temperature, maximum safe flow time $\tau_{1/2}$ and number of configurations for the FASTSUM Gen2L data, the parameters for which were specified within table 2.6. The temperatures are computed using $T = 1/(N_t a_t)$, where $a_t = 0.032459$ fm, and 1 fm $= 1/(197.3$ MeV).

4.2 Topological Susceptibility

T (MeV)	ϵ/T^4	R^2 for ϵ	χ^2_{dof} for ϵ	p/T^4	R^2 for p	χ^2_{dof} for p
760	-	-	-	-	-	-
507	-	-	-	-	-	-
380	-44.685(0.001)(2.6)	0.985	0.003	58.850(0.002)(3.2)	0.986	0.004
304	-64.980(0.003)(2.6)	0.966	0.019	83.444(0.004)(3.0)	0.969	0.022
253	-77.726(0.007)(1.8)	0.992	0.001	97.268(0.007)(2.2)	0.993	0.001
217	-105.730(0.05)(1.8)	0.990	0.0005	126.132(0.05)(2.1)	0.991	0.0005
190	-181.428(0.03)(2.0)	0.995	0.0006	202.279(0.03)(2.3)	0.995	0.0007
169	-566.649(0.14)(7.8)	0.988	0.013	589.189(0.14)(7.9)	0.989	0.013
152	-902.101(0.15)(9.9)	0.994	0.007	909.305(0.14)(9.9)	0.994	0.007
127	-2896.963(0.3)(42)	0.960	1.047	2898.154(0.3)(42)	0.960	1.042
109	-5073.225(0.5)(69)	0.986	0.223	5068.122(0.5)(69)	0.986	0.221
95	-8447.333(0.8)(115)	0.986	0.369	8431.767(0.8)(115)	0.986	0.367
47	-	-	-	-	-	-

Table. 4.2: Energy density ϵ, and pressure p, as functions of temperature for the FASTSUM Gen2L data, the parameters for which were specified within table 2.6. The temperatures are computed using $T = 1/(N_t a_t)$, where $a_t = 0.032459$ fm, and 1 fm $= 1/(197.3$ MeV). The first error is statistical and the second is systematic. The goodness of fit parameters R^2 and χ^2_{dof} are included for both the energy density and pressure data. The data for $T = 47$ MeV has been omitted as it was used as the zero temperature data point in order to compute the vacuum expectation value required for eq. (4.20).

Topological susceptibility is a very interesting quantity owing to the fact that it is relevant to both the strong CP problem and dark matter through its relation to the axion [93]. As such the topological susceptibility (χ_{top}) is of particular interest in cosmology [95–97]. In recent years there have been a number of lines of study using gradient flow on the lattice to compute χ_{top}, from those using domain wall fermions [98], staggered fermions [99], to those using reweighting [100, 105]. There is also work done without flow using fermionic methods based on the Atiyah-Singer index theorem [101]. More work in this area can be found in [102, 103]. A recent review of topological studies on the lattice can be found in [104].

One of the motivating factors for including this work is to inquire as to whether there may be any particular benefit in computing χ_{top} using the anisotropic lattice setup with $N_f = 2 + 1$ Wilson type quarks. Moreover it offers an opportunity to demonstrate the use of the gradient flow on an anisotropic lattice for an observable not related to the energy-momentum tensor.

Following the work of [93], the topological charge density is defined by;

$$q(x,\tau) = \frac{1}{64\pi^2}\epsilon_{\mu\nu\rho\sigma}G^a_{\mu\nu}(x,\tau)G^a_{\mu\nu}(x,\tau), \tag{4.61}$$

where $\epsilon_{0123} = 1$ and the topological charge $Q(\tau)$ is then given as;

$$Q(\tau) = \int d^4x q(x,\tau). \tag{4.62}$$

The topological susceptibility is then given by;

$$\chi^G_{top} = \frac{1}{V_4}(< Q^2 > - < Q >^2), \tag{4.63}$$

with V_4 being the four-volume, and the superscript G making explicit the use of the gauge definition rather than the fermionic definition. In order to extrapolate a value for χ^G_{top} it is necessary to take the $\tau \to 0$ limit, however this can only be done for that data which shows a clear plateau within the safe maximum flow time $\tau_{1/2}$ in order to prevent contamination from lattice artifacts.

The statistical errors within χ^G_{top} are determined by using the Jackknife method directly for the difference specified in eq. (4.63). The extrapolation within the fiducial window is then performed using a linear regression with a generalised least squares (GLS) fit, which is considered appropriate due to the correlation within the data. The correlation coefficient used within the GLS fit is estimated using an initial ordinary least squares fit.

The statistical errors on the final extrapolated result are then determined by repeating this extrapolation for both the upper and lower error bounds across all data points. These two values agree to close to machine precision, and thus the larger of the two values is then taken to be the symmetric error value. The values of topological susceptibility at lower temperature were computed on larger lattices, and thus were constructed with fewer configurations, leading to larger statistical error than those values at higher temperatures.

In principle any value within the plateau may be taken as the result for χ^G_{top} provided that the gradient within the plateau is exactly zero. However in practice there will remain a small non-zero gradient and thus it is not suitable to select a single arbitrary data point from within the plateau. One method for dealing with this would be to take the mean value from all data points within the plateau with the systematic error being taken as the standard deviation of the distribution within the fiducial window. However this approach does not account for the correlation between the data points within the plateau, or for the fact that the resultant χ^G_{top} value should be taken for $\tau = 0$, which may differ from the average value within the plateau based on the size of the plateau's gradient. The results of this method are included within this section for comparison with the results from the GLS fit.

The approach taken within this work for determining the overall value of χ^G_{top} with both statistical and systematic errors, is to compute the statistical error as stated above, using the GLS fit to extrapolate to $\tau = 0$, and repeating this for various choices of the fiducial window (plateau), with the systematic error then being taken as the standard deviation of the resultant normal distribution.

Results

T (MeV)	χ^G_{top} (GeV^4)	Plateau Gradient	χ^2_{dof}	Plateau Mean
760	-	-	-	-
507	-	-	-	-
380	-	-	-	-
304	-	-	-	-
253	-	-	-	-
217	-	-	-	-
190	-	-	-	-
169	1.050(3)(17) 10^{-5}	3.61 10^{-10}	1.175 10^{-10}	1.053(2) 10^{-5}
152	1.455(4)(10) 10^{-5}	1.14 10^{-8}	3.128 10^{-11}	1.477(3) 10^{-5}
127	1.668(4)(2) 10^{-5}	2.32 10^{-10}	2.446 10^{-12}	1.668(1) 10^{-5}
109	1.726(5)(10) 10^{-5}	6.64 10^{-9}	1.945 10^{-11}	1.740(2) 10^{-5}
95	1.711(4)(18) 10^{-5}	-6.71 10^{-10}	6.028 10^{-11}	1.711(3) 10^{-5}
47	1.574(8)(14) 10^{-5}	2.17 10^{-8}	1.617 10^{-11}	1.614(8) 10^{-5}

Table. 4.3: Topological susceptibility using the gauge χ^G_{top} definition, for various temperatures using the FASTSUM Gen2L configurations. The first error on χ^G_{top} is statistical and the second is systematic. The plateau gradient is included to specify the flatness of the data within the plateau. The chi-squared per degree of freedom χ^2_{dof}, is included as the goodness of fit parameter. The plateau mean is the mean value within the fiducial window, and its systematic error was taken as the standard deviation of the values within the fiducial window.

Those lattices of $N_t = 32$ (fig. 4.20b) and below, corresponding to temperatures 190 MeV and above, did not present a clear plateau within the safe flow time as defined within eq. (4.41). This is somewhat surprising upon first glance as one of the purported benefits of the anisotropic lattice over its isotropic counterpart is a superior sampling in the temporal direction which here corresponds to temperature. In particular when using gradient flow this should in principle mean that due to the smallest viable value of N_t being at a higher temperature than for the isotropic lattice, that a meaningful plateau should be present up to higher temperatures. However this assumes that the rate at which a plateau is reached with respect to flow time is equal, which does not appear to be the case. Within the comparative work of Suzuki et al [93], the smallest lattice with a usable plateau within the safe flow time was $N_t = 10$, corresponding to $T = 279$ MeV. For the FASTSUM Gen2L configurations the smallest viable lattice was for $N_t = 36$, corresponding to $T = 169$ MeV. With this said however, it is not yet possible to draw a conclusion regarding whether the anisotropic lattice holds an advantage within studies of χ^G_{top} when using gradient flow, as these simulations are performed at different lattice spacing's and pion masses. Ideally these variables would have been set to match those of Suzuki et al's work, however the FASTSUM Gen2L configurations were not tuned with such studies in mind. It is anticipated that as later generations of configurations become available, the higher temperatures may well obtain a plateau within a shorter flow time, permitting safe extrapolation, however this remains to be seen at a later date.

Comparing the safely obtained results in fig. 4.24 it is clear that the results agree at near zero temperature. It would also be tempting to state that the error for the FASTSUM data is under better control, given that the statistics are similar for the two studies. Likewise it is also interesting

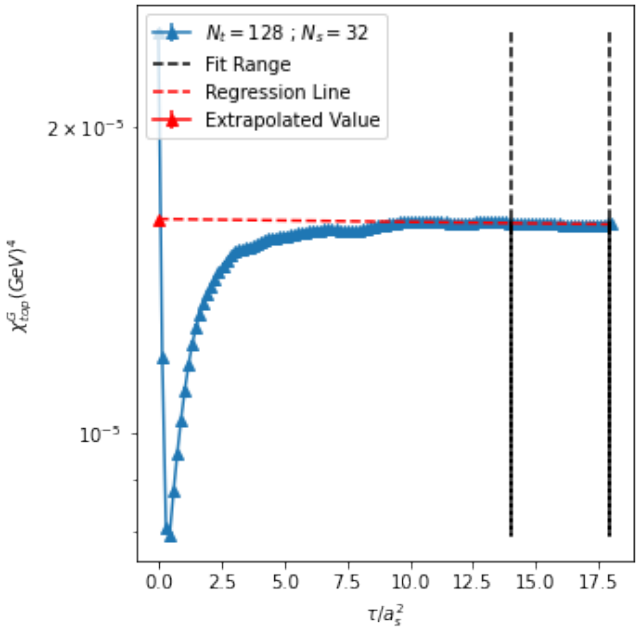

(a) Data for the N_t x $N_s^3 = 128$ x 32^3 ensemble, corresponding to a temperature of $T = 47$ MeV.

Fig. 4.17: Topological susceptibility from the gauge definition $\chi^G_{top}(x, \tau)$, as a function of flow time τ/a_s^2.

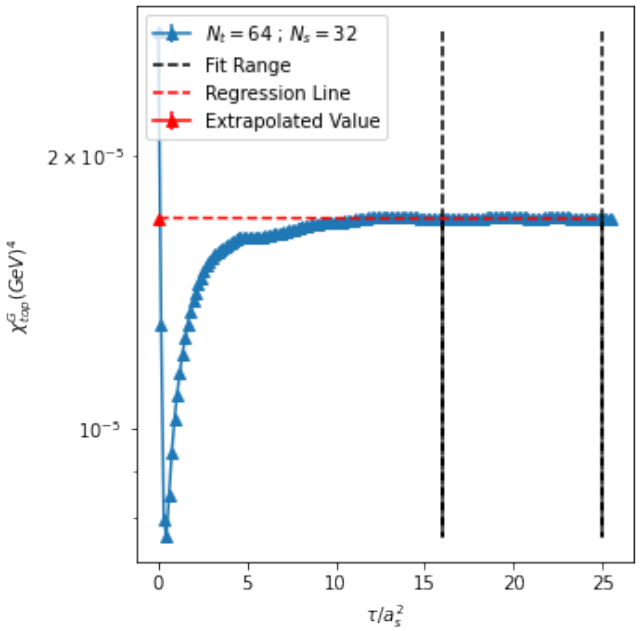

(a) Data for the N_t x $N_s^3 = 64$ x 32^3 ensemble, corresponding to a temperature of $T = 95$ MeV.

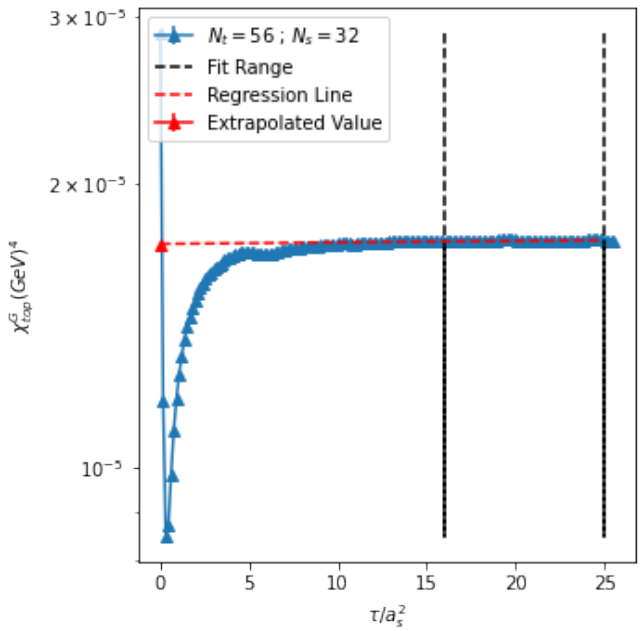

(b) Data for the N_t x $N_s^3 = 56$ x 32^3 ensemble, corresponding to a temperature of $T = 109$ MeV.

Fig. 4.18: Topological susceptibility from the gauge definition $\chi^G_{top}(x, \tau)$, as a function of flow time τ/a_s^2.

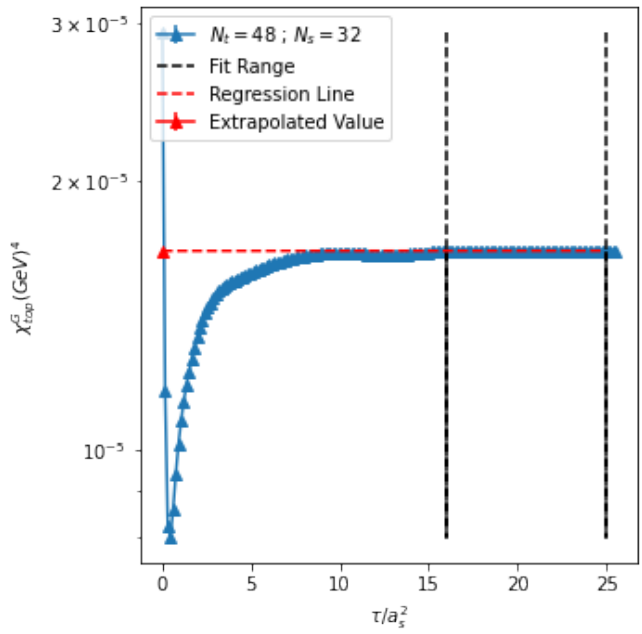

(a) Data for the N_t x $N_s^3 = 48$ x 32^3 ensemble, corresponding to a temperature of $T = 127$ MeV.

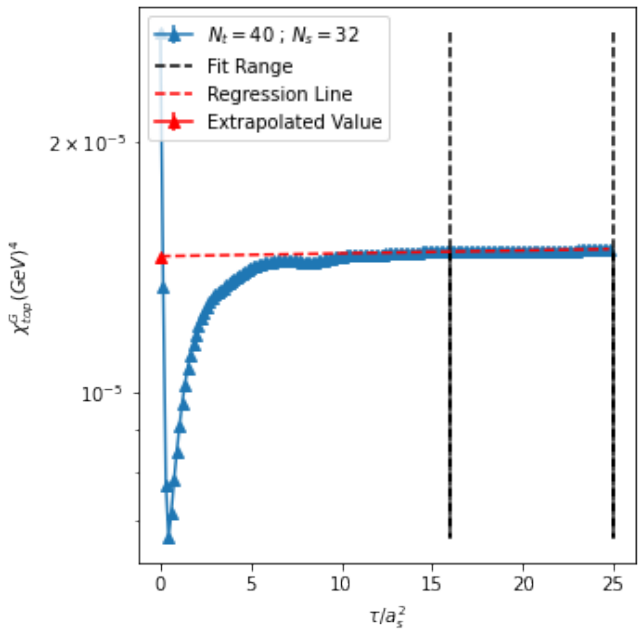

(b) Data for the N_t x $N_s^3 = 40$ x 32^3 ensemble, corresponding to a temperature of $T = 152$ MeV.

Fig. 4.19: Topological susceptibility from the gauge definition $\chi^G_{top}(x, \tau)$, as a function of flow time τ/a_s^2.

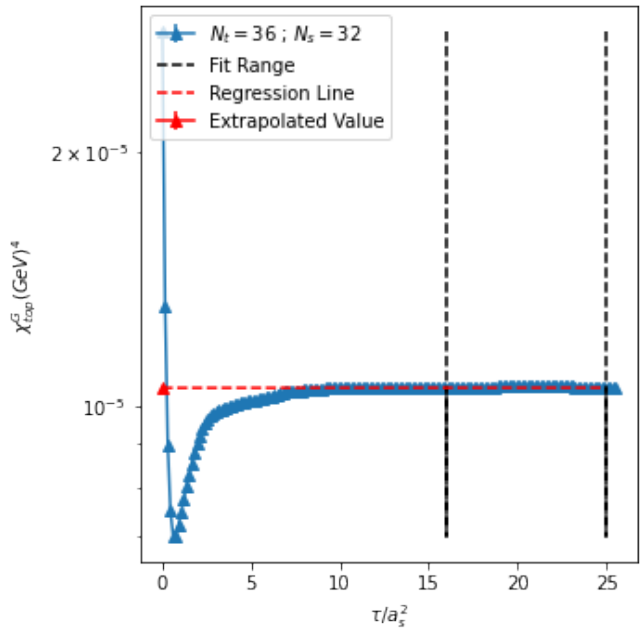

(a) Data for the N_t x $N_s^3 = 36$ x 32^3 ensemble, corresponding to a temperature of $T = 169$ MeV.

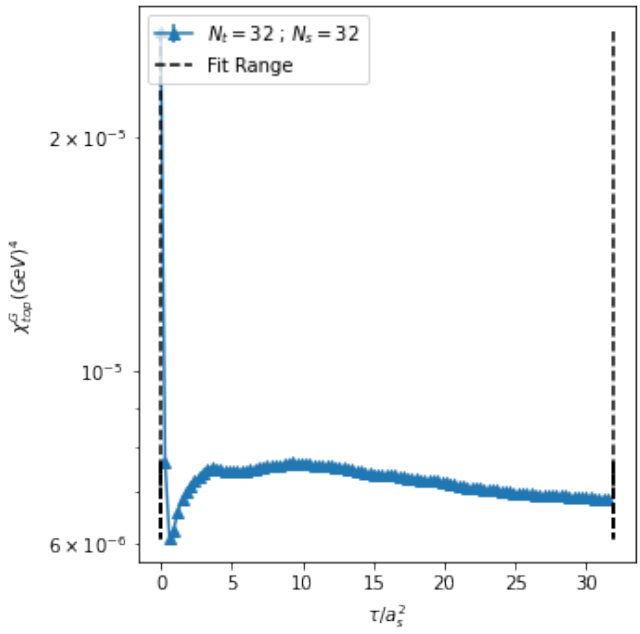

(b) Data for the N_t x $N_s^3 = 32$ x 32^3 ensemble, corresponding to a temperature of $T = 190$ MeV.

Fig. 4.20: Topological susceptibility from the gauge definition $\chi^G_{top}(x, \tau)$, as a function of flow time τ/a_s^2.

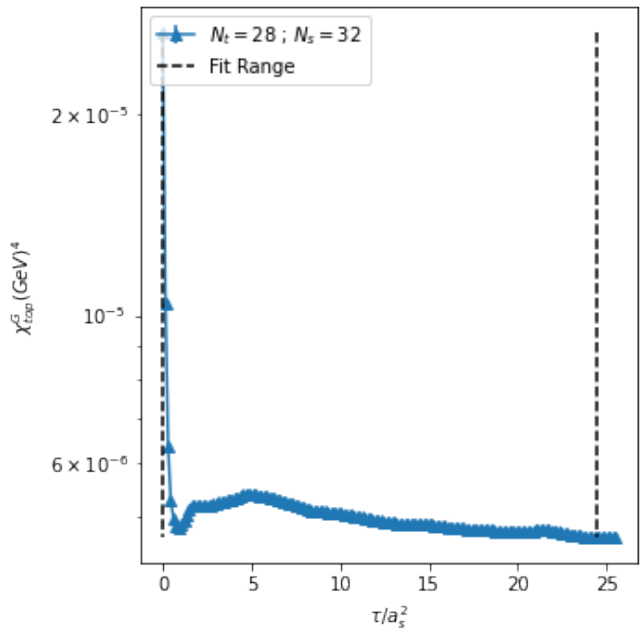

(a) Data for the N_t x $N_s^3 = 28$ x 32^3 ensemble, corresponding to a temperature of $T = 217$ MeV.

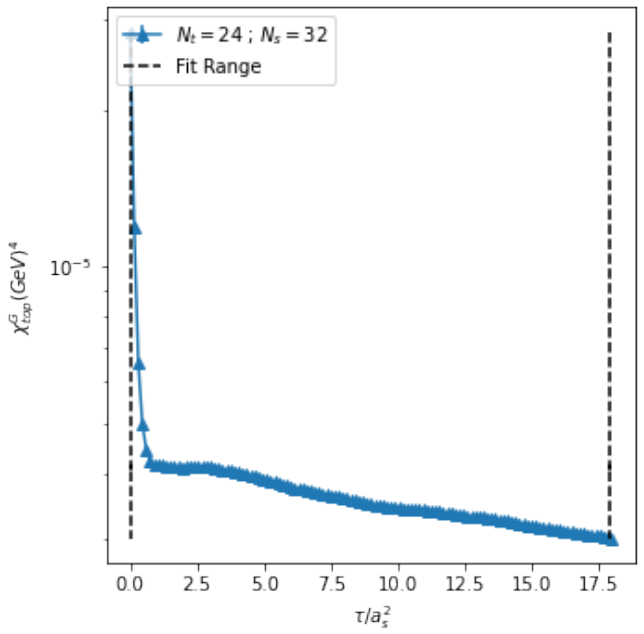

(b) Data for the N_t x $N_s^3 = 24$ x 32^3 ensemble, corresponding to a temperature of $T = 253$ MeV.

Fig. 4.21: Topological susceptibility from the gauge definition $\chi^G_{top}(x, \tau)$, as a function of flow time τ/a_s^2.

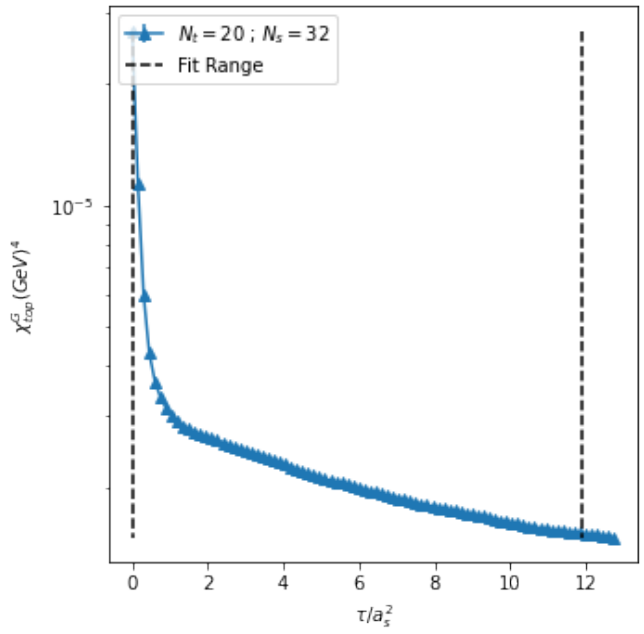

(a) Data for the N_t x $N_s^3 = 20$ x 32^3 ensemble, corresponding to a temperature of $T = 304$ MeV.

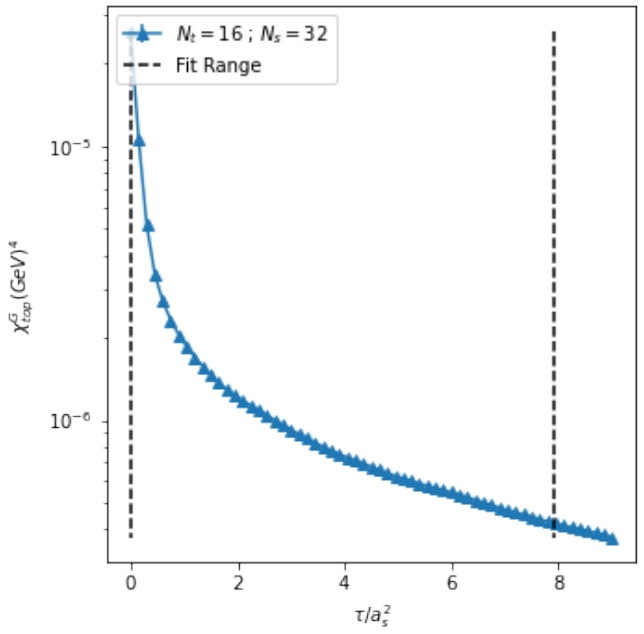

(b) Data for the N_t x $N_s^3 = 16$ x 32^3 ensemble, corresponding to a temperature of $T = 380$ MeV.

Fig. 4.22: Topological susceptibility from the gauge definition $\chi^G_{top}(x, \tau)$, as a function of flow time τ/a_s^2.

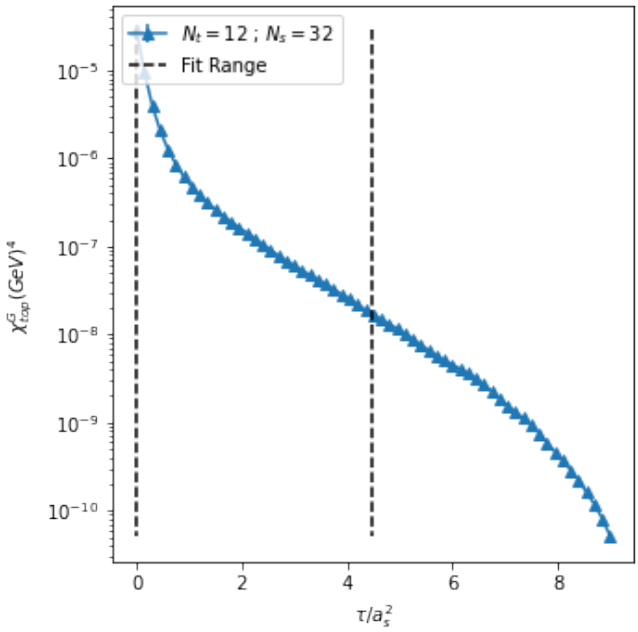

(a) Data for the N_t x $N_s^3 = 12$ x 32^3 ensemble, corresponding to a temperature of $T = 507$ MeV.

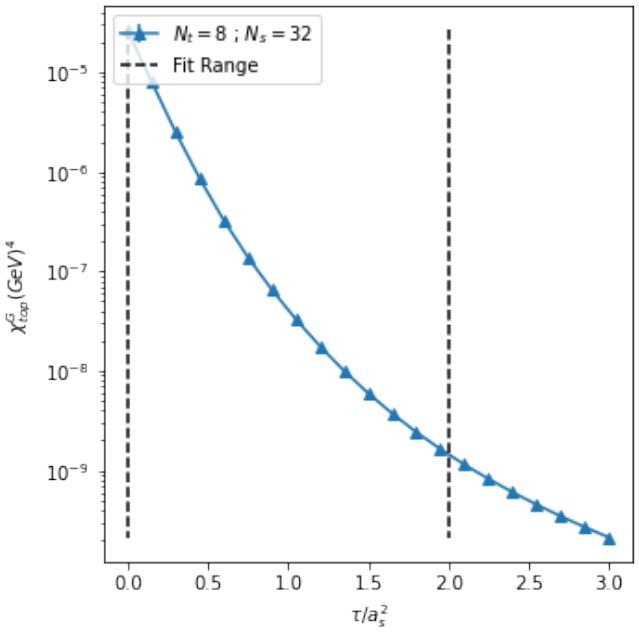

(b) Data for the N_t x $N_s^3 = 8$ x 32^3 ensemble, corresponding to a temperature of $T = 760$ MeV.

Fig. 4.23: Topological susceptibility from the gauge definition $\chi^G_{top}(x, \tau)$, as a function of flow time τ/a_s^2.

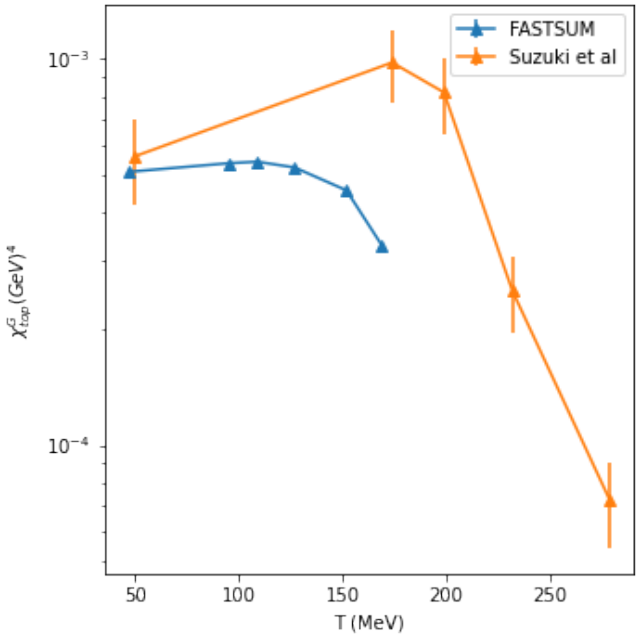

(a) χ^G_{top} vs T.

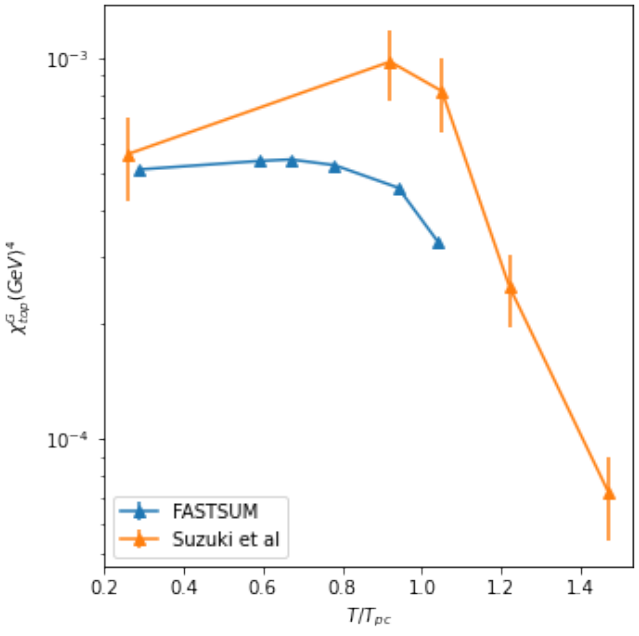

(b) χ^G_{top} vs T/T_{pc}.

Fig. 4.24: Topological susceptibility vs temperature for the FASTSUM Gen2L ensembles and comparison against the work of Suzuki et al [93]. The work of Suzuki et al has a value $T_{pc} = 190$ MeV, with the FASTSUM Gen2L value being $T_{pc} = 162$ MeV.

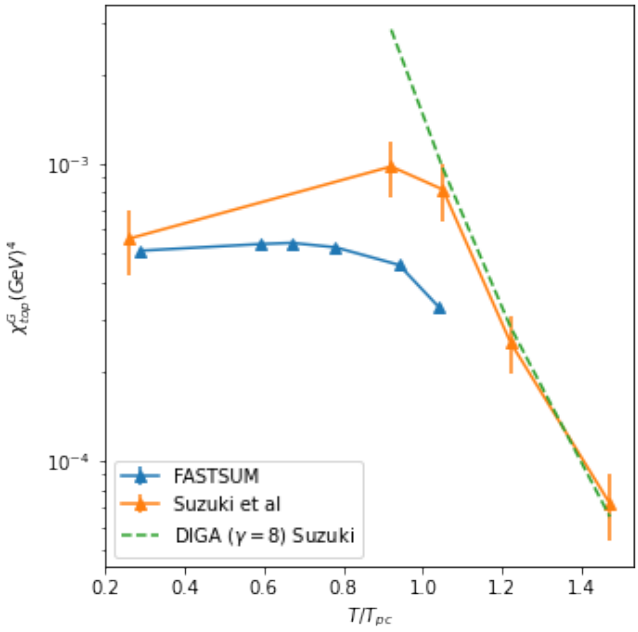

(a) χ^G_{top} vs T/T_{pc}. The Suzuki data is shown to roughly agree with the dilute instanton gas approximation (DIGA) at around $> T_{pc}$. The FASTSUM data does not extend to high enough temperatures to show agreement with the DIGA.

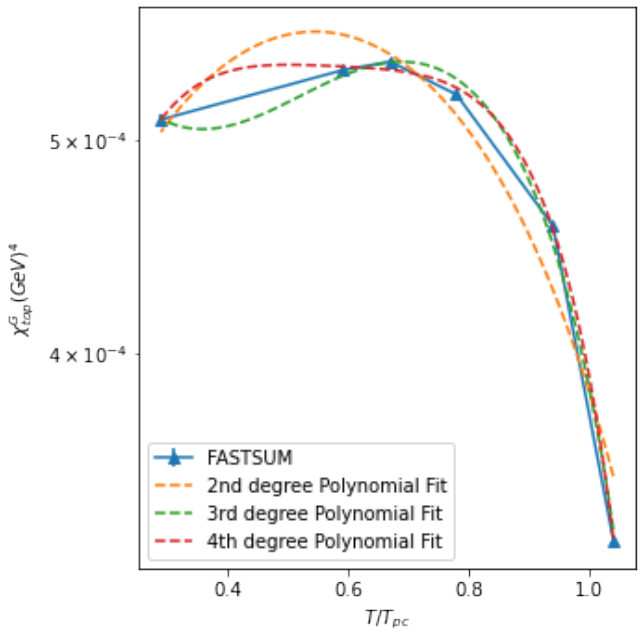

(b) χ^G_{top} vs T/T_{pc}. The FASTSUM data below approximately T_{pc} is not described by the power law decay of the DIGA, but rather is described as a more complex polynomial.

Fig. 4.25: Topological susceptibility vs temperature for the FASTSUM Gen2L ensembles and comparison against the work of Suzuki et al [93], including fits.

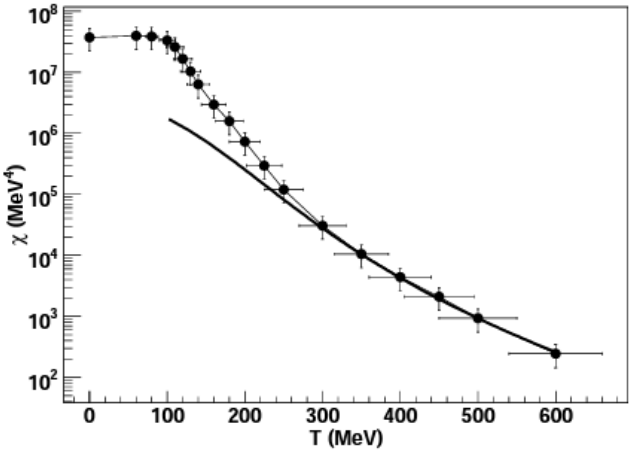

(a) Topological susceptibility vs temperature computed using the interacting instanton liquid model. The trend shows agreement with the dilute instanton gas model at large temperatures ($T > 300$ MeV), and an approximate plateau at lower temperatures ($T < 100$ MeV).

Fig. 4.26: The figure is taken from fig.23 of [94], where the behaviour of χ^G_{top} vs T is understood in terms of the population of bonded and unbonded instantons.

to highlight that the peak in χ^G_{top} appears to occur at a lower temperature, at around $\sim 0.6-0.7\ T_{pc}$ vs Suzuki's $\sim 0.9\ T_{pc}$. However unfortunately no significance can yet be drawn from such a comparison precisely due to the difference in lattice spacing and pion mass. What can be said however, is that the anisotropic lattice appears to give a reasonable and well controlled result for χ^G_{top} at $\leq T_{pc}$, with the difference with respect to the literature being somewhat typical for the level of variation seen with the topological susceptibility. The values from the extrapolations are presented within table 4.3, including the goodness of fit parameter χ^2_{dof} and the gradient of the plateau within the fiducial window. All of the fiducial windows used for extrapolation demonstrate a very small gradient and a very small χ^2_{dof}, suggesting a well controlled extrapolation. The statistical error was consistently around the sub-percent level with the systematic error being on the percent level. The values obtained by taking the mean topological susceptibility within the fiducial window show good agreement to the sub-percent level for those plateau's with the smallest gradient and disagreement of a few percent for those which were less flat. This suggests that either method can be used providing that the anticipated sources of error are already at the percent level, with the extrapolation method being used when higher precision is required.

The interest in computing the topological susceptibility was largely due to the importance of its temperature dependence within cosmology, as the abundance of axion dark matter would be sensitive to the mass of the axion and thus to the temperature dependence of the topological susceptibility [95]. The safely extrapolated data is shown again within fig. 4.25a along with Suzuki et al's work, this time with data based on the dilute instanton gas model (DIGA). The DIGA is suggested to describe the temperature dependence of the topological susceptibility at a sufficiently high temperature with three quark flavours, namely;

$$\chi^G_{top} \propto \left(\frac{T}{T_{pc}}\right)^{-\gamma}, \tag{4.64}$$

where $\gamma = 8$ for the DIGA. It is clear from the figure that whilst the work of Suzuki et al demonstrates agreement with the DIGA for temperatures just above T_{pc}, no such agreement is found for the safely extrapolated FASTSUM data. The FASTSUM data does however show agreement with the low temperature results from the interacting instanton liquid model (IILM), as shown within fig. 4.26a. The slight peak with an approximate plateau, combined with the well controlled errors, would suggest that the peak seen within the work of Suzuki er al is not physical and will likely vanish with improved data. A key objective within the work presented in this section was to improve upon the knowledge of the topological susceptibility as a function of temperature for full $N_f = 2+1$ QCD. Unfortunately the configurations used within this work were generated at parameters for which a plateau is typically not available at low flow times, and thus the highly desired data at large temperature was not available.

Moreover the FASTSUM data suggests that the temperature dependence for $T < T_{pc}$ is instead approximately described according to a polynomial, as can be seen within fig. 4.25b. No specification is given for the parameters of said polynomials as their chi-squared per degree of freedom values were $\mathcal{O}(10^{-8})$, $\mathcal{O}(10^{-7})$ and $\mathcal{O}(10^{-6})$ for the fourth, third and second degree polynomials respectively, suggesting that with so few data points the trend is being over-fitted.

Chapter 5

Conclusions

The key objectives of this work were to try the new technology of the gradient flow on the FASTSUM Gen2L configurations so as to determine their suitability for thermodynamic studies, and to perform the first thermodynamic computations in $N_f = 2 + 1$ QCD on the anisotropic lattice, both of which have been achieved.

The gradient flow for the gauge fields has been implemented on the anisotropic lattice via the OpenQCD-FASTSUM code base. The gauge field gradient flow has been validated by bench-marking against the known value of the renormalised fermion anisotropy $\tilde{\gamma}_f$, and spatial lattice spacing a_s, for the Gen2L ensembles. The known value for $\tilde{\gamma}_f$ was previously computed using fermion dispersion methods, whilst the known a_s value was obtained by combining $\tilde{\gamma}_f$ with a_t, which was determined using a baryon mass fit. The values for $\tilde{\gamma}_g$ and a_s presented within this work were determined using the gradient flow on gauge fields. The obtained $\tilde{\gamma}_g$ value differed from the known $\tilde{\gamma}_f$ value by 1.13%, whilst the obtained a_s value differed by 8.32% from the previous value. Given the different approaches used for these calculations and the typical extent to which such gluonic and fermionic methods agree, the values obtained within this work are considered to be in agreement with the previous calculations. This also provided FASTSUM with an awareness of the extent to which these methods agree for their Gen2L configurations. Moreover the OpenQCD-FASTSUM code allows for these calculations to be performed more than twenty times faster than using the code of Borsanyi et al.

One of the key computations within this work was the determination of the topological susceptibility χ^G_{top}, via the gluonic definition using gradient flow. This provided the first insight into the suitability of the FASTSUM configurations to thermodynamic computations, and represents to the authors knowledge the first such computation for full $N_f = 2 + 1$ QCD using the anisotropic lattice. It was hoped that χ^G_{top} could be determined to sufficiently high temperatures so as to test the dilute instanton gas approximation in full QCD, which would help to assess the axion as a potential dark matter candidate. The topological susceptibility has been studied for $T = 0.29 \rightarrow 4.69\ T_{pc}$, representing temperatures from $T = 47 \rightarrow 760$ MeV. For the parameters used within the Gen2L configurations, the plateau required for the extrapolation of the desired result was present at surprisingly large

flow times. Consequently χ^G_{top} could only be computed as a function of temperature across the range $T = 0.29 \rightarrow 1.04\ T_{pc}$, which did not allow for comparison against the dilute instanton gas approximation, which is only valid from $T \geq 300$ MeV. Comparison against the interacting instanton liquid model showed good qualitative agreement at low temperatures $T \leq 100$ MeV, with a nearly constant χ^G_{top} down to $T = 47$ MeV. Comparison against the work of Suzuki et al which utilised an isotropic lattice for full QCD studies demonstrated good agreement at the lowest temperature $T \sim 47$ MeV, with the values for higher temperatures differing slightly. This disagreement cannot be taken too seriously as of yet due to the different lattice spacing and pion masses used within the two studies. Whilst the comparison to the literature for the anisotropic full QCD χ^G_{top} computation is promising at lower temperatures, the parameters used for the Gen2L configurations do not appear to be suitable for higher temperature studies, and thus if this research path is to be taken further it may be required for the FASTSUM collaboration to generate bespoke configurations for this computation. It was an unexpected insight that the required flow time would be so large compared to other research groups, and when analysing the next generation of configurations with different parameters it would be prudent to consider that this may be an inherent feature of the anisotropic lattice itself. The contribution of this work to the research community is the clear qualitative agreement for full QCD with the low temperature behaviour determined by the interacting instanton liquid model, whereas the work of Suzuki et al indicated an unexpected substantial peak within χ^G_{top} towards low temperatures which did not agree with the anticipated trend.

The other key computation within this work was the construction of the energy-momentum tensor on the anisotropic lattice using gradient flow, with the first steps being to use the expectation value to compute the energy density and pressure as functions of temperature. Given that this was the first application of the method outlined by Suzuki et al using an anisotropic lattice, and using the FASTSUM Gen2L configurations which were not tuned for such studies, only the gluonic contribution was studied with the determination of the fermionic contribution being left for a next step. It was discovered that the coupling for the Gen2L configurations was too strong to allow for the use of the perturbatively determined coefficients within the method of Suzuki et al. One of the reasons for selecting this method over its competitors was the straightforward nature of its application. The requirement to non-perturbatively determine the coefficients used within this method substantially increases the workload for its use. Without direct access to the required coefficients it was not possible to perform a final analysis of the gluonic contribution to the energy density and pressure. A partial analysis was thus performed within this work, with the coefficients set to unity, using the data that was available. Whilst the trend in flow time for both of these observables is expected to differ considerably with the inclusion of the correct coefficients, it was nevertheless insightful to perform the same analysis with the available data. The energy density and pressure were studied for $T = 0.59 \rightarrow 4.69\ T_{pc}$, with the required signal for extrapolation being present for all but the two smallest lattices, resulting in data in the range $T = 0.59 \rightarrow 3.25\ T_{pc}$. Once more the required signal within the data for extrapolation is present at large flow times, and whether this is due to the parameters of the configurations or the anisotropic lattice itself is not yet clear. The presence of well linear regions within the data is encouraging that such a trend may likely be present when the

full analysis is performed with the non-perturbative coefficients. The resultant trends in the energy density and pressure as functions of temperature were completely non-physical, however it should be explicitly stated that there is no reason to expect the results to be physical in the absence of the correct coefficients. No meaningful comment can yet be made about comparing the results of this partial analysis to the literature. The only way to progress past this level of analysis is to perform the work of non-perturbatively determining the coefficients. One of the key insights of this work was that once again for the anisotropic lattice with the Gen2L configurations, the required flow times are considerably larger than those seen in previous studies. This could prove to be a useful insight also to the wider research community when designing their own similar research programs. In order to understand whether this is a characteristic of the anisotropic lattice or the Gen2L data, this analysis will be repeated on the next generations of data. The FASTSUM group has now become aware that in order to perform their desired future studies of transport properties using the energy-momentum tensor, they must compute the required coefficients non-perturbatively. It should be understood that whilst the method of Suzuki et al has not been as simple in application as was anticipated due to the strong coupling, that the alternative methods themselves also require substantial work in order to utilise. It is not yet possible to determine whether this method is the most suitable candidate for anisotropic lattice studies, as the difficulty in performing the determination of the coefficients must be understood, and the long flow time requirement must be laid at the feet of either the anisotropic lattice or the Gen2L data.

The initial key objectives to try the new technology of the gradient flow on the FASTSUM Gen2L configurations so as to determine their suitability for thermodynamic studies, and to perform the first thermodynamic computations in full $N_f = 2+1$ QCD on the anisotropic lattice, have been achieved, however this presents an initial exploratory investigation into these areas and a substantial research program lies ahead. Within the work presented in this thesis the FASTSUM Gen2L configurations have been explored for the purpose of thermodynamic investigations, including the topological susceptibility and the expectation value of the energy-momentum tensor. The first full QCD study of these quantities has also been performed using an anisotropic lattice. The key next steps for the energy-momentum tensor are to non-perturbatively determine the required coefficients, to compute the fermion contribution, and to compute correlation functions. This analysis must also be performed on new generations of data in order to understand the high flow time required to obtain the desired signals within the data. The topological susceptibility must also be analysed on new generations of data in order to again understand the pattern of requiring large flow times to obtain the required signal, and to determine whether a different parameter set will allow access to the determination of χ^G_{top} at larger temperatures for comparison against the dilute instanton gas approximation.

Appendices

Appendix A - Chiral Symmetry

All fermions are represented by a 4-component Dirac spinor, whose elements can be decomposed into two Weyl spinors, which each represent a different chirality. There are four such spinors for each type of particle, which are the solutions to the Dirac equation, describing how spin-1/2 particles evolve in time. For example, for a massless electron there exist two particle solutions and two anti-particle solutions, each of which have a left chiral and a right chiral variant. These four spinors are strictly speaking distinct particles, and they have unique quantum numbers and thus behave distinctly within experiment. The time evolution of the spinors takes the form $e^{\pm imt}$, with t time and m mass. This is crucial because massive particles thus necessarily change chirality, even in the absence of any interactions, and are typically in some linear combination of left and right chirality. The material within this section follows the content within [35, 36].

The statement that a particle is left chiral or right chiral is a statement about whether the particle behaves as though it is described using a left handed or a right handed coordinate system. This was shown by Wu to be a meaningful distinction, as only left handed particles transform non-trivially under the $SU(2)_L$ weak interactions . A more sophisticated description would be to state that particles with different chirality transform under different representations of a given group[1], however it still comes down to whether the coordinate system for describing the particles behaviour is left handed or right handed.

The strong and electromagnetic interactions may be agnostic to the chirality of a given particle, but in order to describe the weak interactions it must be possible to project a given massive Weyl spinor from its general mixture of left and right chirality into a definite left chirality. The projection operators $P_{L,R}$ which project to a state of pure left and right handedness respectively, are given by;

$$\psi_{L,R} = \frac{1}{2}(1 \pm \gamma_5)\psi = P_{L,R}\psi, \tag{1}$$

where the chirality operator γ_5 is defined as;

$$\gamma_5 = i\gamma_0\gamma_1\gamma_2\gamma_3. \tag{2}$$

In general terms a particle exhibits chiral symmetry if it is invariant under any transformation of the chiral symmetry group;

$$U(N_f)_L \times U(N_f)_R \simeq U(N_f)_V \times U(N_f)_A, \tag{3}$$

where the vector component $U(N_f)_V$ represents performing the same transformation simultaneously on left and right chiral particles, whilst the axial component $U(N_f)_A$ represents acting differently on each chirality. This can then be decomposed into the direct product of subgroups;

[1] A representation is a map from the group manifold to a space of linear transformations acting on vectors. See [36] for further details.

$$\begin{aligned} U(N_f)_L \times U(N_f)_R &\simeq SU(N_f)_L \times SU(N_f)_R \times U(1)_L \times U(1)_R \\ &\simeq SU(N_f)_V \times SU(N_f)_A \times U(1)_V \times U(1)_A. \end{aligned} \tag{4}$$

Transformations of Weyl spinors under this full chiral symmetry group then take the form;

$$U(1)_V : \psi_{L,R} \to e^{i\alpha}\psi_{L,R}, \tag{5}$$

for the vector component of the unitary transformations and;

$$U(1)_A : \psi_{L,R} \to e^{\pm i\alpha}\psi_{L,R}, \tag{6}$$

for the axial component, where in each case α is simply a real number and thus these transformations amount to changes by some phase factor. Note that in the axial case, the left and right handed fields experience a different phase angle. For the special unitary part of the chiral symmetry, the transformations take the form;

$$SU(N_f)_V : \psi_{L,R} \to e^{i\lambda}\psi_{L,R}, \tag{7}$$

for the vector component of the chiral transformations and;

$$SU(N_f)_A : \psi_{L,R} \to e^{\pm i\lambda}\psi_{L,R}, \tag{8}$$

for the axial component of the transformations. The λ in this case is just an $SU(N)$ matrix where $N = N_f$, built in the usual way from a linear combination of basis states, and thus the transformation takes on the form of an $N_f \times N_f$ matrix.

Interestingly in nature the $U(1)_A$ symmetry only exists on the classical level, or in other words, it only appeared to be a symmetry of QCD before using a more thorough framework. The $U(1)_A$ symmetry is broken due to quantum effects, which is an example of what is called anomalous symmetry breaking, where a symmetry that appeared to exist under classical mechanics disappears under a quantum description. This particular example of an anomalous symmetry breaking also goes by the name of the axial anomaly, given that it is the axial part of the symmetry (or atleast of the unitary part $U(1)_V \times U(1)_A$) which is anomalously broken. The remaining chiral symmetry in nature that could in principle be observed is then;

$$U(N_f)_L \times U(N_f)_R \to SU(N_f)_V \times SU(N_f)_A \times U(1)_B, \tag{9}$$

where the notation $U(1)_V \equiv U(1)_B$ is often used to denote that the conserved quantity associated under Nöether's theorem to the unitary vector part of the chiral symmetry is the baryon number.

Alas this is still not the chiral symmetry observed in nature. As the early universe expanded the energy density decreased, and thus the coefficients of the Higgs potential, whose values depend on the energy density, changed in such a manner as to result in electroweak symmetry breaking. The Higgs mechanism then resulted in the fermions, including the quarks, obtaining a mass. This is consequential for chiral symmetry because any mass term necessarily mixes left and right chiral fields in order to obey Lorentz invariance. Hence any mass term will by default break chiral symmetry given that the left and right handed fields are now explicitly coupled and thus can't be transformed independently, which is the essence of chiral symmetry. This particular form of symmetry breaking is called explicit symmetry breaking and appears on the level of the Lagrangian density. In other words there now exists an additional term within the Lagrangian which explicitly breaks the symmetry in question. In some sense, the term can be thought of as having always existed but with a value of zero, and after the electroweak symmetry breaking the term then has a non-vanishing value and thus the details of its chiral field mixing become important for whether or not the Lagrangian itself respects chiral symmetry overall.

In the context of QCD, if the non-zero quark masses are equal then the remaining chiral symmetry is;

$$U(N_f)_L \times U(N_f)_R \to SU(N_f)_V \times U(1)_V, \tag{10}$$

which is often rewritten as $SU(N_f)_V \times U(1)_V \equiv SU(N_f)_F \times U(1)_B$, where $SU(N_f)_F$ is used to denote that the conserved quantity under the special unitary vector part of the chiral symmetry is the flavour.

However in nature the quarks exhibit a clear hierarchy in mass, resulting in a further reduced chiral symmetry;

$$U(N_f)_L \times U(N_f)_R \to U(1)_u \times U(1)_d \times U(1)_s \times \cdots \times U(1)_{N_f}. \tag{11}$$

Interestingly though, since the mass of the up and down quarks are far below the $\Lambda_{\bar{M}S}$ scale, there still exists in nature an approximate global $SU(2)_L \times SU(2)_R$ symmetry, where isospin transformations act simultaneously on left and right handed fields $SU(2)_I \equiv SU(2)_V$. Similarly, since the mass of the strange quark is of the order of the $\Lambda_{\bar{M}S}$ scale, there also exists a lesser remnant of a global $SU(3)_L \times SU(3)_R$ symmetry which appears in the spectrum as an approximate flavour symmetry. In other words, although the universe currently exhibits explicit symmetry breaking, the effect on the lighter quarks in small enough that they can be thought of as being almost massless, and thus there is an approximate full chiral symmetry for the three light quarks ($N_f = 3$);

$$U(N_f)_L \times U(N_f)_R \to SU(N_f)_L \times SU(N_f)_R \times U(1)_B. \tag{12}$$

This is still not the full story however, as in addition to the anomalous chiral symmetry breaking

and the explicit chiral symmetry breaking (albeit with a remnant approximate symmetry surviving), there additionally exists a spontaneous chiral symmetry breaking where the symmetry is broken by the ground state itself. This is evidenced by the existence of the pseudo-scalar mesons within the spectrum, those being the Pions, Kaons and the η-meson. The Nambu-Goldstone theorem states that when a continuous global symmetry is broken by the ground state of the system, i.e. spontaneously broken, the spectrum thus exhibits massless Nambu-Goldstone bosons. The remnant full chiral symmetry that exists for the light quarks, $N_f = 3$, is spontaneously broken from eq. (12) down to;

$$SU(N_f)_L \times SU(N_f)_R \times U(1)_B \to SU(N_f)_F \times U(1)_B, \tag{13}$$

where again $SU(N_f)_F \equiv SU(N_f)_V$. The number of broken generators from the spontaneous symmetry breaking, in this case $N_f^2 - 1$, is equal to the number of Nambu-Goldstone bosons that appear in the spectrum. In the case of QCD, these are strictly speaking pseudo Nambu-Goldstone bosons given that they are not quite massless, which is due to the fact that the symmetry in eq. (12) is only approximate since the chiral symmetry was explicitly broken in the first place.

Spontaneous chiral symmetry breaking is a non-perturbative phenomenon and is studied on the lattice using the chiral order parameter, called the chiral condensate;

$$\begin{aligned} < \bar{\psi}\psi > &=< 0|\bar{\psi}(x)\psi(x)|0 > \\ &=< 0|\bar{\psi}_R(x)\psi(x)_L + \bar{\psi}_L(x)\psi(x)_R|0 > . \end{aligned} \tag{14}$$

The condensate is invariant under simultaneous transformation of left and right chiral fields, i.e. the vector component of the chiral symmetry, but not the axial component, and thus not under general chiral transformations. The chiral limit where spontaneous symmetry breaking is no longer present is signified by a vanishing value for the condensate, $< \bar{\psi}\psi >= 0$.

Appendix B - Renormalisation and the Λ_{QCD} scale

The following brief outline of the concept of effective field theory and renormalisation is taken from [106], to which the reader is directed for a more complete discussion.

The key idea of the Wilsonian renormalisation group is that the relevant degrees of freedom (or variables) that are required to describe the phenomena within a system are dependent on the energy (or length) scale at which the phenomena are being studied. In this sense the relevant degrees of freedom that capture the behaviour of condensed matter systems may be the atoms, those for nuclear physics are the nuclei, whereas those for QCD in the hadronic phase will be the hadrons and mesons but at higher energies the quarks and gluons must be used for a successful description of the system's behaviour. At low energies, the quarks and gluons do still matter, however their influence is simply to set the coupling constants and masses in the so called effective theory, within which the hadrons and mesons serve as the relevant degrees of freedom. In an effective theory the behaviour of the system under investigation is most naturally and efficiently described in terms of degrees of freedom that are defined at the same energy scale as which the behaviour under study occurs.

The effective theory is valid up to some energy (momentum) scale μ, beyond which the correct behaviour will only be described by a new effective theory which has new degrees of freedom defined at that new energy scale. The effective theory with degrees of freedom defined at scale μ may be used to describe behaviour considerably below this scale, however the description will no longer be efficient. An analogy would be attempting to use quantum field theory to describe a ball rolling down a hill; the information necessary may be at hand, but its far harder than using a more suitably selected mechanics framework.

The parameters of the effective theory at scale μ, such as the coupling constants and masses, will be determined by the specific properties of the more fundamental underlying theory at some higher energy scale $\mu^{'}$. The renormalisation group flow describes how these parameters at different energy scales are related to one another, and are typically described in terms of so called beta functions;

$$\beta_i(g_i) = \mu \frac{dg_i(\mu)}{d\mu}, \tag{15}$$

where g_i is the i'th coupling constant. The take home point is that the most fundamental description is perhaps not always the most pragmatic, and thus hydrodynamics may be preferable as a description in some situations rather than the underlying microscopic theory which would be QCD. Likewise, the theory that is being used to describe a system may in-fact only be an effective theory for some more fundamental, so called more microscopic theory.

For QCD, the relevant energy scale is $\mu = \Lambda_{QCD}$, the value for which depends on how many quark flavours are present in the system under study. Whether the renormalisation group flow can be used to relate the couplings at one scale to those at another is quite complicated, but in those circumstances where this is not possible, the theory is termed non-renormalisable. The QCD Lagrangian is

renormalisable despite potential non-renormalisable terms, because those terms are irrelevant at the low energies relevant to QCD. More specific details of renormalisation for QCD can be found within chapter 2 of [52].

Bibliography

[1] R. Morrin, et al, *Dynamical QCD simulations on anisotropic lattices*, Phys. Rev. D 74, 014505, 2006.

[2] R. Edwards, et al, *Tuning for Three-flavors of Anisotropic Clover Fermions with Stout-link Smearing*, arXiv:0803.3960, Phys.Rev.D78:054501, 2008.

[3] S. Aoki, et al, (CP-PACS Collaboration) *Charmonium Spectrum from Quenched Anisotropic Lattice QCD*, arXiv:hep-lat/0112020, Phys.Rev.D65:094508, 2002.

[4] P. Chen, *Heavy Quarks on Anisotropic Lattices: The Charmonium Spectrum*, arXiv:hep-lat/0006019, Phys.Rev. D64 (2001) 034509, 2000.

[5] T. Klassen, *Non-Perturbative Improvement of the Anisotropoc Wilson QCD Action*, arXiv:hep-lat/9809174, Nucl.Phys.Proc.Suppl. 73 (1999) 918-920.

[6] T. Klassen, *The Anisotropic Wilson Gauge Action*, arXiv:hep-lat/9803010v2, Nucl.Phys. B533 (1998) 557-575, 1998.

[7] S. Aoki, et al, (CP-PACS Collaboration), *Hybrid Quarkonia on Asymmetric Lattices*, arXiv:hep-lat/9812017, Phys.Rev.Lett. 82 (1999) 4396-4399.

[8] J. Harada, et al, *Heavy quark action on the anisotropic lattice*, arXiv:hep-lat/0203025, Phys.Rev. D66 (2002) 014509.

[9] C. Morningstar and M. Peardon, *The glueball spectrum from an anisotropic lattice study*, arXiv:hep-lat/9901004, Phys.Rev. D60 034509, 1999.

[10] T. Umeda, et al, (CP-PACS Collaboration), *Two flavours of dynamical quarks on anisotropic lattices*, arXiv:hep-lat/0302024, Phys.Rev. D68 034503, 2003.

[11] G. Aarts, et al, (FASTSUM Collaboration), *Hadron spectrum calculations in the quark-gluon plasma*, arXiv:1812.08151, PoS Lattice 2018.

[12] G. Aarts, et al, (FASTSUM Collaboration), *Charmonium at high temperature in two-flavour QCD*, arXiv:0705.2198, Phys.Rev.D76:094513,2007.

[13] G. Aarts, et al, (FASTSUM Collaboration), *The bottomonium spectrum at finite temperature from $N_f = 2 + 1$ lattice QCD*, arXiv:1402.6210 J. High Energ. Phys. 2014, 97 (2014).

[14] G. Aarts, et al, (FASTSUM Collaboration), *Lattice QCD at nonzero temperature and density*, arXiv:2111.10787, XXXII IUPAP Conference on Computational Physics 21, 2021.

[15] G. Aarts, et al, (FASTSUM Collaboration), *Meson thermal masses at different temperatures*, arXiv:2111.00784, PoS Lattice 2021.

[16] G. Aarts and A. Nikolaev (FASTSUM Collaboration), *Electrical conductivity of the quark-gluon plasma: perspective from lattice QCD*, arXiv:2008.12326 EPJA THOR, 2020.

[17] G. Aarts, et al, (FASTSUM Collaboration), *Properties of the QCD thermal transition with $N_f = 2 + 1$ flavours of Wilson quark*, arXiv:2007.04188, Phys.Rev.D 105 (2022) 3, 034504.

[18] G. Aarts, et al, (FASTSUM Collaboration), *News from bottomonium spectral functions in thermal QCD*, arXiv:1912.12900, PoS Lattice 2019.

[19] H. Suzuki, *Energy-momentum tensor on the lattice: recent developments*, arXiv:1612.00210, PoS Lattice 2016.

[20] E. Itou and Y. Nagai, *QCD viscosity by combining the gradient flow and sparse modeling methods*, arXiv:2110.13417, PoS Lattice 2021.

[21] E. Itou and Y. Nagai, *Sparse modeling approach to obtaining the shear viscosity from smeared correlation functions*, arXiv:2004.02426, JHEP 07 (2020) 007.

[22] Y. Taniguchi, et al, *Study of energy-momentum tensor correlation function in $N_f = 2 + 1$ full QCD for QGP viscosities*, arXiv:1901.01666, PoS Lattice 2018.

[23] E. Berkowitz, et al, *Lattice QCD input for axion cosmology*, arXiv:1505.07455, Phys. Rev. D 92, 034507 (2015).

[24] M. Tanabashi, et al, (Particle Data Group), *Review of Particle Physics*, Phys. Rev. D 98, 030001, 2018.

[25] D. Griffiths, *Introduction to Elementary Particles (Second, Revised Edition)*, Wiley-VCH Publishing, ISBN 978-3-527-40601-2, pp. 376 and 403, 2010.

[26] M. Gell-Mann, *The Eighfold Way: A Theory Of Strong Interaction Symmetry*, California Institute of Technology, 1961.

[27] G. t'Hooft and M. Veltman, *Regularization and renormalization of gauge fields*, Nuc.Phys.B, 44, 1, pp189-213, 1972.

[28] D. Gross and F. Wilczek, *Asymptotically Free Gauge Theories. I*, Phys.Rev.D8, 3633, 1973.

[29] D. Gross and F. Wilczek, *Reliable Perturbative Results for Strong Interactions?*, Phys.Rev.Lett, 30, 26, 1973.

[30] G. Gattringer and C.B. Lang, *Quantum Chromodynamics on the Lattice*, Springer, ISBN: 978-3-642-01850-3, 2010.

[31] I. Montvay and G. Münster, *Quantum Fields on a Lattice*, Cambridge University Press, ISBN 9780511470783, 1994.

[32] J. Schwichtenberg, *Physics From Finance*, ISBN 1795882417, 2020.

[33] G. Moore, *Informal Lectures on Lattice Gauge Theory*, Spring 2003, Accessed September 2021.

[34] S. Elitzur, *Impossibility of spontaneously breaking local symmetries*, Phys.Rev.D12, 3978, 1975.

[35] U. Wiese, *An Introduction to Lattice Field Theory*, 2009, Accessed Septer 2021.

[36] J. Schwichtenberg, *Physics From Symmetry*, ISBN: 978-3-319-66631-0, Springer, 2015.

[37] D. Tong, *Gauge Theory*, 2018, Accessed September 2021.

[38] D. Kaplan, *Chiral Symmetry and Lattice Fermions*, arXiv:0912.2560v2, 2012.

[39] P. Lepage, *Perturbative Improvement for Lattice QCD: An Update*, arXiv:hep-lat/9707026, Nucl.Phys.Proc.Suppl. 60A (1998) 267-278, 1997.

[40] M. Lüscher, *Implementation of the lattice Dirac operator*, 2012, Accessed September 2021.

[41] C. Morningstar and M. Peardon, *Analytic Smearing of SU(3) Link Variables in Lattice QCD*, arXiv:hep-lat/0311018, Phys.Rev. D69 (2004) 054501, 2003.

[42] M. Lüscher and P. Weisz, *On-shell Improved Lattice Gauge Theories*, Commim. Math. Phys. 97, 59-77, 1985.

[43] P. Lepage, *QCD for Coarse Lattices*, arXiv:hep-lat/9510049, Nucl.Phys.Proc.Suppl. 47 (1996) 3-16, 1995.

[44] P. Weisz, *Renormalization and lattice artifacts*, arXiv:1004.3462, 2010.

[45] Y. Iwasaki, *Renormalization Group Analysis of Lattice Theories and Improved Lattice Action. II – four-dimensional non-abelian SU(N) gauge model*, arXiv:1111.7054, 2011.

[46] R. Edwards, et al, *First results from 2+1 dynamical quark flavors on an anisotropic lattice: light-hadron spectroscopy and setting the strange-quark mass*, arXiv:0810.3588, Phys.Rev.D79:034502, 2009.

[47] R. Edwards, et al, *Coupled $\pi\pi$,$K\bar{K}$ scattering in P-wave and the ρ resonance from lattice QCD*, arXiv:1507.02599, Phys. Rev. D 92, 094502, 2015.

[48] R. Edwards, et al, *The quark-mass dependence of elastic πK scattering from QCD*, arXiv:1904.03188, Phys. Rev. Lett 123, 042002, 2019.

[49] S. Schaefer, *Simulations with the Hybrid Monte Carlo algorithm: implementation and data analysis*, 2009.

[50] M. Lüscher, *Algorithms used in ranlux v3.0, Martin Luscher*, 2001.

[51] M. Clark, *The Rational Hybrid Monte Carlo Algorithm*, arXiv:hep-lat/0610048, PoSLAT2006:004, 2006.

[52] K. Yagi, et al, *Quark-Gluon Plasma*, Cambridge University Press, ISBN: 9780521089241, Camb.Monogr.Part.Phys.Nucl.Phys.Cosmol. 23 1–446, 2005.

[53] M. Stephanov, *QCD phase diagram: an overview*, arXiv:hep-lat/0701002, PoSLAT2006:024, 2006.

[54] M. Atiyha and R. Bott, *The Yang-Mills Equations Over Riemann Surfaces*, doi: 10.1098/rsta.1983.0017, Phil. Trans. R. Soc. Lond. A 1983 308, 523-615.

[55] M. Lüscher, *Future applications of the Yang-Mills gradient flow in lattice QCD*, arXiv:1308.5598, 2013.

[56] S. Borsanyi, et al, *High-precision scale setting in lattice QCD*, arXiv:1203.4469, JHEP 1209 010, 2012.

[57] T. Hirakida, et al, *Themodynamics for pure SU(2) gauge theory using gradient flow*, arXiv:1805.07106, Progress of Theoretical and Experimental Physics, Volume 2019, Issue 3, March 2019, 033B01.

[58] M. Lüscher, P. Weisz, *Perturbative analysis of the gradient flow in non-abelian gauge theories*, arXiv:1101.0963, JHEP 1102:051, 2011.

[59] J. Dragos, et al, *Towards a determination of the nucleon EDM from the quark chromo-EDM operator with the gradient flow*, arXiv:1810.10301, PoS Lattice 2018.

[60] J. Dragos, et al, *Confirming the Existence of the strong CP Problem in Lattice QCD with the Gradient Flow*, arXiv:1902.03254, Phys. Rev. C 103, 015202 (2021).

[61] M. Lüscher *Trivializing maps, the Wilson flow and the HMC algorithm*, arXiv:0907.5491, Commun.Math.Phys.293:899-919,2010.

[62] J. Dragos, et al, *Expansion coefficient of the pseudo-scalar density using the gradient flow in lattice QCD*, arXiv:1811.11798, PoS Lattice 2018.

[63] G. Bergner, et al, *Study of thermal $SU(3)$ supersymmetric Yang-Mills theory and near-conformal theories from the gradient flow*, arXiv:1911.11575, PoS Lattice 2019.

[64] R. Narayanan and H. Neuberger, *Infinite N phase transitions in continuum Wilson loop operators*, arXiv:hep-th/0601210, JHEP0603:064,2006.

[65] R. Lohmayer and H. Neuberger, *Continuus smearing of Wilson Loops*, arXiv:1110.3522, PoS Lattice 2011.

[66] A. Ramos, *The Yang-Mills gradient flow and renormalization*, arXiv:1506.00118, 2015.

[67] M. Lüscher, *Properties and uses of the Wilson flow in lattice QCD*, arXiv:1006.4518, JHEP 1008:071, 2010.

[68] S. Borsanyi, et al, *Anisotropy tuning with the Wilson flow*, arXiv:1205.0781, 2012.

[69] S. Borsanyi, et al, *High precision scale setting on the lattice*, PoS Lattice 2021.

[70] L. Ludmila, et al, *Two-flavor QCD Thermodynamics using Anisotropic Lattices*, arXiv:hep-lat/0603031, Phys.Rev.D73:074504,2006.

[71] S. Borsanyi, et al, *QED and strong isospin corrections in the hadronic vacuum polarization contribution to the anomalous magnetoc moment of the muon*, arXiv:2202.05807, PoS Lattice 2021.

[72] F. Karsch, *SU(N) Gauge Theory Couplings on Asymmetric Lattices*, Nucl.Phys., B205:285–300, 1982.

[73] B. Svetitsky and F. Fucito, *Latent Heat of the SU(3) Gauge Theory*, Phys. Lett., B131:165, 1983.

[74] C. DeTar and U. Heller, *QCD Thermodynamics from the Lattice*, Eur.Phys.J., A41:405–437, 2009.

[75] T. Umeda, et al, *Fixed Scale Approach to Equation of State in Lattice QCD*, arXiv:0809.2842, Phys.Rev.D79:051501, 2009.

[76] H. Suzuki, et al, *Exploring $N_f = 2 + 1$ QCD theromodynamics from the gradient flow*, arXiv:1609.01417, Phys. Rev. D 96, 014509 (2017).

[77] M. Kitazawa, et al, *Thermodynamics and reference scale of $SU(3)$ gauge theory from gradient flow on fine lattices*, arXiv:1511.05235, PoS Lattice 2015.

[78] H. Suzuki, *Energy-momentum tensor from the Yang-Mills gradient flow*, arXiv:1304.0533, PTEP 2015 (2015) 079201.

[79] M. Kitazawa, et al, *Measurement of thermodynamics using gradient flow*, arXiv:1412.4508, PoS Lattice 2014.

[80] T. Iritani, et al, *Thermodynamics in quenched QCD: energy-momentum tensor with two-loop order coefficients in the gradient flow formalism*, arXiv:1812.06444, Prog Theor Exp Phys (2019).

[81] M. Asakawa, et al, (FlowQCD Collaboration), *Thermodynamics of $SU(3)$ Gauge Theory from Gradient Flow*, arXiv:1312.7492, Phys. Rev. D 90, 011501 (2014).

[82] H. Makino and H. Suzuki, *Lattice energy-momentum tensor from the Yang-Mills gradient flow – inclusion of fermion fields*, arXiv:1403.4772, PTEP 2015 (2015) 079202 .

[83] H. Suzuki, *Universal formula for the energy-momentum tensor via a flow equation in the Gross Neveu model*, arXiv:1501.04371, PTEP 2015 (2015) 4, 043B04.

[84] K. Olive et al. (Particle Data Group), *Quantum Chromodynamics*, Chin. Phys. C, 38, 090001 (2014) and 2015 update.

[85] M. Lüscher, *Chiral symmetry and the Yang-Mills gradient flow*, arXiv:1302.5246, JHEP 04 (2013) 123.

[86] H. Meyer, *A calculation of the shear viscosity in $SU(3)$ gluodynamics*, arXiv:0704.1801, Phys.Rev.D76:101701,2007.

[87] K. Huebner, et al, *Correlation functions of the energy-momentum tensor in $SU(2)$ gauge theory at finite temperature*, arXiv:0808.1127, Phys.Rev.D78:094501,2008.

[88] L. Giusti and H. Meyer, *Thermal momentum distribution from path integrals with shifted boundary conditions*, arXiv:1011.2727, Phys.Rev.Lett.106:131601,2011.

[89] D. Robaina and H. Meyer, *Renormalization of the momentum density on the lattice using shifted boundary conditions*, arXiv:1310.6075, PoS Lattice 2013.

[90] L. Debbio, et al, *Space-time symmetries and the Yang-Mills gradient flow*, arXiv:1306.1173, JHEP 11 (2013) 212.

[91] F. Capponi, et al, *Renormalisation of the energy-momentum tensor in scalar field theory using Wilson flow*, arXiv:1512.02851, PoS Lattice 2015.

[92] F. Capponi, et al, *Renormalisation constants of the lattice energy momentum tensor using the gradient flow*, arXiv:1512.04374, PoS Lattice 2015.

[93] H. Suzuki, et al, *Topological susceptibility in finite temperature (2+1)-flavor QCD using gradient flow*, arXiv:1611.02411, Phys. Rev. D 95, 054502, 2017.

[94] O. Wantz and E. Shellard, *The topological susceptibility from grand canonical simulations in the interacting instanton liquid model: chiral phase transition and axion mass.*, arXiv:0908.0324, Nucl.Phys. B829, 110-160, 2010.

[95] P. Petreczky, et al, *The topological susceptibility in finite temperature QCD and axion cosmology*, arXiv:1606.03145, Phys.Lett. B762 (2016) 498-505.

[96] Sz. Borsanyi, et al, *Lattice QCD for Cosmology*, arXiv:1606.07494, Nature 539 (2016) 7627, 69-71.

[97] R. Kitano and N. Yamada, *Topology in QCD and the axion abundance*, arXiv:1506.00370, JHEP 10 (2015) 136.

[98] Y.C. Chen, et al, *Topological susceptibility in finite temperature QCD with physical $(u/d, s, c)$ domain-wall quarks*, arXiv:2204.01556, 2022.

[99] C. Bonati, et al, *Axion phenomenology and θ-dependence from $N_f = 2 + 1$ lattice QCD*, arXiv:1512.06746, JHEP 1603 (2016) 155.

[100] P. Jahn, et al, *Improved Rewighting for QCD Topology at High Temperature*, arXiv:2002.01153, 2020.

[101] C. Gattringer, et al, *The topological susceptibility of $SU(3)$ gauge theory near T_c*, arXiv:hep-lat/0203013, Phys.Lett. B535 (2002) 358-362.

[102] S. Borsanyi, et al, *Acion cosmology, lattice QCD and the dilute instanton gas*, arXiv:1508.06917, Phys.Lett.B 752 (2016) 175-181.

[103] L. Giusti and M. Lüscher, *Topological susceptibility at $T > T_c$ from master-field simulations of the $SU(3)$ gauge theory*, arXiv:1812.02062, Eur. Phys. J. C79 (2019) 207.

[104] M. Lombardo and A. Trunin, *Topology and axions in QCD*, arXiv:2005.06547, Int.J.Mod.Phys.A 35 (2020) 20, 2030010.

[105] Guy D. Moore, et al, *Topological Susceptibility to High Temperatures via Reweighting*, arXiv:1810.13218, 2018.

[106] T. Hollowood, *Renormalization Group and Fixed Points in Quantum Field Theory*, Springer-Briefs in Physics, ISBN 978-3-642-36311-5, 2013.